Durham E-Theses

Formation of protonium and positronium in atomic collisions

Whitehead, Richard John

Formation of Protonium and Positronium in Atomic Collisions

by

Richard John Whitehead MPhys AMInstP

A thesis submitted to the University of Durham in candidature for the degree of Doctor of Philosophy

Department of Physics,

University of Durham, U.K.

March 2001

Declaration

I declare that the work contained in this thesis has not previously been submitted for a degree, either at this university or at any other. All the work presented herein was conducted by the author, unless explicitly stated otherwise.

R. J. Whitehead, March 2001

Abstract

A minimum-norm method has been developed for solving the coupled integro-differential equations describing the scattering of positrons by one-electron targets in which the rearrangement channels for positronium formation have been explicitly included. The minimum-norm method, applied to this application for the first time in this thesis, is an enhancement of a previously reported least-squares method which has enabled the extension to a significantly larger basis consisting of up to 26 states on the direct centre, including pseudostates, and 3 states on the positronium. The method has been applied here to e^+-H and e^+-He$^+$ scattering; cross sections have been produced for the latter over a range of energies up to 250 eV. The basis was found to be large enough to produce smooth cross sections and little evidence of pseudoresonance structure was found. The results are the first converged cross sections to be calculated for e^+-He$^+$ scattering using the coupled channel approximation. Results for e^+-H scattering compare well with the work of other authors. A highly efficient parallel code was developed for solving the largest coupling cases. The results prove the minimum-norm approach to be an accurate and reliable method for large-scale coupled channel calculations involving rearrangement collisions.

Also in this thesis, the capture of slow antiprotons by atomic hydrogen and positronium has been simulated by the Classical Trajectory Monte Carlo (CTMC) method. Statistically accurate cross sections for protonium and antihydrogen formation have been obtained and the energy dependence of the process established. Antihydrogen formation from antiproton collisions with positronium in the presence of a laser has also been simulated with the CTMC method and the effects of laser polarisation, frequency and intensity studied. Enhancements of the antihydrogen formation cross section were observed and it is suggested that more sophisticated calculations should be undertaken

To Julie and my parents

Preface

In recent years the study of the formation of exotic systems, bound states comprising of particles such as positrons and antiprotons, has received more and more attention. In the case of the interaction of positrons with matter this is largely due to relatively recent developments in experimental positron sources and techniques and the subsequent accumulation of experimental data to compare with theory. On the theory side the study of the interaction of positrons with matter requires quite a large amount of computational effort that, until maybe the last ten years, has not been so widely available. The combination of abundant suitable computing resources and new experimental data has fuelled theoretical investigations and many studies of positron and positronium collisions with many types of atoms and molecules have been made over the last ten years or so. The interaction of antiprotons with matter has also received a great deal of attention due to the prospect of the fundamental tests of physics that could be performed if significant quantities of exotic compounds can be produced and trapped and the high funding that this has attracted.

In this thesis the interaction of exotic particles with matter has been studied using two very different approaches.

In part I, chapters 1–4, a minimum-norm method is developed for solving the coupled integro-differential equations arising from the scattering of positrons by one-electron targets where the rearrangement channels for positronium formation have been explicitly included. The minimum-norm method, applied to this application for the first time in this thesis, is an enhancement of a previously reported least-squares method (Merts and Collins [1], Bransden and Noble [2]) which has enabled the extension of the close coupling basis used in the least-squares approach

to be carried out using a significantly larger basis. This extension allows the use of a much more complete basis including pseudostates [3] and thus the evaluation of cross sections such as ionisation, excitation and electron loss. It is also expected that the use of a large pseudostate basis will give more accurate estimates of the other major cross sections than is possible with the use of eigenstates alone [4].

A brief introduction to positron collisions is given in chapter 1. The close coupling approximation and the close coupling equations in the least-squares and minimum-norm formalisms are discussed in chapter 2; the pseudostate approximation, boundary conditions and alternative approaches are also discussed. Numerical methods are discussed in chapter 3.

The minimum-norm method has been applied here to e^+-H and e^+-He$^+$ scattering; cross sections for the latter have been produced over a wide range of energies, 0–40.8 eV, 40.8–47 eV and 50–250 eV, using sets of basis states up to a 29-state approximation which incorporates eigenstates and pseudostates up to $\overline{8s}$, $\overline{8p}$, $\overline{8d}$ and $\overline{8f}$ on the He$^+$ and 1s, 2s and 2p eigenstates on the positronium. Partial cross sections have been produced up to a total angular momentum of $J = 20$ and extrapolated to higher J using a geometric rule to give cross sections summed over all partial waves. These results are presented and discussed in chapter 4. The 29-state basis was found to be large enough to produce very smooth cross sections for elastic scattering, various excitation processes, ionisation, ground state capture, total capture and electron loss. Little evidence was found in the major cross sections of the pseudoresonance structure reported previously by various other authors; there was, however, evidence of pseudoresonances in the much smaller excited state capture cross sections. The minimum-norm method is also found to give highly accurate phase shifts for pure elastic scattering when compared to variational results. The existence of some previously reported resonances in e^+-H have also been verified, further demonstrating the ability of the minimum-norm method.

Since the evaluation of cross sections using large coupled channel basis sets, such as the 29-state basis, involves a considerable computational effort, a parallel algorithm for the minimum-norm method was developed. This was implemented with the message passing (MPI) library and was found to be highly efficient. The

parallel algorithm is such that it could be straightforwardly ported to a massively parallel computer and thus larger computations could be undertaken.

The results presented in this thesis prove the least-squares/minimum-norm approach to rearrangement collisions to be an accurate and reliable method for large-scale coupled channel calculations involving rearrangement collisions; the results are the first complete cross sections to be calculated for e^+-He^+ scattering using the coupled channel approximation.

In part 2 a purely classical approach, the Classical Trajectory Monte Carlo (CTMC) method, is applied to collisions between heavy exotic particles (e.g. muons, pions and antiprotons) and hydrogen and positronium targets.

The CTMC method has been widely used and, due to the relatively small amount of computing resources required, has been used for many years. Statistically accurate cross sections for protonium and antihydrogen formation have been obtained using an importance sampled initial distribution and the energy dependence of the process established. The results are of greater statistical accuracy and over a wider energy range (in the case of antiproton-positronium collisions) than those reported previously by other authors and are found to agree very well with experimental data for the charge conjugate reaction of proton capture by positronium. The extension of the CTMC method made in this thesis, however, has been the introduction of a laser field to the collision. This has been applied to antihydrogen formation in antiproton-positronium collisions where the effects of laser polarisation, frequency and intensity have been studied. Enhancements of the antihydrogen formation cross section were observed and, in the light of the findings of this preliminary work, it is suggested that it would be worthwhile undertaking further studies of laser enhancement using more sophisticated calculations. The results are an encouraging step in the quest to produce larger quantities of exotic systems.

I would like to thank the staff at RIKEN, Japan for their hospitality during a visit whilst some of this work was undertaken, in particular to Dr. Isao Shimamura for his help in organising the visit, and to the staff at the British Council and JISTEC for making my stay in Japan, 1998, such a memorable experience. I would

also like to thank the many people, friends and collegues, with whom I had many helpful discussions and supported me whilst this work was undertaken. These are: my supervisors, Professors Brian Bransden and David Flower and Drs Jim McCann and Cliff Noble and other friends/collegues within the department, both past and present, Drs Charles Adams, Hilary Davies, Ifan Hughes, Brian Jackson, Niels Kylstra, Mark Leadbeater and Robert Potvliege and Thomas Winiecki. Specifically, I would like to thank Dr. Potvliege for supplying Floquet results for photoionisation of positronium and Dr. K. Ohtsuki for supplying PSS results for antiproton capture by hydrogen. I would also like to say a very special thank you to Dr. Lydia Heck who I am deeply indebted to for her much valued support, sense of humour and constant enthusiasm.

Finally, I would like to express my deepest gratitude to Julie, my partner and best friend, and my parents for their love and support throughout and without whom this work would not have been possible.

R. J. Whitehead

Durham

March 2001

Contents

List of Figures

List of Tables

PART I: Close Coupling Formation of Positronium From Ionic Targets

Chapter 1

Introduction

The study of positrons began with their prediction, by Dirac in 1928 [5], and subsequent experimental verification, by Anderson in 1932 [6]. Probably the first theoretical studies of the interaction of positrons with matter were done by Ore in 1949 [7] and Massey and Mohr in 1954 [8]. Ore postulated that positronium formation, a bound state between a positron and an electron, would be at a maximum when the positron energy lies within an energy band in which no other electronic energy transfer is possible. Of course the positron energy, in the case of an endothermic reaction, must be sufficient for positronium formation to be energetically possible,[1] around 6.8 eV in positron-hydrogen scattering, although this may depend on the surrounding medium. This hypothesis is known as the Ore gap model. In positron-hydrogen collisions the so-called Ore gap lies between the positronium formation threshold and the first excitation threshold, at 10.2 eV.[2] Since then much work has been done and many advances have been made. For a review of the early theoretical work, up to around the end of the 60s, see for example Bransden [9].

Although theoretical work on positron scattering got off to quite a good start early experimental work on positron scattering was somewhat frustrated by the lack of high intensity, low energy, monoenergetic positron beams. Early work relied on the unmoderated positrons produced from nuclear beta decay which have an energy distribution that is peaked rather high with respect to the typical energies required for atomic scattering work, around the typical binding energies of electrons in atoms. More on this later.

Table 1.1: A few of the properties of positronium. Data taken from Ghosh *et al* [10].

	Parapositronium	Orthopositronium
Reduced mass	1/2	
Ionisation potential (eV)	6.8	
Fraction of formation	25%	75%
Lifetime (sec)	1.25×10^{-10}	1.47×10^{-7}
Mode of annihilation	2 γ-rays	3 γ-rays

We now discuss some of the fundamental properties of positrons. As is well known, for every particle there exists an antiparticle of equal mass[3] and equal and opposite charge, the antiparticle of the electron of course being the positron. Although there is a distinct preference for matter over antimatter in the universe, at least in our vicinity, positrons do occur naturally. There is evidence for the existence of positrons both in solar flares and the centre of the galaxy. This evidence is inferred from the detection of photons of energy 511 keV arising from the annihilation of electrons and positrons into photon pairs, a relativistic process which can only be explained fully by quantum electrodynamics. Although the predominant annihilation channel, annihilation into other numbers of photons also occurs, mostly three photon; the fraction of these other processes is however in comparison small.

Of particular interest in studies of positron interactions with matter are the bound states which can be formed. The most notable of these, and the one which occurs most frequently in collision studies, is positronium. Some of the properties of positronium are given in table 1.1. Theoretical evidence is also emerging for the existence of other bound states; for instance, bound states with alkali metals and transition metals [11–13].

On the experimental side a great deal of effort is being put into the production of antihydrogen, $\overline{H}$, the bound state of a positron with an antiproton [14–16].

Antihydrogen, produced in sufficient quantities and trapped for long enough, could provide a very useful test of some of the very fundamental principles of modern physics, notably the CPT theorem [17–19].

It seems appropriate at this point to clarify the reactions considered in this thesis. The possible reaction channels for scattering of positrons by atomic hydrogen and singly ionised helium are

$$
e^+ + \mathrm{H} \longrightarrow
\begin{cases}
e^+ + \mathrm{H} & \text{elastic scattering} \\
e^+ + \mathrm{H}^* & \text{inelastic scattering} \\
e^+ + e^- + p & \text{ionisation} \\
\mathrm{Ps} + p & \text{capture/charge exchange}
\end{cases}
\tag{1.1}
$$

and

$$
e^+ + \mathrm{He}^+ \longrightarrow
\begin{cases}
e^+ + \mathrm{He}^+ & \text{elastic scattering} \\
e^+ + \mathrm{He}^{+*} & \text{inelastic scattering} \\
e^+ + e^- + \alpha & \text{ionisation} \\
\mathrm{Ps} + \alpha & \text{capture/charge exchange}
\end{cases}
\tag{1.2}
$$

respectively, where Ps denotes positronium. Annihilation has been deliberately omitted here since, at the energies considered here, it is only a small contribution to the reaction channels and is often omitted in theoretical calculations, being treated as a perturbation if required once the solution for the other channels has been computed; see, for example, Armour and Humberston [20].

So why study positrons? The interaction of positrons with matter has become an important part of a number of areas of physics. High energy positron collisions with electrons have been a huge part of elementary particle physics for many years, for example at the Large Electron Positron (LEP) collider at CERN which possibly saw the first signs of the existence of the Higgs particle, although this is far beyond the context of this thesis. A quantitative knowledge of positron interactions is necessary for a greater understanding of areas of astrophysics in which the presence of positrons is a significant factor, such as the aforementioned solar flares and the probable existence of positrons near the centre of the galaxy. The application to

positron scattering of methods previously applied to electron scattering provides a useful test of existing methods; also there are new phenomena, very different to what is found in electron scattering, such as the possibility of positronium production, annihilation and the existence of resonances which may differ in character to those found in electron scattering. The simplest kind of rearrangement collision involving positrons is scattering by hydrogenic targets, which is what we consider in this thesis. This also has relevance to the experimental production of antihydrogen in a trap in the form of the charge conjugate reaction $e^--\overline{H}$ which can result in the breakup of the antihydrogen. Furthermore, methods developed for dealing with one electron targets can then be extended to treat more complex two electron targets; for a recent example see Campbell *et al* [21]. The e^+-He^+ reaction studied in this thesis is also the first complete study to be performed of positron scattering by an ion and represents a first step towards the study of other positron-ion reactions.

More recently much theoretical work has been done on positron scattering by atoms, ions and molecules. Perhaps not surprisingly the vast majority of these studies have been with the most simple collision system: positron-hydrogen scattering. A range of theoretical methods have been used. Probably the most accurate at low energies has been the variational method, used by Humberston *et al* [22–25] and Kuang and Gien [26, 27]. Close coupling methods in configuration space have been employed by many authors: Kernoghan *et al* [28–30] and Higgins *et al* [31–33] using the R-matrix method; Igarashi and Toshima [34], Zhou and Lin [35, 36] and Igarashi and Shimamura [37] using the hyperspherical close coupling method; Bransden and Noble [2] using the least-squares method; as well as others. Alternative momentum space methods have been used by Bray *et al* [38–41], Mitroy *et al* [42–50], Basu *et al* [51, 52] and Hewitt *et al* [53, 54]. The above list is by no means complete; the reader is instead referred to the following reviews [10, 20, 21, 55, 56]. Studies of positron collisions have not been limited to hydrogen, however; more complex targets have also been investigated.[4]

In experiments positrons are generally taken from either β-decay or from pair

production generated by EM showers from high energy electron beam collisions:

$$e^- + (Z, N) \longrightarrow e^- + \gamma$$
$$\gamma \longrightarrow e^+ + e^-.$$

(1.3)

The most popular, it seems, is that of β-decay, since radioactive sources are widely available and require much less apparatus than an electron accelerator. A popular source for this is ^{22}Na from which the reaction

$$^{22}\text{Na} \longrightarrow \ ^{22}\text{Ne}^* + e^+ + \bar{\nu},$$

(1.4)
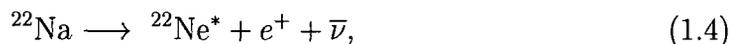
which has a half-life of 2.6 yr, produces positrons distributed over a range of energies up to 540 keV.

Both methods of producing positrons do so mostly at relatively high energies with very few produced in the required energy range, generally epithermal ($\sim$ eV) up to a few keV. What is required then is a method to decelerate them to the required energy, usually by thermalizing them and then reaccelerating them to the required energy if it is above epithermal (as done by, say, [57, 58]). This can be accomplished in a manner similar to that used to decelerate antiprotons in accelerator facilities, however it is sufficient, not to mention easier, to do so by use of a moderating material. Moderating materials used are usually metallic (rather than insulating) since the moderating time ($\sim$ ps) is much less than the typical lifetime against annihilation ($\sim$ 100 ps); tungsten (W) can be used with a good efficiency. An alternative method involves depositing (freezing) a noble gas onto the sodium source; this is found to give a marked improvement in efficiency (roughly an order of magnitude) over metallic moderators.

If large quantities of positrons over a short period of time are required, as in the case of antihydrogen production and spectroscopy [59], techniques are available for trapping and cooling the positrons. The most developed of these methods appears to be that of [60] in which positrons are trapped and then cooled by gas collisions. This way up to 10^{10} positrons may be trapped over a period of about 1 hour and stored for up to several hours, sufficient for the production of enough antihydrogen for spectroscopic measurements. Suffice to say, the technology for

producing positron beams is now, compared to 5–10 years ago, quite well developed.

The production of positronium involves the interaction of the positron beam (or cloud, as in the case of positrons accumulated in a trap) with a material such as silver foil.

Reviews and discussions on positron and positronium production and trapping have been given by a number of authors; see for example [17, 19, 59–62]. A particular experiment is described in some detail in [57, 58]. A recent review of positron trapping techniques and generation of cold, bright positron beams using positron accumulation techniques has been written by Surko *et al* [63].

Measurements of positron interactions in collisions of positrons with hydrogen atoms have been made by Sperber *et al* [64], Jones *et al* [65] and by Zhou *et al* [66]. As far as I am aware no experiments have been done involving the impact of positrons on He^+, however, measurements of electron impact on He^+ have been performed by Defrance *et al* [67] using a crossed beam technique.

To conclude then, much work has been done so far both theoretically and experimentally on positron collisions, although there is a great deal more work yet to be done. It is hoped that the many methods that have been applied so far and the advent of more experimental results will enable a fruitful interplay between theory and experiment in the near future. Most computations have so far been limited to relatively simple targets and theoretical methods for treating complex targets are still, by comparison, in their infancy. It is the purpose of this thesis to develop the least-squares method [2] for use with large basis sets including pseudostates.

In the next chapter the close coupling equations are derived for the specific cases considered and the least-squares method is extended to the minimum-norm method which was found to be necessary in order to obtain consistently accurate results. In chapter 3 the program and numerical methods are discussed in more detail and in chapter 4 results are presented and discussed.

Notes

[1]In some cases, notably the alkali metals, the reaction is exothermic and, in the absence of annihilation, the cross section for positronium formation diverges to infinity at zero energy.

[2]Note that in positron scattering from singly charged helium ions considered in this thesis the Ore gap does not exist since the $n = 2$ excitation channels open up at a lower energy than the positronium channels.

[3]So far there is no evidence to suggest any symmetry breaking here, although this is an important question in itself. For our purposes we may view particle-antiparticle pairs as possessing the same mass.

[4]We give here a list of some references, although by no means complete. Positron scattering by complex (multielectron) atomic targets has been studied by McAlinden *et al* [68–70], Van Reeth and Humberston [71–75], Ryzhikh and Mitroy [76], Watts and Humberston [77], Hewitt *et al* [78–80] and Gianturco and Melissa [81–83]. Scattering of positronium has been studied recently by Blackwood *et al* [84] and Bransden *et al* [85] as well as a number of other authors; for references, see for example the citations contained within [84].

Chapter 2

The Close Coupling and

Pseudostate Approximations

2.1 Introduction

In this chapter we derive the close coupling equations for positron-atom scattering by one electron targets and introduce the least-squares and minimum-norm methods of solution applied in this thesis and show how scattering matrices and cross sections may be computed. We use the method of partial waves in order to reduce the close coupling equations to radial form. We also look at the theory of pseudostates and show how these are applied to extend the basic close coupling method utilising only eigenstates.

The close coupling method, originally introduced by Massey and Mohr [86], has enjoyed much success in both electron-atom and positron-atom scattering. Before talking about the scattering of any particular type of particle by a specific target, however, we derive the radial scattering equations for general scattering. In all that follows, unless explicitly stated otherwise, we work in atomic units (a.u.), in which $e = m = \hbar = 1$.

The Schrödinger equation is

$$H\Psi(\boldsymbol{x}, \boldsymbol{r}, t) = i\frac{\partial \Psi(\boldsymbol{x}, \boldsymbol{r}, t)}{\partial t}; \tag{2.1}$$

$\boldsymbol{x}$ represents the target internal co-ordinates and $\boldsymbol{r}$ represents the scattering co-

ordinate. If we view the system as a beam of particles of equal and well defined energies incident on a target, the system as a whole will be an eigenfunction of the total energy E. The wavefunction may thus be written

$$\Psi(\boldsymbol{x}, \boldsymbol{r}, t) = \psi(\boldsymbol{x}, \boldsymbol{r})e^{-iEt} \tag{2.2}$$

and the Schrödinger equation becomes the time independent equation

$$(H - E)\psi(\boldsymbol{x}, \boldsymbol{r}) = 0. \tag{2.3}$$

If we now expand the wavefunction $\psi(\boldsymbol{x}, \boldsymbol{r})$ as a product of a complete set of eigenfunctions $\phi_m(\boldsymbol{x})$ of the target internal Hamiltonian H_0 and scattering functions $F_m(\boldsymbol{r})$ representing the relative motion of projectile and target, i.e.

$$\psi(\boldsymbol{x}, \boldsymbol{r}) = \sum_m \phi_m(\boldsymbol{x}) F_m(\boldsymbol{r}), \tag{2.4}$$

and write the total Hamiltonian H as

$$H = H_0 - \frac{1}{2\mu}\nabla_r^2 + V_\alpha, \tag{2.5}$$

where $V_\alpha = V_\alpha(\boldsymbol{x}, \boldsymbol{r})$ is the interaction potential between the projectile and the target and μ is the reduced mass, projecting with the target wavefunctions we arrive at the coupled equations

$$\left(-\frac{1}{2\mu}\nabla_r^2 - E + \varepsilon_m\right) F_m(\boldsymbol{r}) = -\sum_n V_{mn}(\boldsymbol{r}) F_n(\boldsymbol{r}). \tag{2.6}$$

Here, $[H_0 - \varepsilon_m]\phi(\boldsymbol{x}) = 0$ and the potential $V_{mn}(\boldsymbol{r})$ is defined by the matrix element

$$V_{mn}(\boldsymbol{r}) \equiv \int d\boldsymbol{x} \, \phi_m^*(\boldsymbol{x}) V_\alpha(\boldsymbol{x}, \boldsymbol{r}) \phi_n(\boldsymbol{x}), \tag{2.7}$$

which in the case of neutral collisions, due to the finite extent of the target electron cloud, we may assume vanishes faster than $1/r$ for large r. We note here that the functions $\phi_m(\boldsymbol{x})$ in (2.4) span both the bound states and the continuum.

The scattering wavefunctions $F_m(\boldsymbol{r})$ may be expanded in terms of eigenfunctions of the total scattering orbital angular momentum l. If we take the case of the spherically symmetric potential $V_{mn}(\boldsymbol{r}) = V_{mn}(r)$, $r \equiv |\boldsymbol{r}|$, then the expansion is[1]

$$F_m(\boldsymbol{r}) = \sum_{l=0}^{\infty} r^{-1} f_m(l, r) P_l(\cos\theta), \tag{2.8}$$

where A_l is a constant and $P_l(\cos\theta)$ is a Legendre polynomial. This expansion of the wavefunction is termed the *method of partial waves*. Defining

$$k_m^2 \equiv 2\mu(E - \varepsilon_m), \tag{2.9}$$

where $k_m^2 > 0$ for open (energetically available) channels and $k_m^2 < 0$ for closed channels, and noting that

$$\nabla^2 = \frac{1}{r^2}\frac{\partial}{\partial r}\left(r^2\frac{\partial}{\partial r}\right) - \frac{\boldsymbol{L}^2}{r^2}, \tag{2.10}$$

we arrive at the coupled radial equations

$$L_i f_i(r) = \sum_j U_{ij} f_j(r), \tag{2.11}$$

where the differential operator

$$L_i = \left(\frac{\mathrm{d}^2}{\mathrm{d}r^2} - \frac{l_i(l_i+1)}{r^2} + k_i^2\right) \tag{2.12}$$

and the reduced potential $U_{ij}(r) = 2\mu V_{ij}(r)$. Expressions for the matrix elements have been given by Percival and Seaton [87].

The scattering of electrons by atoms in the absence of exchange may be described fully by the set of coupled second order differential equations (2.11). The solution of these equations may be found relatively simply by direct numerical integration, e.g. by the Runge-Kutta method [88]. The addition of exchange, for example due to the inclusion of Pauli symmetry in electron scattering or by the replacement of the electron by a positron, complicates the solution of the equations immensely since this introduces an additional, non-local, potential. The potential, V_{ij}, then becomes replaced by an integral

$$U_{ij}f_j(r) = \int_0^\infty U_{ij}(r,r')f_j(r')dr' \tag{2.13}$$

The resulting integro-differential equations can no longer be reduced to a set of second order differential equations and hence direct integration is no longer possible.[2]

2.2 The Close Coupling Approximation and Pseudostates

Above the first inelastic threshold, where more than one channel is open, in order for the individual excitation cross sections to be calculated the trial wave function must contain components referring to all open channels and possibly some closed ones too.[3] From this point on a one-electron target is assumed, for which the internal wavefunction is known exactly. In electron-atom scattering, with no exchange and neglecting spin, the wavefunction is simply

$$\Psi^\alpha = \sum_{i=1}^{N} \phi_i(\boldsymbol{r}_1) F_i^\alpha(\boldsymbol{r}_2).\tag{2.14}$$

Here, $\phi_i(\boldsymbol{r}_1)$ denotes the target's internal wavefunction, $F_i^\alpha(\boldsymbol{r}_2)$ represents the projectile scattering wavefunction and α identifies the solution.

We note that this expansion is truncated: there are N channels, of which $1 \leqslant n_{op} \leqslant N$ are open. This is an important point. The reason for this truncation is a practical one since from this trial function inserted into the Schrödinger equation a set of N differential equations of the form in equation (2.11) are obtained. Clearly in any calculation there will be a maximum number of channels, N, which may be retained depending on factors such as the computing resources available and the method of solution employed. The equations are coupled to one-another by the potentials V_{ij}. In practice, many channels are found to be only very weakly coupled to the important channels and can therefore be neglected. The inclusion of electron exchange, in which the electrons are allowed to interchange, is accomplished straightforwardly by the addition of terms as in

$$\Psi^\alpha = \left[1 + (-)^S P_{12}\right] \sum_{i=1}^{N} \phi_i(\boldsymbol{r}_1) F_i^\alpha(\boldsymbol{r}_2)\tag{2.15}$$

where S is the total spin and P_{12} is an operator that exchanges the coordinates of the two electrons. The addition of the exchange terms, as discussed above, gives rise to an additional integral term in the scattering equations.

Up until now we have discussed mainly the scattering of electrons. What happens if we now replace the electron with a positron? From this point on we will restrict ourselves to positron scattering only, unless explicitly stated otherwise.

The difference between an electron and a positron is its charge. What we now have is a positively charged projectile rather than a negatively charged one. At first sight it may appear that all that is involved is a change in sign of the interaction potential; the situation is, however, much more complicated than this. One should first note that, even with this difference in sign, in both positron-atom and electron-atom scattering the long-range polarisation force felt by the projectile due to distortion of the target electron cloud is attractive.

The first difference arises in the *static interaction*[4] which in the case of electrons is attractive but for positrons is repulsive, although they are both equal in magnitude. Thus, whilst the static interaction in electron-atom scattering tends to add to the long-range polarisation, for positrons it tends to cancel.

The second difference between electrons and positrons is the absence of any Pauli exchange between the projectile and target. In the case of electron scattering the presence of this exchange introduces extra terms to the close coupling expansion, as in equation (2.15).[5] At first sight this may also seem to considerably simplify the problem, however, unfortunately this is not the case. The difficulty with positrons is that, due to their opposite sign, the possibility exists of the positron picking up an electron from the target to form positronium. This rearrangement needs be taken into account in the trial wavefunction and the expansion now becomes

$$\Phi^\alpha = \sum_{i=1}^{N} \phi_i(\boldsymbol{r})F_i^\alpha(\boldsymbol{x}) + \sum_{j=1}^{M} \psi_j(\boldsymbol{R})G_j^\alpha(\boldsymbol{\rho}). \tag{2.16}$$

Here, r and x represent the electron and positron respectively in the direct partition and R and ρ represent the positronium internal coordinate and scattering coordinate respectively in the exchange partition. By partition, we are referring to the asymptotic form of the solution, where the direct partition is defined as being the same arrangement as the incident channel (e.g. e$^+$-H) and the exchange partition refers to the rearranged channels (e.g. p-Ps). $F_i^\alpha(\boldsymbol{x}) = x^{-1}f_i^\alpha(\boldsymbol{x})$ and $G_j^\alpha(\boldsymbol{\rho}) = \rho^{-1}g_j^\alpha(\boldsymbol{\rho})$ define reduced scattering wavefunctions $f_i^\alpha(\boldsymbol{x})$ and $g_j^\alpha(\boldsymbol{\rho})$ direct and exchange partitions respectively, introduced for convenience later on. From this expansion coupled integro-differential equations result which will be derived

and discussed in detail later on. From now on, in general, only the reduced scattering wavefunctions will be referred to and for simplicity will be called scattering wavefunctions.

There are two complications here. The first is the presence of non-local exchange terms in the equations similar to those present in electron scattering. The second is that, while the total wavefunction in electron scattering is completely defined by the Pauli principle, it is more difficult to describe in positron scattering due to the possibility of linear dependencies in the expansion (2.16). The positron-scattering wavefunction is thus more difficult to describe near the origin. In actual fact though linear dependencies have so far not been observed in practice.[6]

We might now question about the expansions (2.15) and (2.16) how the target states ϕ_i and ψ_j are chosen since, in general, they will come from an infinite set and hence the expansion would contain an infinite number of terms. It turns out that in fact many terms give rise to equations that are only weakly coupled to the rest of the set and hence have little or no effect on the scattering. These terms may then be dropped from the expansion leaving behind a set of $N + M$ equations that, within a certain accuracy, completely describe the scattering.

Simple though this may seem, a problem does arise with considering only target eigenstates. The problem is most apparent when the effect of long range polarisation forces is significant since the interaction potential, in the case of a neutral target, is proportional to the dipole polarisability of the target. As is well known, the discrete atomic states of hydrogen contribute to only around 82% of the polarisability (with much of this coming from the 2p level) while the remaining 18% comes from the continuum. Furthermore, if the collision energy is high enough, ionisation of the target (promotion of a previously bound electron to the continuum) may have a significant effect. Clearly, in the above expansion this has not in any way been accounted for[7] and, since the energy on the target takes on a continuous index above the ionisation threshold, this is not a trivial problem. A common way to overcome this problem, and the way which we employ in the present calculations, is given by the introduction of *pseudostates.*

Pseudostates were first introduced by Damburg and Karule [3] for use in electron-

hydrogen scattering. One or more pseudostates of this kind are added to the eigenfunction expansion and are designed such that they reproduce the dipole polarisability exactly. Pseudostates of the kind introduced by Damburg and Karule have since been used in positron-hydrogen scattering by Higgins and Burke [32] who employed $\overline{2s}$ and $\overline{2p}$ states on both the hydrogen and positronium centres. These states were of the form $(ar + br^2) \exp(-\alpha r)$ and $(cr^2 + dr^3) \exp(-\alpha r)$ for the s and p states respectively, where the range α was chosen to match that of the respective ground states.

A problem that was found in the use of small basis sets such as these was the existence of spurious resonances above threshold which varied in character with changes in the basis. The first of these to be discovered was a broad s-wave resonance at 2.62 Ryd in the coupled-static approximation for positron-hydrogen scattering discovered by Higgins and Burke [31]. The existence of this resonance has since been confirmed by other authors. The fact that this resonance occurs was at first puzzling since, as pointed out by Walters $et\ al$ [89], resonances cannot occur above the ionisation threshold in positron-hydrogen scattering [90, 91]. It has since been shown by many authors, however, that these resonances are purely a product of the incomplete model and do not occur in the exact theory.

An alternative method for generating pseudostates, and the one which we adopt in this thesis, is one involving an expansion in terms of L^2 states introduced by Burke $et\ al$ [92–94]. Pseudostates, $\Upsilon_i(r)$, are formed by a linear superposition of N basis functions,

$$\Upsilon_i(r) = \sum_{j=1}^{N} c_j^{(i)} v_j(r), \quad i = 1, 2, \dots, N, \tag{2.17}$$

where the parameters, $c_j^{(i)}$, are chosen in order to diagonalise the target Hamiltonian, H_r; i.e.

$$\langle \Upsilon_i | H_r | \Upsilon_j \rangle = \epsilon_i \delta_{ij}. \tag{2.18}$$

In the work of Burke $et\ al$ the pseudostates were expanded using a basis of Slater functions to diagonalise the Hamiltonian. In the work of this thesis we use a similar expansion except that we use a basis composed of Laguerre functions. An expansion

of this kind was used by Bray and Stelbovics [4] who pointed out that the Laguerre basis is more suitable, numerically, for large basis sets; the lower energy states are also found to converge rapidly to the exact eigenstates.

By producing a set of pseudostates from a significant number of basis functions with carefully chosen parameters one produces a set of target states consisting of, essentially, a few of the lowest energy eigenstates and a range of pseudostates with effective energies reaching into the continuum. By increasing the number of pseudostates in the expansion one obtains an increasingly accurate representation of the full wavefunction. Pseudostates are thus an attractive approach to solving the problems of eigenstate only expansions. As well as offering a more complete expansion of the wavefunction they also retain desirable features of the close coupling method such as important minimum principles. One downside of pseudostate expansions, however, is that they introduce spurious pseudothresholds to the S-matrix from which so-called pseudoresonance structure may arise. These are false resonances originating solely from the presence of these pseudothresholds.

The use of pseudostates has been studied in some detail by Bray *et al* using their so-called Convergent Close Coupling (CCC) method [4]. Although the CCC method was first applied to the case of electron-hydrogen scattering, these results are still of great interest due to the issue of convergence of the target basis. Sets of N pseudostates were used to represent the hydrogen target. The pseudostates were constructed from a Laguerre basis similar to that used in this thesis and convergence was analysed for s-wave scattering as a function of increasing N. Up to $N = 30$ were used and the results tested against the accurate results of the Poet-Temkin model [95, 96] (described in, for example, [97, 98]). They found that the characteristic pseudoresonance structure found by previous authors and mentioned above was evident in the smaller basis set results but then disappeared for the 30-state runs. They also found that a very narrow genuine resonance in the 2s cross section around 2 eV was reproduced well by the model. Convergence was found not to be a function of the target scaling parameter, ζ, in the Laguerre set (3.4), however it was suggested that the rate of convergence may depend on ζ. The rate of convergence, however, did depend critically on the collision energy.

With minor modifications to the CCC code of [4] the CCC method was extended to treat positron-hydrogen collisions in the absence of exchange [38, 39]. The major changes involve omission of the electron exchange potentials and reversal of the signs of the potentials in the Hamiltonian. Although the CCC case for electron-hydrogen scattering had already been studied carefully, with the omission of the exchange potentials it was not immediately clear how the convergence might proceed. From a formal point of view an infinite expansion of states on the target centre (hydrogen) will be complete; however, in practice, a truncated expansion cannot account fully for the states on the exchange centre. The reason for this is that the wavefunction extends to infinite distances in both scattering variables, in contrast to the electron scattering case which is infinite in only one variable. They found that convergence of the pure elastic scattering [38] was indeed much different for positrons with convergence to within 1% for the first partial wave requiring targets of angular momentum up to $l = 15$ with $N_l \approx 6$ targets with angular momentum l. Comparison with converged close coupling results containing only eigenstates demonstrated the importance of allowing for virtual excitation. Above around 100 eV where positronium formation is insignificant they also were able to produce well converged results [39], believed to be accurate to within a few percent and in good agreement with variational calculations and experimental results (see references cited therein).

More recently the CCC method has been extended by Kadyrov and Bray [40, 41] to introduce the positronium formation channels as well. Instead of expanding the targets on the hydrogen centre using both eigenstates and pseudostates and using only eigenstates on the exchange centre, as is more usually the case, they expanded with up to 17 pseudostates on each centre. Although nonorthogonal, and hence ill-conditioned, with a careful choice of numerical precision they did not encounter any significant numerical problems and were able to show that the pseudoresonances encountered using other models only disappeared when using larger two-centred expansions with at least 11 states on each centre. It seems then that for very well converged results two-centred expansions of this kind are necessary. However, computations of this kind are very large compared to expansions with only a few

states on the positronium centre and for many cases are simply impractical.

2.3 Derivation of the Close Coupling Equations

Having discussed the close coupling approximation in a general context, in this section and appendix C we derive the radial scattering equations and matrix elements in detail for the cases considered in this thesis.

The system may be described by the time independent Schrödinger equation

$$[H - E] \Psi^{JM} = 0 \tag{2.19}$$

for a fixed centre of mass energy, E, where the scattering wavefunction, Ψ, is indexed by the quantum numbers for total angular momentum, J, and its projection, M. As discussed above, the wavefunction may be partitioned into terms representing separately the direct and exchange partition channels as

$$\Psi^{JM} = \Psi_D^{JM} + \Psi_X^{JM}, \tag{2.20}$$

where

$$\Psi_D^{JM} = \sum_\alpha \overline{\phi}_{\alpha L_\alpha l_\alpha}^{JM}(\boldsymbol{r}; \hat{x}) \frac{1}{x} f_{\alpha, L_\alpha}^J(x) \qquad \text{Direct} \tag{2.21a}$$

$$\Psi_X^{JM} = \sum_\gamma \overline{\psi}_{\gamma L_\gamma l_\gamma}^{JM}(\boldsymbol{R}; \hat{\rho}) \frac{1}{\rho} g_{\gamma, L_\gamma}^J(\rho) \qquad \text{Exchange.} \tag{2.21b}$$

Note that spin has been neglected since spin interactions are negligible. Here,

$$\overline{\phi}_{\alpha L_\alpha l_\alpha}^{JM}(\boldsymbol{r}; \hat{x}) = R_{n_\alpha l_\alpha}(r) Y_{l_\alpha m_\alpha}(\hat{r}) \times$$
$$\langle L_\alpha l_\alpha; m_\alpha' m_\alpha | JM \rangle Y_{L_\alpha m_\alpha'}(\hat{x})$$
$$= \phi_{\alpha l_\alpha}(\boldsymbol{r}) \langle L_\alpha l_\alpha; m_\alpha' m_\alpha | JM \rangle Y_{L_\alpha m_\alpha'}(\hat{x}) \tag{2.22a}$$

$$\overline{\psi}_{\gamma L_\gamma l_\gamma}^{JM}(\boldsymbol{R}; \hat{\rho}) = S_{n_\gamma l_\gamma}(R) Y_{l_\gamma m_\gamma}(\hat{R}) \times$$
$$\langle L_\gamma l_\gamma; m_\gamma' m_\gamma | JM \rangle Y_{L_\gamma m_\gamma'}(\hat{\rho})$$
$$= \psi_{\gamma l_\gamma}(\boldsymbol{R}) \langle L_\gamma l_\gamma; m_\gamma' m_\gamma | JM \rangle Y_{L_\gamma m_\gamma'}(\hat{\rho}); \tag{2.22b}$$

$\phi_{\alpha l_\alpha}(\boldsymbol{r})$ and $\psi_{\gamma l_\gamma}(\boldsymbol{R})$ are the target internal wavefunctions; $f_{\alpha, L_\alpha}^J(x)$ and $g_{\gamma, L_\gamma}^J(\rho)$ represent the scattering wavefunctions; the subscripts D and X represent the direct and exchange components respectively; $Y_{l_\alpha m_\alpha}(\hat{r})$ and $Y_{l_\gamma m_\gamma}(\hat{R})$ etc. are spherical harmonics; and $\langle L_\alpha l_\alpha; m_\alpha' m_\alpha | JM \rangle$ and $\langle L_\gamma l_\gamma; m_\gamma' m_\gamma | JM \rangle$ are Clebsch-Gordan

Figure 2.1: Jacobi coordinates.
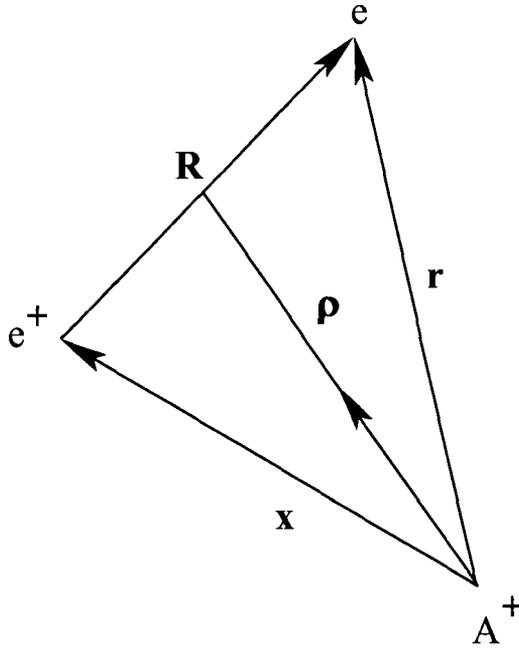
coefficients. The angular factors coupling the target to the scattered particle have been included in the channel functions $\overline{\phi}^{JM}_{\alpha L_\alpha l_\alpha}(\boldsymbol{r}; \hat{x})$ and $\overline{\psi}^{JM}_{\gamma L_\gamma l_\gamma}(\boldsymbol{R}; \hat{\rho})$ for convenience later; the summations over the magnetic quantum numbers are implicit. We note that the l_i and L_i obey the relation

$$|J - l_i| \leqslant L_i \leqslant J + l_i, \qquad (2.23\text{a})$$

equivalently written as

$$\Delta(L_i l_i J), \qquad (2.23\text{b})$$

according to the parity condition

$$\Pi^J = (-1)^J = (-1)^{L_i + l_i}. \qquad (2.24)$$

Working in Jacobi coordinates (figure 2.1), such that the internal and centre of mass coordinates of the positronium (R, ρ) are related to the electron and positron coordinates relative to the nucleus (r, x) by

$$\boldsymbol{R} = \boldsymbol{r} - \boldsymbol{x} \qquad (2.25\text{a})$$

$$\boldsymbol{\rho} = \boldsymbol{x} + \tfrac{1}{2}\boldsymbol{R}, \qquad (2.25\text{b})$$

the Hamiltonian may be written either in terms of $(\boldsymbol{x}, \boldsymbol{r})$ or $(\boldsymbol{R}, \boldsymbol{\rho})$:

$$H = -\frac{1}{2}\nabla_x^2 - \frac{1}{2}\nabla_r^2 - \frac{1}{R} + \frac{Z}{x} - \frac{Z}{r} \tag{2.26a}$$

$$= -\frac{1}{4}\nabla_\rho^2 - \nabla_R^2 - \frac{1}{R} + \frac{Z}{x} - \frac{Z}{r}, \tag{2.26b}$$

where Z denotes the nuclear charge. The Schrödinger equation (2.19) may be partial wave analysed by substituting in (2.20) and projecting onto $\overline{\phi}_{\alpha L_\alpha l_\alpha}^{JM}(\boldsymbol{r}; \hat{x})$ and $\overline{\psi}_{\gamma L_\gamma l_\gamma}^{JM}(\boldsymbol{R}; \hat{\rho})$, i.e.

$$\int d\hat{x} \int d\boldsymbol{r} \overline{\phi}_{\beta L_\beta l_\beta}^{J*}(\boldsymbol{r}; \hat{x}) \left[H - E\right] \Psi^{JM} = 0 \tag{2.27a}$$

$$\int d\hat{\rho} \int d\boldsymbol{R} \overline{\psi}_{\delta L_\delta l_\delta}^{J*}(\boldsymbol{R}; \hat{\rho}) \left[H - E\right] \Psi^{JM} = 0, \tag{2.27b}$$

where $*$ denotes complex conjugation. These equations comprise four matrix elements:

$$M_1 \equiv \int d\hat{x} \int d\boldsymbol{r} \overline{\phi}_{\beta L_\beta l_\beta}^{J*}(\boldsymbol{r}; \hat{x}) \left[H - E\right] \Psi_D^{JM} \tag{2.28a}$$

$$M_2 \equiv \int d\hat{\rho} \int d\boldsymbol{R} \overline{\psi}_{\delta L_\delta l_\delta}^{J*}(\boldsymbol{R}; \hat{\rho}) \left[H - E\right] \Psi_X^{JM} \tag{2.28b}$$

$$M_3 \equiv \int d\hat{x} \int d\boldsymbol{r} \overline{\phi}_{\beta L_\beta l_\beta}^{J*}(\boldsymbol{r}; \hat{x}) \left[H - E\right] \Psi_X^{JM} \tag{2.28c}$$

$$M_4 \equiv \int d\hat{\rho} \int d\boldsymbol{R} \overline{\psi}_{\delta L_\delta l_\delta}^{J*}(\boldsymbol{R}; \hat{\rho}) \left[H - E\right] \Psi_D^{JM} \tag{2.28d}$$

or, equivalently,

$$M_1 \equiv \left\langle \overline{\phi} \left| H - E \right| \Psi_D^J \right\rangle$$

$$M_2 \equiv \left\langle \overline{\psi} \left| H - E \right| \Psi_X^J \right\rangle$$

$$M_3 \equiv \left\langle \overline{\phi} \left| H - E \right| \Psi_X^J \right\rangle$$

$$M_4 \equiv \left\langle \overline{\psi} \left| H - E \right| \Psi_D^J \right\rangle.$$

Using the fact that

$$\left\langle \phi_\alpha \left| -\frac{1}{2}\nabla_r^2 - \frac{Z}{r} \right| \phi_\beta \right\rangle = \delta_{\alpha\beta}\epsilon_\alpha \tag{2.29a}$$

and

$$\left\langle \psi_\gamma \left| -\nabla_R^2 - \frac{1}{R} \right| \psi_\delta \right\rangle = \delta_{\gamma\delta}\eta_\gamma \tag{2.29b}$$

and defining

$$E = \frac{1}{2}k_\alpha^2 + \epsilon_\alpha = \frac{1}{4}{k'_\gamma}^2 + \eta_\gamma \qquad (2.30)$$

M_1 and M_2 can be evaluated to

$$M_1 = -\frac{1}{2x}\left\{\frac{\mathrm{d}^2}{\mathrm{d}x^2} - \frac{L_\alpha(L_\alpha+1)}{x^2} - 2\left(\frac{Z-1}{x}\right) + k_\alpha^2\right\}f_{\alpha L_\alpha}^J(x)$$
$$+ \frac{1}{2x}\sum_\beta V_{\alpha\beta}(x)f_{\beta L_\beta}^J(x) \qquad (2.31)$$

$$M_2 = -\frac{1}{4\rho}\left\{\frac{\mathrm{d}^2}{\mathrm{d}\rho^2} - \frac{L_\gamma(L_\gamma+1)}{\rho^2} + {k'_\gamma}^2\right\}g_{\gamma L_\gamma}^J(\rho)$$
$$+ \frac{1}{4\rho}\sum_\delta W_{\gamma\delta}(\rho)f_{\gamma L_\delta}^J(\rho) \qquad (2.32)$$

where the direct potentials $V_{\alpha\beta}(x)$ and $W_{\gamma\delta}(\rho)$ are given by the matrix elements

$$V_{\alpha\beta} = \left\langle \phi_\alpha \left| \frac{1}{x} - \frac{1}{R} \right| \phi_\beta \right\rangle \qquad (2.33)$$

$$W_{\gamma\delta} = \left\langle \psi_\gamma \left| \frac{Z}{x} - \frac{Z}{r} \right| \psi_\delta \right\rangle. \qquad (2.34)$$

Note that in (2.31) the overall Coulomb interaction in the direct partition is shown explicitly. The direct potentials V_{ij} and W_{ij} therefore vanish faster than $1/x$ and $1/\rho$ respectively. These matrix elements are evaluated further in appendix C where they are shown to give rise to local, energy independent potentials.

M_3 and M_4 are more complicated and give rise to non-local potentials that depend upon energy and which couple together the scattering wavefunctions $f_{\alpha L_\alpha}^J(x)$ and $g_{\gamma L_\gamma}^J(\rho)$ thereby allowing for rearrangement of the particles to occur in the central collision complex. The forms of these matrix elements are (appendix C)

$$M_3 = \sum_{\gamma L_\gamma} \int_0^\infty \rho\,\mathrm{d}\rho K_{\alpha\gamma}(x,\rho)g_{\gamma L_\gamma}^J(\rho) \qquad (2.35)$$

$$M_4 = \sum_{\alpha L_\alpha} \int_0^\infty x\,\mathrm{d}x \overline{K}_{\gamma\alpha}(\rho,x)f_{\alpha L_\alpha}^J(x), \qquad (2.36)$$

where the exchange kernels, $K_{\alpha\gamma}(x,\rho)$ and $\overline{K}_{\gamma\alpha}(\rho,x)$, are given by[8]

$$K_{\alpha\gamma}(x,\rho) = \sum_{ac\lambda} A_{ac\lambda}\left[K_{\lambda,\alpha\gamma}^{(1)}(x,\rho) + \left(-\frac{1}{4}\right)K_{\lambda,\alpha\gamma}^{(2)}(x,\rho)\left\{\frac{\mathrm{d}^2}{\mathrm{d}\rho^2} - \frac{L_\gamma(L_\gamma+1)}{\rho^2} + {k'_\gamma}^2\right\}\right]$$

$$(2.37a)$$

and

$$\overline{K}_{\gamma\alpha}(\rho,x) = \sum_{ac\lambda} \overline{A}_{ac\lambda} \left[\overline{K}^{(1)}_{\lambda,\gamma\alpha}(\rho,x) + \left(-\frac{1}{2}\right) \overline{K}^{(2)}_{\lambda,\gamma\alpha}(\rho,x) \left\{ \frac{\mathrm{d}^2}{\mathrm{d}x^2} - \frac{L_\alpha(L_\alpha+1)}{x^2} + k_\alpha^2 \right\} \right].$$

(2.37b)

The four kernels $K^{(1)}_{\lambda,\alpha\gamma}(x,\rho)$, $K^{(2)}_{\lambda,\alpha\gamma}(x,\rho)$, $\overline{K}^{(1)}_{\lambda,\gamma\alpha}(\rho,x)$ and $\overline{K}^{(2)}_{\lambda,\gamma\alpha}(\rho,x)$ are energy independent and all angular factors, also energy independent, are contained in the terms $A_{ac\lambda}$ and $\overline{A}_{ac\lambda}$. We thus arrive at coupled equations

$$\left(\frac{\mathrm{d}^2}{\mathrm{d}x^2} - \frac{L_\alpha(L_\alpha+1)}{x^2} - 2\left(\frac{Z-1}{x}\right) + k_\alpha^2 \right) f^J_{\alpha,L_\alpha}(x) =$$
$$\sum_{\beta,L_\beta} V_{\alpha\beta}(x) f^J_{\beta,L_\beta}(x) + 2 \sum_{\gamma,L_\gamma} \int_0^\infty \mathrm{d}\rho(x\rho) K_{\alpha\gamma}(x,\rho) g^J_{\gamma L_\gamma}(\rho) \quad (2.38a)$$

$$\left(\frac{\mathrm{d}^2}{\mathrm{d}\rho^2} - \frac{L_\gamma(L_\gamma+1)}{\rho^2} + k_\gamma'^2 \right) g^J_{\gamma,L_\gamma}(\rho) =$$
$$\sum_{\delta,L_\delta} W_{\gamma\delta}(\rho) g^J_{\delta,L_\delta}(\rho) + 2 \sum_{\alpha,L_\alpha} \int_0^\infty \mathrm{d}x(x\rho) \overline{K}_{\gamma\alpha}(x,\rho) f^J_{\alpha L_\alpha}(x), \quad (2.38b)$$

where all of the energy dependence has been factored out into simple derivatives of the scattering wavefunctions, with as much of the rest of the equations evaluated in energy independent factors. These factors thus only need be evaluated once for each coupling case, i.e. for each choice of expansion (2.21) and for each total angular momentum J.

We now begin to compactify the notation by defining the operator

$$L_{ij} \equiv \int_0^\infty \mathrm{d}r \left\{ \delta(r-r') \left[\frac{\mathrm{d}^2}{\mathrm{d}r^2} + k_i^2 - \frac{L_i(L_i+1)}{r^2} - \frac{Z-1}{r} \eta_i \right] \delta_{ij} \right.$$
$$\left. - \delta(r-r') V_{ij}(r) - K_{ij}(r,r') \right\}, \quad (2.39)$$

where $\eta_i = 2$ for channel i in the direct partition and $\eta_i = 0$ for the Ps channels. The reader should note that factors of $2x\rho$ have been absorbed here into the exchange kernels $K_{ij}(r,r')$. We now have the set of coupled equations

$$\boldsymbol{L}\boldsymbol{f}^\alpha = 0, \qquad i = 1,\dots,I \qquad (2.40)$$

where α labels linearly independent solutions. We also impose the boundary conditions

$$f_i^\alpha(r) \sim r^{L_i+1} \qquad \text{as } r \to 0 \tag{2.41a}$$

$$f_i^\alpha(r_B) = d_i^\alpha \qquad d_i^\alpha \text{ constant.} \tag{2.41b}$$

The first of these conditions, (2.41a), is mandatory.[9] The second condition, (2.41b), is imposed for convenience as part of the solution method and defines the linearly independent solutions identified by the vectors $\boldsymbol{d}^\alpha$; this set of solutions may then be used later by matching to the appropriate boundary conditions to define the actual scattering wavefunction for the problem. In the present case it was considered convenient to define $\boldsymbol{d}^\alpha$ by[10]

$$d_i^\alpha = \delta_{i\alpha}. \tag{2.42}$$

In principle the set of solutions should also be independent of the choice of r_B, but in practice, working with finite precision arithmetic, the result may depend on the choice of r_B. This will be discussed in more detail in chapter 3.

2.4 Least-Squares and Minimum-Norm Methods of Solution

The least-squares method is not new to scattering theory; it has been employed previously in electron scattering calculations by Merts and Collins [1] who used it to solve the linear differential equations arising from electron scattering by atoms, molecules and ions in an intermediate radial region beyond the charge cloud of the target. It was compared to methods such as R-matrix propagation techniques and accelerated asymptotic expansions [99–101] to which it was found to compare favourably. Although the equations arising from electron scattering in the intermediate radial region involve only local potentials, Merts and Collins also noted that it could be used to treat non-local potentials.

In this section it is shown how the least-squares technique may be extended to treat the integro-differential equations derived in the previous section arising

from the full close coupling treatment of scattering of positrons from hydrogenic targets [2]. Although found to be adequate for calculations involving a moderate number of target states, such as eigenfunction-only expansions, when applied to calculations involving a large number of pseudostates the extended least-squares method was found to be difficult to apply successfully. In light of this an enhancement of the least-squares method, called the minimum-norm method, was developed for this thesis which will be described later on in this section. General methods for solving integral equations are discussed in, for example, the books by Delves and Mohamed [102] and Delves and Walsh [103], whilst more general issues involved in linear equation solving are discussed by Golub and Van Loan [104].

We begin by noting that there exists a region of space given by $x < x_a$, $\rho < \rho_a$ outside which the exchange potentials may be considered negligible. In this external region the exchange[11] terms may therefore be neglected and a decoupling occurs between the equations representing each partition. This situation corresponds physically to a well defined arrangement of the particles where only the local potentials remain, acting upon channels within a particular arrangement only. We thus are left with two independent sets of differential equations which may now be solved by direct integration, e.g. Runge-Kutta [88], or by R-matrix propagation techniques. We shall discuss these propagation techniques and solution of the scattering equations in the asymptotic region in later sections.

In the least-squares and minimum-norm methods of solution we make use of the above decoupling by defining a so-called inner region[12] of space, depicted in figure 2.2, by $x < x_a$, $\rho < \rho_a$, outside which the exchange potentials are negligible. We expand the scattering wavefunction over this region in terms of a set of basis functions, $\phi_\lambda^i(r)$:

$$f_i^\alpha(r) = \sum_{\lambda=1}^{\Lambda} C_{i\lambda}^\alpha \phi_\lambda^i(r). \qquad (2.43)$$

Furthermore we demand that

$$\phi_\lambda^i(r) \sim r^{L_i+1} \qquad \text{as } r \to 0 \qquad (2.44)$$

so that the boundary condition (2.41a) is automatically satisfied. We remark here that there is a notable difference between this expansion and that of Merts and

Figure 2.2: Schematic representation of the partitioning of space in the least-squares approach.
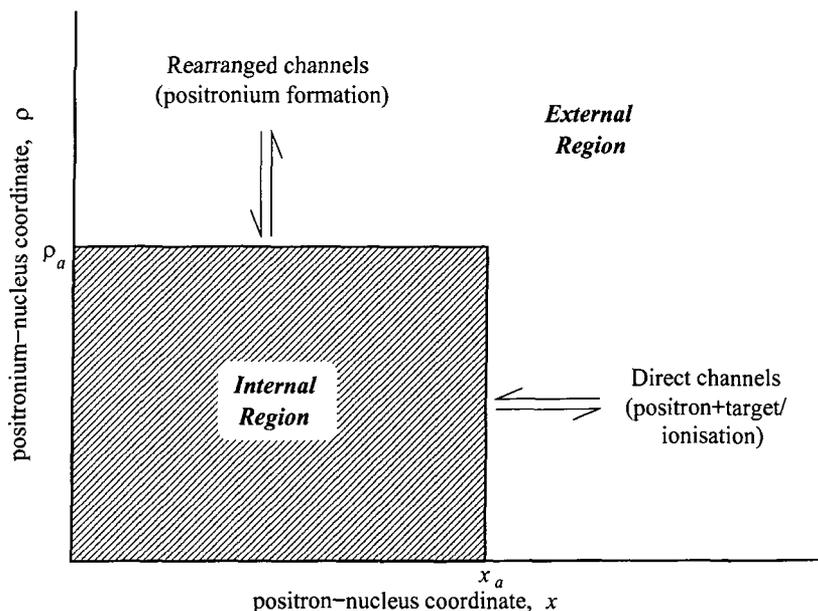
Collins. In our case the expansion of the wavefunction is over a finite region, in contrast to Merts and Collins who expand over a region that extends out to infinity. The advantage of expanding over a finite region is that an effectively complete set of orthogonal basis functions may be used.[13] It turns out, as we shall find out later, that for large scattering calculations with many channels, up to 60 or more, this completeness, with no linear dependencies,[14] is critical for the reliability of the method and for obtaining accurate cross sections. The exact choice of basis functions $\phi_\lambda^i(r)$ will be discussed in chapter 3.

The least-squares problem now amounts to a minimisation of the functional

$$I^\alpha = \sum_{i=1}^{I} \sum_{q=1}^{Q} \left[\sum_{j=1}^{I} L_{ij} f_j^\alpha(r_q) \right]^2 + \sum_{i=1}^{I} \left[f_i^\alpha(r_B) - d_i^\alpha \right]^2 \qquad (2.45)$$

where the mesh points r_q, $q = 1, \ldots, Q$ cover the range $0 \leqslant r \leqslant r_i$, with Q sufficient to determine the coefficients $C_{i\lambda}^\alpha$ uniquely, and the nonlocal potentials are evaluated using a numerical quadrature, i.e.

$$\int_0^\infty K_{ij}(r, r') f_j^\alpha(r') dr' = \sum_{q'=1}^{Q'} K_{ij}(r_q, r_{q'}) f_j^\alpha(r_{q'}) w_{q'}. \qquad (2.46)$$

Using the expansion (2.43) we have

$$I^\alpha = \sum_{i=1}^{I} \sum_{q=1}^{Q} \left[\sum_{\lambda=1}^{\Lambda} \sum_{j=1}^{I} M_{ij\lambda}(r_q) C_{i\lambda}^\alpha \right]^2 + \sum_{i=1}^{I} \left[\sum_{\lambda=1}^{\Lambda} \phi_\lambda^i(r_B) C_{i\lambda}^\alpha - d_i^\alpha \right]^2 \qquad (2.47)$$

where

$$M_{ij\lambda}(r_q) = \delta_{ij} \left[\frac{\mathrm{d}^2}{\mathrm{d}r^2} + k_i^2 - \frac{L_i(L_i+1)}{r^2} - \frac{Z-1}{r}\eta_i \right] \phi_\lambda^i(r) \Bigg|_{r=r_q}$$

$$- V_{ij}(r_q)\phi_\lambda^j(r_q) - \sum_{q'=1}^{Q'} K_{ij}(r_q, r_{q'})\phi_\lambda^j(r_{q'})w_{q'}. \qquad (2.48)$$

$r_{q'}$, $w_{q'}$ are quadrature nodes and weights; $M_{ij\lambda}(r_q)$ is called the *M-matrix*. Now, minimising I^α with respect to the coefficients $C_{i\lambda}^\alpha$, i.e.

$$\frac{\partial I^\alpha}{\partial C_{i\lambda}^\alpha} = 0 \qquad \begin{cases} i = 1, \dots, I \\ \\ \lambda = 1, \dots, \Lambda \end{cases} \qquad (2.49)$$

we arrive at the matrix equation

$$(\boldsymbol{F} + \boldsymbol{G})\boldsymbol{C}^\alpha = \boldsymbol{H}^\alpha \qquad (2.50)$$

where the F-, G- and H-matrices are

$$F_{j\lambda, j'\lambda'} = \sum_{i=1}^{I} \sum_{q=1}^{Q} M_{ij\lambda}(r_q) M_{ij'\lambda'}(r_q) \qquad (2.51\mathrm{a})$$

$$G_{j\lambda, j'\lambda'} = \delta_{jj'} \phi_\lambda^j(r_B) \phi_{\lambda'}^{j'}(r_B) \qquad (2.51\mathrm{b})$$

$$H_{j\lambda}^\alpha = d_j^\alpha \phi_\lambda^j(r_B). \qquad (2.51\mathrm{c})$$

The above method is called the *method of least-squares*.

We note at this point that the placement of the nodes (mesh points) r_q in the functional (2.45) is completely arbitrary. Theoretically, the choice should not be critical providing that there are enough points to avoid linear dependences in the final matrix equation (2.50). In practice this is not always so easy; a poor choice of points quickly leads to ill-conditioning in (2.50) as the number of channels, I, increases. This ill-conditioning can become so extreme, even for a modest number of channels, that, even with double precision arithmetic, the method becomes unreliable. What we need, therefore, is some prescription with which to reliably determine a suitable placement of the nodes.

Introducing weights w_q to the functional so that it now reads[15]

$$I^\alpha = \sum_{i=1}^{I} \sum_{q=1}^{Q} \left[\sum_{j=1}^{I} L_{ij} f_j^\alpha(r_q) w_q \right]^2 + \sum_{i=1}^{I} \left[f_i^\alpha(r_B) - d_i^\alpha \right]^2. \tag{2.52}$$

we note the similarity of the contents of the brackets in the first term to a numerical integral.[16] Now, defining a norm

$$N^\alpha = \sum_{i=1}^{I} \int_0^{r_i} dr \left[\sum_{j=1}^{I} L_{ij} f_j^\alpha(r) \right]^2, \tag{2.53}$$

which we note is equivalent to $\int dr |(H - E)\psi|^2$, and introducing this into the definition of the functional (2.52) we may impose restrictions on the choice of nodes r_q and weights w_q by demanding that they are given by a quadrature rule. A particular choice of rule might be, say, a Gaussian rule [105]; however, due to the sometimes large number of basis functions ϕ_λ^i necessary in the wavefunction expansion (2.43) it is convenient to instead split the integral into subranges: symbolically

$$\int_0^{r_i} \longrightarrow \int_0^{x_1} + \int_{x_1}^{x_2} + \cdots + \int_{x_{n-1}}^{r_i}, \tag{2.54}$$

what is known as a compound Gaussian rule. We may now choose lower order rules for each interval. This method, a generalisation of the least-squares method, is called the *minimum-norm method*.

A further generalisation is found by introducing more weights $\overline{w}_q$ into the quadrature. These weights are chosen to be equal within each subrange in order to maintain the quadrature rules but may be chosen arbitrarily between subranges. It is found that this additional degree of freedom, although not really necessary for good results with the sizes of calculation performed in this thesis, noticeably improves the performance of the algorithm further in some cases when the weights $\overline{w}_q$ are chosen suitably. For now, the issues of choices of compound rules, total number of nodes, application of additional weighting factors and division into subranges and how the performance of the algorithm is affected will be skipped and instead discussed in chapter 3.

2.5 Solution in the Asymptotic Region; the T-Matrix and Cross Sections

Having discussed the solution of the scattering equations in the inner region we now move on to discuss the solution in the asymptotic region. This is defined as the region in which physical scattering observables, such as the cross sections, are defined, and in which, in an experimental apparatus, the detectors would be situated. We show in this section how the asymptotic forms of the solutions to the scattering equations enable the the reaction (K-) matrix, the scattering (S-) matrix and the transition (T-) matrix to be determined, from which the cross sections may be computed. We also only give a brief overview, collecting together the more important results; for a more comprehensive discussion the reader is referred to, for example, [97, 98, 106, 107].

In the asymptotic region we assume that the couplings between channels are negligible and hence we may consider solutions to the radial (partial wave) equation

$$[L_l - U]f_l = 0. \tag{2.55}$$

Here, L_l is the operator (2.12) for a single channel only and acting on an angular momentum of l, $U = U(r)$ is the reduced potential and f_l is the radial wavefunction with orbital angular momentum l. It may be shown [106] that cases in which the potential, $U(r)$, vanishes faster than r^{-1}, it is sufficient, in the asymptotic region, to consider the solutions to the free-particle equation

$$L_l f_l = 0. \tag{2.56}$$

However, in the case of a residual Coulomb force, such as in e$^+$-He$^+$ scattering considered in this thesis, this residual force *must* be retained since it remains strong enough to result in a distortion of the asymptotic wave manifested by the addition of an extra, logarithmic, phase factor.

Consider firstly a potential of pure Coulomb form, i.e.

$$U(r) = -\frac{2\gamma k}{r} = -\frac{2\gamma k^2}{\rho}, \tag{2.57}$$

where $\rho = kr$. The solution to (2.55) regular at the origin is the spherical Coulomb function

$$F_l = C_l\, e^{i\rho}(\rho)^{l+1}\, {}_1F_1(l+1+i\gamma; 2l+2; -2i\rho), \qquad (2.58)$$

where C_l is a constant, which has the asymptotic form

$$F_l \underset{\rho\to\infty}{\sim} \sin(\rho - \tfrac{1}{2}l\pi - \gamma\ln 2\rho + \sigma_l); \qquad (2.59)$$

σ_l is the Coulomb phase shift

$$\sigma_l = \arg\Gamma(l+1+i\gamma), \qquad (2.60)$$

which, for $\gamma = 0$, becomes $\sigma_l = 0$.

In order to completely specify the solution we must also introduce a second independent solution, the irregular Coulomb function, G_l, given by

$$\begin{aligned}
G_l = iC_l\, e^{i\rho}(\rho)^{l+1}\big[&W_1(l+1+i\gamma, 2l+2, -2i\rho) \\
&- W_2(l+1+i\gamma, 2l+2, -2i\rho)\big]
\end{aligned} \qquad (2.61)$$

$$\underset{\rho\sim\infty}{\sim} \cos(\rho - \tfrac{1}{2}l\pi - \gamma\ln 2\rho + \sigma_l).$$

It is also convenient to define two additional irregular functions

$$\begin{aligned}
H_l^{(\pm)} &= \exp(\pm i\sigma_l)\left(F_l \pm iG_l\right) \\
&\underset{\rho\sim\infty}{\sim} \mp i\exp\{\pm i(\rho - \tfrac{1}{2}l\pi - \gamma\ln 2\rho)\}
\end{aligned} \qquad (2.62)$$

so that the full scattering solution can be written

$$f_l = A_l^c[H_l^{(-)} - S_l^c H_l^{(+)}]. \qquad (2.63)$$

Here, S_l^c is termed the S-matrix which is related to the Coulomb phase shift by

$$S_l^c = \exp\{2i\sigma_l(k)\} = \frac{\Gamma(l+1+i\gamma)}{\Gamma(l+1-i\gamma)}. \qquad (2.64)$$

In a more realistic collision problem the Coulomb force will be modified by some short range potential, $\tilde{U}(r)$, which vanishes faster than r^{-1}, i.e.

$$U(r) = \tilde{U}(r) - \frac{2\gamma k}{r}. \qquad (2.65)$$

The short range component of this potential is such that beyond a certain point it may be dropped from the radial equation leaving the Coulomb equation. In analogy with neutral scattering we write the general solution in the asymptotic region as

$$f_l = \tilde{A}_l^c [F_l + K_l G_l] \tag{2.66}$$

where K_l is termed the reaction matrix or K-matrix. On putting $K_l = \tan \delta_l$ (2.66) is found to have the asymptotic form

$$f_l \underset{\rho \to \infty}{\sim} \sin(\rho - \tfrac{1}{2} l\pi - \gamma \ln 2\rho + \sigma_l + \delta_l). \tag{2.67}$$

Comparison with (2.59) shows that the effect of a short range potential superimposed on the Coulomb potential is to replace the Coulomb phase shift, σ_l, with a phase shift $\Delta_l = \sigma_l + \delta_l$, where the phase shift δ_l contains all the information on the non-Coulombic part of the potential. The solution may also be written as

$$f_l = \tilde{A}_l^{c'} [H_l^{(-)} + e^{2i\Delta_l} H_l^{(+)}]. \tag{2.68}$$

Now, extending this to the multichannel case, we write instead the matrix equation

$$f_l \underset{r \to \infty}{\sim} k^{-1/2} \left(F_l + K_l G_l \right) \tag{2.69}$$

where now f, $k^{-1/2}$, F_l and G_l are diagonal matrices. We define the transition matrix, or T-matrix, by

$$T_l = \frac{K_l}{1 - iK_l}, \tag{2.70}$$

which is related to the S-matrix by

$$S_l = 1 + 2iT_l, \tag{2.71}$$

from which we may compute the cross sections[17]

$$\sigma_f = \frac{4\pi}{k_i^2} \sum_{l=0}^{\infty} (2l + 1) \left| T_{fi}^l \right|^2. \tag{2.72}$$

For computational convenience, as we shall see in the next section, we also define the R-matrix or inverse log-derivative matrix, R_l, at the points $r_i = a_i$ by

$$\mu^{-1/2} k^{-1/2} a^{-1/2} \left. f_l \right|_{r=a} = R_l \mu^{-1/2} k^{-1/2} a^{1/2} \left. f_l' \right|_{r=a}. \tag{2.73}$$

Here, $\mu^{-1/2}$ is a diagonal matrix with elements $\mu_i^{-1/2}$, where μ_i is the reduced mass in the ith channel and, similarly, the matrices $a^{\pm1/2}$ are diagonal matrices with elements $a_i^{\pm1/2}$. Incidentally, the factor of a in (2.73) is not necessary but it is customary to include it. The notation $\left. \right|_{r=a}$ denotes evaluation at the points $r_i = a_i$ and the prime denotes the derivative with respect to the corresponding radial variable, r_i.

2.6 Solution in the Intermediate Region: R-Matrix Propagation

Having solved the scattering equations in the internal and asymptotic regions, what remains is to solve the scattering equations in the intermediate region inbetween. In this region the potentials are local and hence the scattering equations are purely differential in form, i.e. they contain no integral terms. Such coupled second-order linear differential equations may be solved by direct integration, for example using a Runge-Kutta method [88]; however, it is far more convenient to use one of a number of well established dedicated packages which are available [108–110], upholding the principle of software re-use.

In the previous section the R-matrix was defined; from equation (2.73) it is clear that knowledge of the R-matrix is sufficient in order to determine the scattering K-matrix and hence also the cross sections. The above mentioned packages are termed R-matrix propagators since they work by propagating the R-matrix from one point, which in our case will be at the edge of the internal region, to another, usually in the asymptotic region. Use of an R-matrix propagator is clearly advantageous since, by defining an intermediate region, the size of the inner region over which the least-squares expansion is made may be reduced with a considerable reduction in the amount of computation.

In this section we discuss how this propagation is performed. *R*-matrix propagation techniques have also been discussed by a number of authors, including [100, 101, 107, 109–112].

In the intermediate region, the two components of the wavefunction Ψ_D^{JM} and Ψ_X^{JM} can be solved for separately. The Schrödinger equation thus separates into two equations

$$[H - E]\Psi_D^{JM} = 0 \qquad (2.74a)$$

and

$$[H - E]\Psi_X^{JM} = 0. \qquad (2.74b)$$

Similarly to before, projecting these two equations onto the channel functions $\overline{\phi}_{\alpha L_\alpha l_\alpha}^{JM}(\boldsymbol{r}, \hat{x})$ and $\overline{\psi}_{\gamma L_\gamma l_\gamma}^{JM}(\boldsymbol{R}, \hat{\rho})$, we obtain the two sets of differential equations

$$\left(\frac{d^2}{dx^2} - \frac{L_\alpha(L_\alpha + 1)}{x^2} - 2\left(\frac{Z-1}{x}\right) + k_\alpha^2 \right) f_{\alpha, L_\alpha}^J(x) =$$
$$-2\sum_\lambda \sum_\beta a_{\alpha\beta}^\lambda x^{-\lambda-1} f_{\beta, L_\beta}^J(x) \qquad (2.75a)$$

and

$$\left(\frac{d^2}{d\rho^2} - \frac{L_\gamma(L_\gamma + 1)}{\rho^2} + k_\gamma'^2 \right) g_{\gamma, L_\gamma}^J(\rho) = -4\sum_\lambda \sum_\delta \overline{a}_{\gamma\delta}^\lambda \rho^{-\lambda-1} g_{\delta, L_\delta}^J(\rho). \qquad (2.75b)$$

Here, the potential on the right-hand side has been given in multipole form where the multipole coefficients, $a_{\alpha\beta}^\lambda$ and $\overline{a}_{\gamma\delta}^\lambda$, are given by

$$a_{\alpha\beta}^\lambda = \left\langle \overline{\phi}_{\alpha L_\alpha l_\alpha}^{JM} \left| r^\lambda P_\lambda(\cos\Theta) \right| \overline{\phi}_{\beta L_\beta l_\beta}^{JM} \right\rangle \qquad (2.76a)$$

and

$$\overline{a}_{\gamma\delta}^\lambda = Z \left\langle \overline{\psi}_{\gamma L_\gamma l_\gamma}^{JM} \left| \left(\tfrac{1}{2}R\right)^\lambda \left[1 - (-)^\lambda\right] P_\lambda(\cos\overline{\Theta}) \right| \overline{\psi}_{\delta L_\delta l_\delta}^{JM} \right\rangle; \qquad (2.76b)$$

Θ is the angle between $\boldsymbol{r}$ and $\boldsymbol{x}$; $\overline{\Theta}$ is the angle between $\boldsymbol{R}$ and $\boldsymbol{\rho}$.[18] The multipole expansion of the potential is advantageous since it reduces the amount of computation involved in computing the potentials; at this range only a few terms need be retained in the expansion. Equations (2.75) may be written in matrix form

$$(\mathcal{H} - \mathcal{E})f = 0 \qquad (2.77)$$

where f is a vector comprised of elements $f^J_{\alpha,L_\alpha}(x)$ and $g^J_{\gamma,L_\gamma}(\rho)$; $\mathcal{H}$ is block diagonal, with upper and lower blocks

$$
\mathcal{H}_{\alpha\beta} = -\frac{1}{2\mu_\alpha}\left(\frac{\mathrm{d}^2}{\mathrm{d}x^2} - \frac{L_\alpha(L_\alpha+1)}{x^2} - 2\left(\frac{Z-1}{x}\right) + k_\alpha^2 - 2\mu_\alpha k^2\right)
$$
$$
- \sum_{\lambda,\beta} a^\lambda_{\alpha\beta}x^{-\lambda-1}
\tag{2.78}
$$
$$
\mathcal{H}_{\gamma\delta} = -\frac{1}{2\mu_\gamma}\left(\frac{\mathrm{d}^2}{\mathrm{d}\rho^2} - \frac{L_\gamma(L_\gamma+1)}{\rho^2} + k'^2_\gamma - 2\mu_\gamma k^2\right) - \sum_{\lambda,\delta} \bar{a}^\lambda_{\gamma\delta}\rho^{-\lambda-1}
$$

respectively and all other elements zero; $\mathcal{E}$ is the diagonal matrix

$$
\mathcal{E}_{ij} = k^2\delta_{ij}.
\tag{2.79}
$$

We note that the choice of k^2 is arbitrary and may be chosen to be whatever is most convenient. μ_i is the reduced mass in the ith channel where i runs through α and γ.

In order to proceed with the R-matrix propagation we divide the intermediate region up into sectors; the aim is to propagate the R-matrix in steps, one sector at a time. In order to do this we first define the *modified Bloch operator* matrix

$$
[\mathcal{L}_B(a;b)]_{ij} \equiv [L_B(b) - L_B(a)]\,\delta_{ij}, \qquad b > a
\tag{2.80}
$$

where the *Bloch operator* [113, 114], L_B, is defined by

$$
L_B(a) \equiv \begin{cases} \dfrac{1}{2}\sum_i \delta(x-x_a)|\bar{\phi}_i(\mathbf{r},\hat{x})\rangle\left[\dfrac{\mathrm{d}}{\mathrm{d}x} + \dfrac{1}{x}\right]\langle\bar{\phi}_i(\mathbf{r},\hat{x})| & \text{direct channels} \\[3mm] \dfrac{1}{4}\sum_i \delta(\rho-\rho_a)|\bar{\psi}_i(\mathbf{R},\hat{\rho})\rangle\left[\dfrac{\mathrm{d}}{\mathrm{d}\rho} + \dfrac{1}{\rho}\right]\langle\bar{\psi}_i(\mathbf{R},\hat{\rho})| & \text{exchange channels.} \end{cases}
\tag{2.81}
$$

The purpose of the Bloch operator is that it ensures the Hermiticity of the operator $\mathcal{H} + \mathcal{L}_B$ over the region $[a,b]$.[19]

Now, rewriting (2.77) as

$$
(\mathcal{H} + \mathcal{L}_B - \mathcal{E})f = \mathcal{L}_B f,
\tag{2.82}
$$

which has the formal solution

$$
f = (\mathcal{H} + \mathcal{L}_B - \mathcal{E})^{-1}\mathcal{L}_B f,
\tag{2.83}
$$

this depends on the number of nodes of the wavefunction within the sector and is thus related to the channel momentum. Following Baluja *et al* [110], ten shifted-Legendre basis functions were employed in this work and the sector width was chosen by the criterion

$$k_{\mathrm{max}} |b - a| = 6; \qquad (2.89)$$

here $k_{\mathrm{max}} = \max\{|k_i|; \forall i\}$ is the maximum absolute wavenumber of all channels. This criterion was chosen empirically by Baluja *et al* .

The above propagation technique is called a *solution following* method. The method is considered computationally efficient for the problems considered in this thesis; a great deal of the calculation, namely the construction of the basis within each sector, need only be done once for all energies; for each energy only the $\mathfrak{R}$-matrices need to be constructed and the propagation equation (2.88a) evaluated. An alternative method due to Light and Walker [101, 111, 112] instead works by diagonalising the interaction potential in the centre of each sector. The sector size is thus governed by the rate with which the potential varies, since it is assumed to be constant across each sector. The advantage of this method is clear when the potential is slowly varying and can often be more computationally efficient than the solution following method. The best choice is thus the one which is most suited to a particular problem; alternatively a combination of the two may be used [109].

2.7 Other Methods of Solution

The R-Matrix Method

The R-matrix was first introduced by Wigner and Eisenbud [115–117] in the context of nuclear reaction theory and has since been discussed by a number of other authors [32, 33, 107, 118–120]. It has been used extensively in atomic collision theory, both for electron-atom [120, 121] and, more recently, positron-atom collisions [21, 28–33, 68–70].

Like the least-squares and minimum-norm methods, the R-matrix method works in a partitioned configuration space consisting of an inner region, in which the po-

tentials must all be treated fully, and an external region in which the exchange potentials are negligible and the local potentials may be approximated by multipole expansions and propagated by standard methods [101, 108–111]. Accordingly, the total wavefunction is also divided into two parts which are matched at the R-matrix boundary on the division between the internal and external regions.

For brevity, limiting our discussion to an expansion over the direct partition only, in the internal region the total wavefunction is expanded in terms of a complete basis, Ψ_k, given by

$$\Psi_k = \sum_{ij} \overline{\phi}_i(\boldsymbol{r}, \hat{x}) \frac{1}{x} u_j(x) a_{ijk}. \tag{2.90}$$

Here, the co-ordinates are the same as for the least-squares method and $\overline{\phi}_i(\boldsymbol{r}, \hat{x})$ are channel functions, defined in the same way as before. The functions $u_j(x)$, termed *continuum orbitals,* may be chosen somewhat arbitrarily, although they must come from a complete set and there must be enough of them to ensure completeness in the expansion of Ψ_k. Given the appropriate normalisation the coefficients, a_{ijk}, may be determined by diagonalising the Hamiltonian,

$$\langle \Psi_k | H + L_B | \Psi_{k'} \rangle = E_k \delta_{kk'}, \tag{2.91}$$

where H is the total Hamiltonian such that the wavefunction over all space, Ψ, obeys the equation

$$(H - E)\Psi = 0 \tag{2.92}$$

and the integration in (2.91) is to be performed over the inner region only. The operator L_B is the Bloch operator (2.81), again introduced to ensure Hermiticity in the internal region. The complete solution over the internal region, wavefunction Ψ^{int}, may be written as

$$(H + L_B - E)\Psi^{\text{int}} = L_B \Psi^{\text{int}}. \tag{2.93}$$

Expanding this in terms of the complete set of basis states Ψ_k we have

$$|\Psi^{\text{int}}\rangle = \sum_k |\Psi_k\rangle \frac{1}{E_k - E} \langle \Psi_k | L_B | \Psi^{\text{int}} \rangle. \tag{2.94}$$

Projecting onto the channel functions, $\overline{\phi}_i(\boldsymbol{r}, \hat{x})$, and evaluating on the R-matrix boundary, $x = a$, yields

$$f_i(x)\Big|_{x=a} = \sum_j R_{ij} \frac{\mathrm{d}f_j(x)}{\mathrm{d}x}\Big|_{x=a} \qquad (2.95)$$

Here, $f_i(x)$ are the reduced channel wavefunctions and R_{ij} we recognise as being the R-matrix, given here by

$$R_{ij} = \frac{1}{2} \sum_{k=1}^{N} \frac{w_{ik} w_{jk}}{E_k - E}. \qquad (2.96)$$

The functions w_{ik} are termed *surface amplitudes* and are given by

$$x^{-1} w_{ik}(x) = \left\langle \overline{\phi}_i(\boldsymbol{r}, \hat{x}) \big| \Psi_k \right\rangle \qquad (2.97)$$

and the radial functions f_i are given by

$$x^{-1} f_i(x) = \left\langle \overline{\phi}_i(\boldsymbol{r}, \hat{x}) \big| \Psi^{\mathrm{int}} \right\rangle. \qquad (2.98)$$

It is straightforward to develop the R-matrix method to also include the positronium formation channels; see, for example, Higgins and Burke [32].

We see that with the R-matrix method the majority of the computation lies in the diagonalisation (2.91); once this diagonalisation has been performed the surface amplitudes and the radial functions are readily constructed and all that remains is for the R-matrix (2.96) to be evaluated.

Variational Methods

Although variational methods were developed for bound state problems in the early days of quantum mechanics, it took until about 1944 for the variational method to be developed for scattering problems. The development has since had a significant impact on scattering calculations and has been used widely on many problems.[20] Variational methods in scattering theory hold certain similarities with the Rayleigh-Ritz[21] theory for bound state problems (they both provide stationary functionals) except for two notable exceptions: whilst the Rayleigh-Ritz principle provides an upper bound to an exact energy and also provides parameters which determine

the wavefunction, the variational methods of scattering theory do not, in general, provide variational bounds, except in special cases; the energy is also specified in advance and the variational principle is used to determine other properties, such as scattering lengths, phase shifts, etc. In this section we discuss only a few of the more important aspects of variational theory; for a more comprehensive account of variational methods in scattering theory plus references see, for example, Bransden [97], Joachain [106], Burke and Joachain [107], or the monograph by Nesbet [122].

Variational methods of the Hulthén-Kohn type [123–125] are often based on variational principles of the form

$$\delta[I_l^t + k\eta_l^t] = 0, \tag{2.99}$$

where η_l^t is a trial phase shift,

$$I_l^t[f_l^t] = \int_0^\infty f_l^t \mathcal{L}_l f_l^t \mathrm{d}r, \tag{2.100}$$

f_l^t is a trial wavefunction with flexible parameters and obeying the boundary condition

$$f_l^t(r) \underset{r\to\infty}{\sim} \sin(kr - \tfrac{1}{2}l\pi) + \tan(\eta_l^t - \tau)\cos(kr - \tfrac{1}{2}l\pi) \tag{2.101}$$

and τ is a flexible parameter, The variationally correct phase shift, $[\eta_l]$, is then given by

$$[\eta_l] = \eta_l^t + k^{-1}I_l^t. \tag{2.102}$$

Values of the parameter $\tau = 0$ and $\pi/2$ produce the so-called Kohn and inverse Kohn methods respectively. Variational methods based on a normalisation of the form

$$f_l^t(r) \underset{r\to\infty}{\sim} \exp(-i\theta_l) - S_l^t(k)\exp(i\theta_l) \tag{2.103}$$

give rise to the variational principle

$$\delta[I_l^t - 2ikS_l^t] = 0 \tag{2.104}$$

from which the variationally correct S-matrix, $[S_l]$, is found to be

$$[S_l] = S_l^t + \frac{1}{2ik} I_l[f_l^t].$$

(2.105)

This method, which is often termed the complex Kohn method, has been employed in positron scattering by Van Reeth and Humberston [74, 75].

A notable problem of the Kohn and inverse Kohn variational methods is that they suffer from so-called Schwartz singularities [126, 127]; i.e. no matter how flexible the trial function is made if you are on, or close to, a singularity the method is hopeless. The problem has been addressed in two ways: (1) use a combination of variational principles, such as the Kohn and inverse Kohn [20], since the singularities occur in different places; and (2) a method developed by Harris [128] overcomes the problem by enabling the evaluation directly on the singularities. The former method has been used in positron-hydrogen collisions by Humberston *et al* [22–25, 75] whilst the Harris method has been employed by Shimamura [129]. Unfortunately the Harris method is restricted to points on the singularities only, although the singularities can be moved by alterations of the trial wavefunction.

A variational principle for the R-matrix has been given by Jackson [130] and generalised by Bransden and Noble [2] to give a variationally correct R-matrix for the least-squares method. The correction was found, however, to be negligible. Also, variational principles of integral form have been introduced by Schwinger [131] and used in positron-hydrogen collisions by Kar and Mandal [132].

Hyperspherical Close Coupling

The Hyperspherical Close Coupling (HSCC) method has been used by several authors in the study of positron-atom/-ion collisions [34–37] and has been reviewed by Lin [133]. The method has been discussed in some detail for the case of positron-hydrogen scattering by Igarashi and Toshima [34].

The problem is formulated in hyperspherical coordinates: the hyperradius, $\rho = \sqrt{r^2 + x^2}$, and the hyperangle, $\phi = \tan^{-1}(r/x)$, replace the radial coordinates of the electron and positron, r and x, and Ω denotes the five angular variables $(\phi, \hat{x}, \hat{r})$.

The total Hamiltonian, H, is written as

$$H = -\frac{1}{2}\left(\frac{\partial^2}{\partial \rho^2} + \frac{5}{\rho}\frac{\partial}{\partial \rho}\right) + h_{\text{ad}}(\rho;\Omega) \tag{2.106}$$

which defines the *adiabatic Hamiltonian*, $h_{\text{ad}}(\rho;\Omega)$, obtained by fixing the value of the hyperradius, ρ, and contains the interparticle potentials. *Adiabatic channel functions*, $\psi_\mu(\rho;\Omega)$, are obtained by diagonalising $h_{\text{ad}}(\rho;\Omega)$ using a suitable basis which, asymptotically, represent the correct physical channels. The total wavefunction of the system, Ψ, is then expanded as

$$\Psi(\rho,\Omega) = \sum_\mu \rho^{-5/2} F_\mu(\rho)\psi_\mu(\rho;\Omega). \tag{2.107}$$

Substitution of (2.107) into the Schrödinger equation then leads to coupled radial equations for $F_\mu(\rho)$ of the form

$$\left(-\frac{1}{2}\frac{d^2}{d\rho^2} + U_\mu(\rho) - E\right)F_\mu(\rho) + \sum_\nu V_{\mu\nu} F_\nu(\rho) = 0, \tag{2.108}$$

where the potentials, $V_{\mu\nu}$, are purely local. These equations are referred to as the *hyperspherical close coupling equations* and can be solved by standard methods for differential equations.

There are a number of advantages of the hyperspherical approach: (1) the scattering equations are purely differential in form once the adiabatic trial functions have been calculated, without the complication of a nonlocal potential term as is the case in close coupling studies; (2) the hyperspherical adiabatic basis takes into account fully the distortion of the target due to polarisation effects and thus smears out all traces of pseudoresonance effects found with close coupling calculations [34]; and (3) analysis of the adiabatic hyperspherical potentials can give insight into the existence of resonances and help in classifying them into Feshbach and shape resonances.

There are also, however, some problems that have been identified: (1) the nonadiabatic couplings are sharply peaked in the vicinity of avoided crossings in the adiabatic potentials and the presence of many avoided crossings leads to ill-conditioning in the coupled equations; (2) the error in closed channel components in some solutions can sometimes overwhelm the calculation making it difficult to obtain linearly

independent solutions, which is necessary for matching to the asymptotic bound-ary conditions to calculate the scattering K-matrix (a problem particularly when the centrifugal barrier is high); and (3) as the total angular momentum, J, is increased, so more and more basis functions need to be used in order to obtain accurate adiabatic states, which leads to linear dependency problems with certain basis sets [34].

The first of these problems is treated by the *diabatic-by-sector method* in which the region of ρ is divided up into small sectors and in sectors where an avoided crossing occurs the adiabatic channel function is instead replaced by one evaluated at the midpoint of the sector. These functions are referred to as piecewise diabatic functions since they are independent of ρ over that sector. In actual calculations the sectors are made small enough so as to maintain unitarity between sectors to a certain accuracy.

In spite of the above problems the HSCC method has so far performed favourably when compared to accurate variational and close coupling methods and, due to the often more complete expansion of the channel functions, offers a useful comparison. By inspection of the adiabatic channel functions it is also possible to classify reso-nances or, if a resonance reported by another calculation cannot be found, provide persuasive arguments as to why it should not exist and may simply be a product of the other model. This has been the case with disputed resonances in e^+-He^+ scattering [37].

Momentum Space Methods

Up until now we have discussed the solution of the scattering equations in configu-ration space only. This is often a choice of convenience; however, it is equally valid to instead formulate the problem in momentum space.

Beginning with the Lippmann-Schwinger equation for the T-matrix

$$T = V + G_0 T, \qquad (2.109)$$

where G_0 is the free-particle Green's function, and writing this in momentum space,

we have the coupled equations

$$\langle k'\alpha' |T| k\alpha\rangle = \langle k'\alpha' |V| k\alpha\rangle$$

$$+ \sum_{\alpha''} \int dk'' \frac{\langle k'\alpha' |V| k''\alpha''\rangle \langle k''\alpha'' |T| k\alpha\rangle}{E + i\varepsilon - E_{\alpha''}} \qquad (2.110a)$$

$$+ \sum_{\beta''} \int dk'' \frac{\langle k'\alpha' |V| k''\beta''\rangle \langle k''\beta'' |T| k\alpha\rangle}{E + i\varepsilon - E_{\beta''}}$$

$$\langle k'\beta' |T| k\alpha\rangle = \langle k'\beta' |V| k\alpha\rangle$$

$$+ \sum_{\alpha''} \int dk'' \frac{\langle k'\beta' |V| k''\alpha''\rangle \langle k''\alpha'' |T| k\alpha\rangle}{E + i\varepsilon - E_{\alpha''}} \qquad (2.110b)$$

$$+ \sum_{\beta''} \int dk'' \frac{\langle k'\beta' |V| k''\beta''\rangle \langle k''\beta'' |T| k\alpha\rangle}{E + i\varepsilon - E_{\beta''}}$$

Here, the interaction elements, generically labelled V, are Born matrix elements of the form

$$\langle k'\alpha' |V| k\alpha\rangle = \left\langle k'\alpha' \left| \frac{1}{x} - \frac{1}{|r - x|} \right| k\alpha \right\rangle \qquad (2.111)$$

$$\langle k'\beta' |V| k\beta\rangle = \left\langle k'\beta' \left| \frac{1}{|R - \frac{1}{2}\rho|} - \frac{1}{|R + \frac{1}{2}\rho|} \right| k\beta \right\rangle \qquad (2.112)$$

$$\langle k'\beta' |V| k\alpha\rangle = \langle k'\beta' |H - E| k\alpha\rangle \qquad (2.113)$$

where equations (2.111) and (2.112) are direct matrix elements and (2.113) are rearrangement matrix elements.

By making substitutions of the form

$$\langle k'\alpha' |V| k\alpha\rangle = \sum \langle L'l_{\alpha'}; M'm_{\alpha'}|JM\rangle \langle Ll_\alpha; Mm_\alpha|JM\rangle \times$$

$$Y^*_{L'M'}(\hat{k}')Y_{LM}(\hat{k})V^J_{\alpha'L'\alpha L}(k',k) \qquad (2.114)$$

and similarly for the T-matrix elements, the Lippmann-Schwinger equations (2.110) may be partial-wave analysed, reducing to single variable equations which may then be solved by discretising using a suitable numerical quadrature to produce a set of linear equations [44].

The advantages of the momentum space formalism are (1) the boundary conditions are already incorporated into the Lippmann-Schwinger equations and so

need not be included separately; (2) the scattering information is obtained directly from the equations; and (3) the matrix elements are better behaved than the corresponding ones in configuration space (as we'll be finding out in chapter 3). The Lippmann-Schwinger equations may equally well be formulated in configuration space too, retaining advantages (1) and (2); however, the Green's functions are found to be oscillatory in character resulting sometimes in a large number of quadrature points being required when discretising the equations. The momentum space formalism has been used in atomic physics by Hewitt *et al* [53] and Mitroy and Stelbovics [49].

Methods for Complex Targets

In the case of positron scattering, of all the methods discussed so far, most of them have only been applied to simple one-electron systems or to multielectron systems employing effective potentials. Of particular note, however, is the *R*-matrix method which has recently been extended successfully to the two electron problem by Campbell *et al* [21]. Treatment of two electron problems with the above methods is very difficult though. Two reasons for the increased complexity are: (1) the presence of electron-electron exchange kernels between the positronium and the remaining target electron(s); and (2) possible states of the residual ion which may have to be included in the wavefunction expansion as well as the positronium states. It is thus useful to develop various approximation methods for dealing with these complex targets. Two approximation methods for dealing with complex targets particularly worth mentioning have been developed. These are the optical potential and polarised orbital methods. We discuss each of these in turn.

Firstly the optical potential method. Following the projection operator formalism of Feshbach [134, 135] we define two operators, P and Q, which project one or more of the open channels and the remainder of the channels (including all closed channels) out of the wavefunction respectively and have the properties

$$P + Q = 1; \qquad P^2 = P; \qquad Q^2 = Q; \qquad PQ = QP = 0. \qquad (2.115)$$

We may now write the wavefunction as $\psi = (P + Q)\psi$. Inserting this into the

Schrödinger equation $(H - E)\psi = 0$, operating on the left separately with P and Q and rearranging we obtain the equivalent equation

$$(H_{PP} + V_{\text{opt}} - E_{PP})\psi = 0 \qquad (2.116)$$

where $H_{PQ} = PHQ$ etc. and the optical potential is given by

$$V_{\text{opt}} = H_{PQ}[Q(E - H)Q]^{-1}H_{QP}. \qquad (2.117)$$

It should be noted that equation (2.116) is equivalent to the Schrödinger equation and no approximation has yet been made. The problem is in how the Green's function $[Q(E-H)Q]^{-1}$ is computed. The method may be developed for computing the elastic scattering cross section only or the ground state positronium formation channel may also be included; it has been employed by Gianturco and Melissa [81–83] for computing positronium formation cross sections for a variety of targets. Determination of the Green's function is, however, highly nontrivial for most targets and is far beyond the scope of this thesis; the reader is instead referred to, for example, Gianturco and Melissa.

Construction of optical potentials has also been discussed by Bransden *et al* [136] with particular application to the interpretation of the broad s-wave resonance found in the coupled-static model of positron-hydrogen scattering. In their paper, Bransden *et al* solved the coupled equations and used the solution to construct optical potentials, $W_n(r, r')$, for the two channels; these potentials were then localised. It should be noted that these local optical potentials, which may be complex, are approximate potentials only and cannot reproduce the exact scattering parameters and radial wavefunctions; it was in fact found, however, that they could reproduce almost idential asymptotic radial wavefunctions and very similar phase shifts. Using the optical potentials they were able to demonstrate the existence of a deep potential well on resonance centred at around $r \approx 3$ a.u. with a corresponding rise in the amplitude of the radial wavefunction between the origin and the first node. These observations are strongly suggestive of the formation of a compound state, the product of a shape resonance.

The second method that has been developed for dealing with complex targets represents the closed channel part of the wavefunction, $Q\psi$, by introducing a po-

larisation potential, $W_P(x)$, as in

$$\left(\nabla_x^2 + k^2 - U(x) - W_P(x)\right) F(x) = 0, \qquad (2.118)$$

where $U(x)$ is the static potential. Various forms of $W_P(x)$ have been derived by various authors. Methods which neglect the kinetic energy of the incident positron and exclude exchange are termed adiabatic polarisation methods. Better approximations include exchange effects (so-called exchange-adiabatic methods) and better results are achieved if short-range diabatic effects are also accounted for in some way. These have been discussed in some detail by Bransden [9] and are not discussed here.

The above methods are members of a group of approximations called the Polarised Orbital (PO) method. The PO method has been employed for the case of positron-hydrogen scattering by, for example, Khan and Ghosh [137]. In their case exchange arising from positronium formation was neglected which they concluded should in fact be included.

Notes

[1] In the spherically symmetric case it is convenient to work in spherical polar co-ordinates r, θ, ϕ. Since we have azimuthal symmetry the scattering wavefunction will be a function of r and θ only. The Legendre polynomials $P_l(\cos\theta)$ form a complete set over the interval $\cos\theta \in [-1, 1]$ and hence the expansion (2.8) follows.

[2] A simple example is that of electron-hydrogen scattering in which excitation of the hydrogen target is not taken into account (only one term in the target expansion): the so-called *static exchange approximation*. In this case the resulting radial equation takes on the form

$$\left(\frac{\mathrm{d}^2}{\mathrm{d}r_1^2} - \frac{l(l+1)}{r_1^2} + k_0^2\right) f_l^S(r_1) = U(r_1)f_l^S(r_1) +$$

$$(-)^S \int_0^\infty K_l(r_1, r_2)f_l^S(r_2)\mathrm{d}r_2.$$

Here, $U(r_1)$ is the local component of the potential and $K(r_1, r_2)$, sometimes termed the exchange kernel, describes the non-local part; r_1 and r_2 are the co-ordinates

of the two electrons relative to the proton; l is the scattering angular momentum (equal in this case to the total angular momentum); and S denotes the total spin: $S = 0$ or 1 triplet or singlet respectively.

[3]In fact, even closed channels can have quite a profound effect on the results, since closed channels may contribute significantly to polarisation forces acting upon the projectile. This is also true below the first threshold in which only elastic scattering is possible, however it can be shown that the phase shift obtained in this way satisfies a lower bound principle (see, for example, [97] and references cited therein).

[4]The static interaction is the potential if only one term is retained in the close coupling expansion and exchange is neglected, i.e. $U_{00}(r_2)$.

[5]This complication, however, reappears in an even nastier form when multi-electron targets are considered, since now electron exchange between the formed positronium and residual target may have to be taken into account. Positron scattering by alkali targets has been studied by a number of authors, including [68–70].

[6]If positive energy states are included on both centres, i.e. in both terms on the right-hand side of equation (2.16), the question does arise, however, of the possibility of double-counting when calculating cross sections. See, for example, Kerhoghan *et al* [29] or Kadyrov and Bray [40].

[7]In the case of positron-atom scattering, in which the possible rearrangement of the particles has been explicitly taken into account, this is not strictly true, due to the non-orthogonality of the expansions representing each centre. In fact in regions where the positronium formation cross section is small scattering of positrons by hydrogen can still be described quite accurately by a single-centre expansion (no positronium channels included), however, convergence is found to be slow requiring targets of angular momentum as high as $l = 15$ [39]; the higher angular momentum targets are required in order to describe important virtual positronium formation. We will return to this point later.

[8]It should be noted that the exchange kernels $K_{\alpha\gamma}(x, \rho)$ and $\overline{K}_{\gamma\alpha}(\rho, x)$ are Hermitian conjugates of each other. In practice, in the least-squares method which we shall meet later, they are calculated separately; the reason for this is due to the

different discretisations used when converting to numerical form.

[9]As will be shown in §2.4 the first of these boundary conditions is strictly imposed on the scattering wavefunction by a particular choice of the basis functions in which the wavefunction is expanded.

[10]Consider the set of relations

$$\sum_\alpha k_i^\alpha f_i^\alpha(r_B) = 0.$$

Since we have $\det \delta_{i\alpha} = 1$, the only set of solutions is the trivial solution $k_i^\alpha = 0$ $\forall i, \alpha$, thus our solution is linearly independent [138].

[11] We make clear at this point the meaning of the word 'exchange', which can cause confusion. In the case of positron scattering the meaning of the term differs from electron scattering in which exchange refers to the symmetry imposed by the Pauli principle. Hereinafter, exchange is used to refer to the effects surrounding the rearrangement of the particles and the formation of positronium.

[12]Terminology adopted from the R-matrix method in which a similar expansion of the wavefunction is made in some region outside which the exchange potentials are negligible.

[13]The reader may question this statement and ask why, for example, a set of orthogonalised associated Laguerre polynomials of the form

$$\phi_{il}(r) \sim (\lambda r)^{l+1} \exp(-\lambda r/2) L_{i-1}^{2l+2}(\lambda r)$$

cannot be employed (λ is a scaling parameter to be chosen). There are possibly three reasons: (1) a set of these functions $\{\phi_{il}(r); i = 1, \ldots, I\}$ will not well represent the asymptotic form of the wavefunction; (2) it would be silly to expand the wavefunction over a large region of space and not make use of well established R-matrix propagation techniques, since this will give rise to a considerably large calculation; and (3) experience of functions of this type before [2] has shown them to be difficult to use since the results depend sensitively on the choice of the scaling parameter, λ, which hence needs to be chosen carefully.

[14]For very large scale numerical calculations a linearly dependent basis was found to give rise to severe ill-conditioning of the resulting linear equations, as shown by an analysis of the effect on the condition number (see chapter 3).

[15]Incidentally, it is found that this very simple generalisation alone can give quite a marked improvement in the performance of the algorithm where the weights are chosen by consideration of the strength of the potential.

[16]A separate weight applied to the boundary condition (last term in equation 2.52) was also experimented with for a while; it was, however, found that with a good choice of program parameters not to be necessary and was subsequently set to one.

[17]It should be noted that the elastic cross section for scattering by an overall Coulomb force as defined here is not the actual cross section which is infinite.

[18]The factor $[1-(-)^\lambda]$ arises because of the charge/mass symmetry of the positronium, discussed in appendix C.

[19]Hermiticity may be shown by consideration of the equation

$$\int d\boldsymbol{x} \; \left(\psi_1^*(H\psi_2) - (H\psi_1)^*\psi_2 \right) \; ,$$

where the integration is over the inner region, and application of Green's theorem.

[20]For an in-depth account of the use of variational methods in electron scattering theory see, for example, Bransden [97]. For positron scattering, see the work of Humberston *et al* [22–25, 71–75], Kuang and Gien [26, 27] or Shimamura [129] or the review by Armour and Humberston [20].

[21]See, for example, Bransden and Joachain [139, 140].

Chapter 3

The Close Coupling Program

Having discussed the basic methods of scattering theory and derived the close coupling equations in the least-squares and minimum-norm formalisms we now turn to the implementation. We discuss in this section the evaluation of the potentials and the other most important numerical considerations.

More details of the code, including sample input and output and some of the more technical details, are given in appendix A. The parallelisation is discussed in appendix B.

3.1 Basis Functions and Construction of the Targets

The radial scattering wavefunctions were expanded using functions based on shifted Legendre functions. These were of the form

$$\phi^i_\lambda(r) = \frac{\sqrt{2\lambda - 1}}{r_0} P_{\lambda-1}(x)(1 - e^{-\mu r})^{L_i+1} \tag{3.1}$$

where the scale factor

$$x = \frac{2r}{r_0} - 1, \tag{3.2}$$

μ is a constant and r_0 is the outer radius for the solution; the factor

$$(1 - e^{-\mu r})^{L_i+1} \tag{3.3}$$

is to ensure the boundary condition at the origin (2.41a) is satisfied. For most values of L_i the choice of the constant μ was found to not be critical and the basis functions performed well over a range $0.2 \lesssim \mu \lesssim 2$, proof that the factor (3.3) had negligible impact on the completeness of the set. However, for larger values of the channel angular momentum L_i, typically $L_i \gtrsim 7$, it was found that this term extended too far along r having a detrimental impact on completeness evident in the solution error. It was found, for values of the total angular momentum J up to 20, that $\mu = 2.0$ was sufficient;[1] a further increase in μ might be necessary for even higher J.

A number of other basis functions were also investigated: ones based on Laguerre functions and others based on Slater functions were tried; the addition of a few oscillatory functions was also tried. Although the Laguerre and Slater basis sets multiplied by the appropriate weight functions in theory also form complete sets (with the correct choice of parameters), they were found to be less convenient to use; the arbitrary parameters depended sensitively on energy whereas this was found not to be the case with the shifted Legendre functions. The addition of a small number of (maybe 4) oscillatory functions to each channel was investigated with the view that they may help represent the wavefunction at larger distances. These were based on Ricatti-Bessel functions when there was no long range Coulomb interaction and Coulomb functions when both particles were charged. For smaller calculations of only 10 or so channels this was found to significantly improve accuracy, however, for larger calculations the effects were disastrous, the linear dependence of the sets resulting in intractable condition numbers in the matrix equation (2.50). In fact, the overall recurring theme when choosing parameters was usually seeking a relatively low condition number; a poor choice of parameters was generally evident by a very rapid increase in the conditioning by many orders of magnitude.

The target wavefunctions were constructed from sets of Laguerre functions by diagonalising the targets' internal Hamiltonians. These were of the form

$$R_{n_\alpha l_\alpha}(r) = e^{-\zeta r/2} r^{l_\alpha} \sum_{k=1}^{K_l} c_k^{(n_\alpha l_\alpha)} \zeta^{3/2} \left[\frac{(k-1)!}{(2l_\alpha + k + 1)!} \right]^{1/2} L_{k-1}^{2l_\alpha + 2}(\zeta r), \qquad (3.4)$$

Table 3.1: Most common target basis sets used. Other basis sets may be derived from these.

2-state	He$^+$(1s)	Ps(1s)
6-state	He$^+$(1s,2s,2p)	Ps(1s,2s,2p)
9-state	He$^+$(1s,2s,2p,3s,3p,3d)	Ps(1s,2s,2p)
20-state	He$^+$(1s-3s,2p-$\overline{8p}$, 3d-$\overline{8d}$, $\overline{4f}$ − $\overline{6f}$)	Ps(1s)
29-state	He$^+$(1s-$\overline{8s}$, 2p-$\overline{8p}$, 3d-$\overline{8d}$, $\overline{4f}$ − $\overline{8f}$)	Ps(1s,2s,2p)

where the $c_k^{(n_\alpha l_\alpha)}$ are expansion coefficients determined by the diagonalisation. The scaling parameter, ζ, was chosen such that the diagonalisation would exactly reproduce the ground state. Thus for He$^+$, $\zeta = 4.0$; for Ps, $\zeta = 1.0$. The number of functions used, K_l, varied with angular momentum. Typically, for the direct partition targets, e.g. He$^+$, 7–10 were used for each l. This, relatively large, number of functions in fact reproduced the first three states (1s, 2s, 2p) to a very good accuracy and also reproduced the 3s, 3p, 3d states quite well. They were, for all intents and purposes, essentially eigenstates. For the exchange partition (Ps) the wavefunctions were constructed in the same manner from large numbers of functions. Once again, the number of functions was sufficient to produce what were essentially eigenstates for the 1s, 2s and 2p levels.

Slater functions were also used to construct targets. In these cases the parameters were chosen in order to exactly reproduce the wavefunctions. Sets of this kind were used in some smaller calculations where only a few low-energy eigenstates were required, e.g. He$^+$(1s,2s,2p,3s,3p,3d). The Slater set Ps(1s,2s,2p) was also used in place of the set constructed by use of diagonalised sets of Laguerre functions; however, no detectable difference was observed, justifying the interpretation of the lower levels as eigenstates and thus also the interpretation of cross sections for the strictly $\overline{2s}$ and $\overline{2p}$ channels as pure 2s and 2p cross sections (a bar over the top of a channel indicates that it corresponds to a pseudostate rather than eigenstate.) Some of the most frequently used sets are given in table 3.1 (discussed in chapter 4). The energies for a typical set of Laguerre targets are shown in table 3.2.

Table 3.2: Target energies for a pseudostate basis constructed from sets of 10, 9, 8 and 7 Laguerre functions (following the work of Kernoghan *et al* [30]) for the s, p, d and f states respectively and scaling parameters of $\zeta = 4.0$. The nucleus is that of He, i.e. $Z = 2$. The $n = 9$ and $n = 10$ states were not employed since the energies were considered too high to have a significant effect (see also the discussion in chapter 4). For convenience, the energies have been tabulated in both a.u. and eV.

	a.u.				eV			
	s	p	d	f	s	p	d	f
1	−2.000000				−54.42			
2	−0.499996	−0.499998			−13.61	−13.61		
3	−0.211297	−0.214566	−0.219142		−5.75	−5.84	−5.96	
4	0.025408	−0.002484	−0.045821	−0.090835	0.69	−0.07	−1.25	−2.47
5	0.457980	0.374436	0.257022	0.136763	12.46	10.19	6.99	3.72
6	1.246540	1.041224	0.792274	0.557416	33.92	28.33	21.56	15.17
7	2.777892	2.272870	1.754082	1.307755	75.59	61.85	47.73	35.59
8	6.221826	4.826050	3.642805	2.729471	169.31	131.32	99.13	74.27
9	16.484876	11.402345	8.066285	5.844799	448.58	310.28	219.50	159.05
10	75.496769	38.400123	23.085828	15.181295	2054.39	1044.93	628.20	413.11

3.2 Evaluation of the Direct Potentials and Asymptotic Potential Coefficients

Beginning with the direct potential for the direct partition, i.e. $V_{\alpha\beta}(x)$. Referring to equation (C.71) and noting that $C_0 = 1$, the $\lambda = 0$ term of the summation (shortening the $R_{n_\alpha l_\alpha}(r)$ notation to R_α)

$$-2C_0 \int_0^\infty r^2 \mathrm{d}r \gamma_0(r,x) R_\alpha R_\beta$$

$$= -2 \int_0^\infty r^2 \mathrm{d}r \frac{1}{r_>} R_\alpha R_\beta$$

$$= -\frac{2}{x} \int_0^x r^2 \mathrm{d}r R_\alpha R_\beta + 2 \int_x^\infty r^2 \mathrm{d}r \frac{1}{r} R_\alpha R_\beta, \qquad (3.5)$$

where $r_>$ refers to the greater of x and r. Now, for $\alpha = \beta$ this becomes

$$-\frac{2}{x}\delta_{\alpha\beta} + 2\delta_{\alpha\beta}\int_x^\infty [R_\alpha]^2 \left(\frac{r^2}{x} - r\right) dr; \tag{3.6}$$

the $\delta_{\alpha\beta}(2/x)$ cancels with that of equation (C.71) giving

$$V_{\alpha\beta}(x) = 2\delta_{\alpha\beta}\int_x^\infty [R_\alpha]^2 \left[\frac{r^2}{x} - r\right] dr$$

$$- 2\left((1 - \delta_{\alpha\beta}) + \sum_{l=1}^{N_l}\right) C_\lambda \left\{\int_0^x R_\alpha R_\beta \frac{r^{l+2}}{x^{l+1}} dr + \int_x^\infty R_\alpha R_\beta \frac{x^l}{r^{l-1}} dr\right\}. \tag{3.7}$$

In practice the integrals were evaluated from the upper to lower limits for additional numerical stability and those involving an infinite limit were truncated. The quadrature was performed by interpolating the least-squares/minimum-norm mesh with 6 point Gauss rules. Comparisons of the 6 point rules performed with 8 point interpolation found the potentials to be calculated with sufficient accuracy. Sufficient accuracy of the 6 point rules was verified by comparison with 8 point rules.

The direct potentials in the exchange partition (C.75) were evaluated in a similar way by interpolating 6 point Gauss rules between the mesh points. The upper limit was truncated and the quadrature split into two components evaluated separately with the final nodes closest to the cusp point at $\rho = R/2$. Comparisons with 8 point rules differed by less than 4×10^{-5}.

The asymptotic potential coefficients were evaluated in a similar manner using compound Gauss rules. The accuracy was verified by comparing results generated with coefficients calculated using higher order rules.

3.3 Structure and Evaluation of the Exchange Kernels and Potentials

The kernels $K_{\alpha\gamma}^{(1)}(x,\rho)$, ... were decomposed by the following relations

$$K_{\alpha\gamma}^{(1)}(x,\rho) = \sum_{\lambda=0}^{\Lambda} A_{ac\lambda} k_{\lambda,\alpha\gamma}^{(1)}(x,\rho) \qquad \overline{K}_{\alpha\gamma}^{(1)}(\rho,x) = \sum_{\lambda=0}^{\Lambda} \overline{A}_{ac\lambda} \overline{k}_{\lambda,\gamma\alpha}^{(1)}(\rho,x) \tag{3.8a}$$

$$K_{\alpha\gamma}^{(2)}(x,\rho) = \sum_{\lambda=0}^{\Lambda} A_{ac\lambda} k_{\lambda,\alpha\gamma}^{(2)}(x,\rho) \qquad \overline{K}_{\alpha\gamma}^{(2)}(\rho,x) = \sum_{\lambda=0}^{\Lambda} \overline{A}_{ac\lambda} \overline{k}_{\lambda,\gamma\alpha}^{(2)}(\rho,x) \tag{3.8b}$$

where the angular factors $A_{ac\lambda}$ and $\overline{A}_{ac\lambda}$ and the $k^{(1)}_{\lambda,\alpha\gamma}(x,\rho)$, ... are derived in appendix C. The integrable singularity at $\mu = -1$ in the angular quadrature was handled by a change of variable and the integration was performed by a Gauss-Legendre rule. For most situations a 32 point rule was found to be sufficient, although near a resonance where the exchange coupling was large a 36 point rule was sometimes found to be necessary. $\Lambda = 20$ was found to give adequate convergence.

Once the scattering solutions have been solved for the exchange potentials may be constructed by straightforward radial integration. In the construction of the least-squares equations a similar integration is performed, this time with the wavefunction replaced by the individual basis functions used in the expansion.

In practice quite a lot of care had to be employed in the radial quadrature. To see why, we take a short diversion to investigate some of the properties of the kernels.

Consider first real (eigen) states only. With $i = 1$ equations (C.16) and (C.47) reduce to

$$k^{(1)}_{\lambda,\alpha\gamma} = \int_{-1}^{+1} \mathrm{d}\mu \frac{P_\lambda(\mu)}{r^{l_\alpha} R^{l_\gamma}} R_\alpha(r) \left[\frac{Z}{x} - \frac{Z}{r}\right] S_\gamma(R) \tag{3.9a}$$

and

$$\overline{k}^{(1)}_{\lambda,\gamma\alpha} = \int_{-1}^{+1} \mathrm{d}\mu \frac{P_\lambda(\mu)}{r^{l_\alpha} R^{l_\gamma}} S_\gamma(R) \left[\frac{Z}{x} - \frac{1}{R}\right] R_\alpha(r) \tag{3.9b}$$

where μ is the cosine of the angle between $\boldsymbol{x}$ and $\boldsymbol{\rho}$. Since real states are of the form

$$R_\alpha(r) \sim r^{l_\alpha} e^{-\zeta r/2} \times \text{polynomial} \tag{3.10}$$

(and similarly for $S_\gamma(R)$ states) we see that the kernels $k^{(1)}_{\lambda,\alpha\gamma}$ and $\overline{k}^{(1)}_{\lambda,\gamma\alpha}$ possess singular integrands along the lines $x = 2\rho$ and $x = \rho$ respectively. Considering now any state in general, i.e. pseudostates too, we have since

$$\frac{\mathrm{d}^2}{\mathrm{d}r^2}[rR_{n_\alpha l_\alpha}(r)] = \frac{l_\alpha(l_\alpha + 1)}{r^2} R_{n_\alpha l_\alpha}(r) + \text{higher order terms} \tag{3.11}$$

singularities arising from the matrix elements

$$I_\lambda(x,\rho) = \int_{-1}^{+1} \mathrm{d}\mu \frac{P_\lambda(\mu)}{r^{l_\alpha} R^{l_\gamma}} R_\alpha(r) \left[\frac{Z}{r} + \frac{1}{R}\right] S_\gamma(R) \tag{3.12}$$

which, once again, are along the lines $x = 2\rho$ and $x = \rho$.

Take the integral

$$I_n(x, \rho) = \int_{-1}^{+1} d\mu P_n(\mu) \frac{e^{-\alpha|x-\rho|}}{|x-\rho|} e^{-\beta|x-2\rho|}. \tag{3.13}$$

Defining

$$J_n(x, \rho) \equiv e^{-\alpha|x-\rho|} e^{-\beta|x-2\rho|}, \tag{3.14}$$

along the line $x = \rho$ we have

$$J_n(x = \rho) = e^{-\alpha x \sqrt{2}(1-\mu)^{1/2}} e^{-\beta x (5-4\mu)^{1/2}} \tag{3.15}$$

$$< e^{-\beta x} \tag{3.16}$$

and so

$$I_n < \int_{-1}^{+1} d\mu P_n(\mu) \frac{e^{-\beta x}}{\sqrt{2}x(1-\mu)^{1/2}} \tag{3.17}$$

which is true even if $P_n(\mu)$ changes sign since the contribution from $0 \leqslant \mu \leqslant 1$ is greater than that from $-1 \leqslant \mu < 0$. Using the fact that

$$\int_{-1}^{+1} (1-x)^{-1/2} P_n(x) dx = \frac{2^{-3/2}}{2n+1} \tag{3.18}$$

([141] equation 7.225(3) p.822)

$$I_n(x = \rho) < \frac{2}{2n+1} \frac{e^{-\beta x}}{x}. \tag{3.19}$$

Similarly, along the line $x = 2\rho$ we find

$$I_n(x = 2\rho) < \frac{2}{2n+1} \frac{e^{-\alpha\rho}}{\rho}. \tag{3.20}$$

Replacing the term $|x - \rho|^{-1}$ with $|x - 2\rho|^{-1}$ we find similar behaviour in the range. Close to the line $x = \rho$ the behaviour of the kernels will be dictated largely by the exponent α, i.e. the range of the $S_\gamma(R)$ wavefunctions. Similarly, close to the line $x = 2\rho$ it will be controlled by the $R_\alpha(r)$ wavefunctions.

To summarise, we see that the extent of the kernels $k^{(1)}$ and $\overline{k}^{(1)}$ is governed by the range of the targets: along the line $x = 2\rho$ it is dictated by the range of the $S_\gamma(R)$ targets (positronium) with extent either side of the line controlled by the

Figure 3.1: The exchange kernels $K_{\alpha\gamma}^{(i)}(x,\rho)$ $i = 1,2$ upper and lower plots respectively; α is a $He^+(6p)$ state and γ is a $Ps(2p)$ state; the total angular momentum is $J = 0$. The sharply peaked structure along the line $x = 2\rho$ is clearly evident. All units are in a.u.
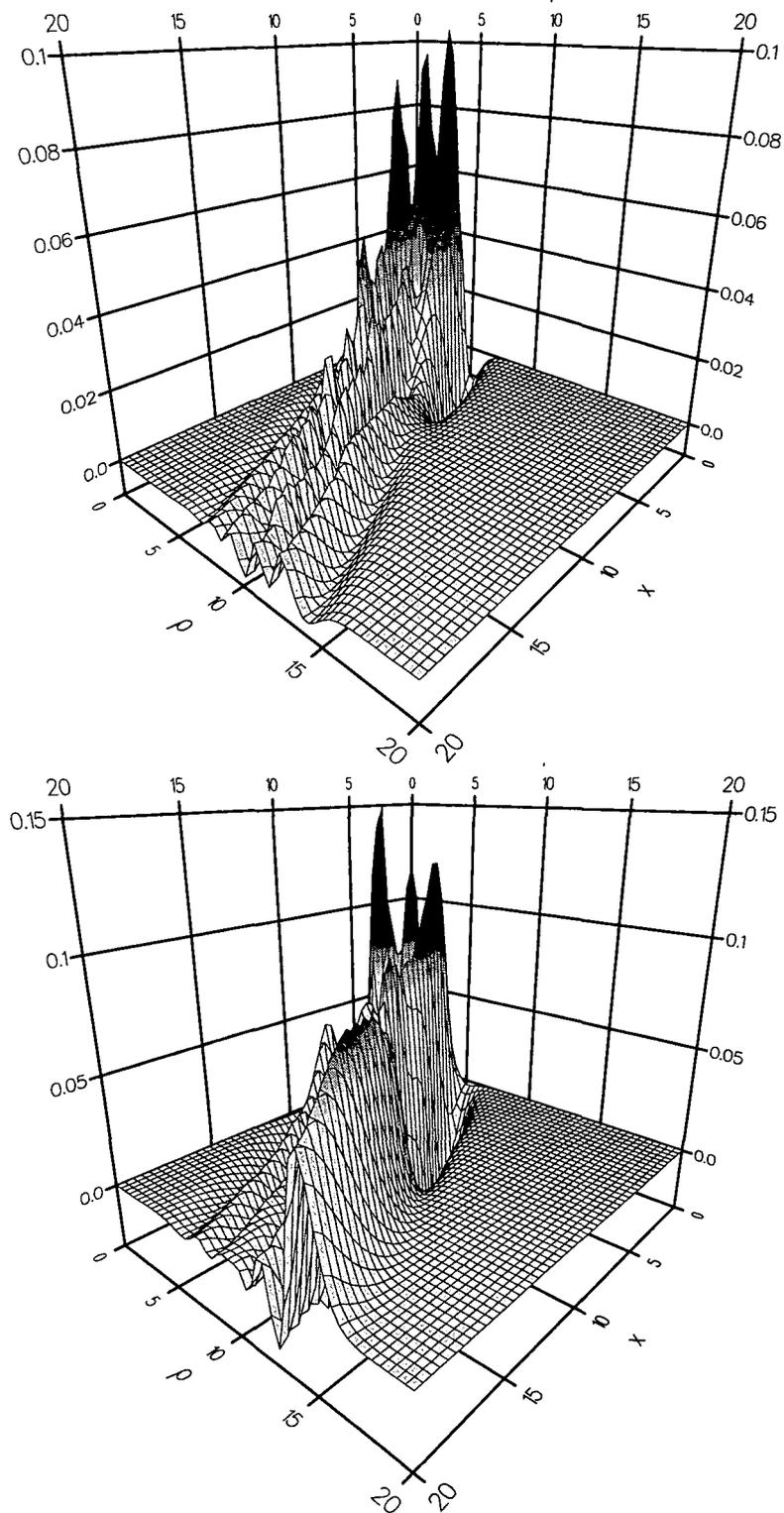
$R_\alpha(r)$ (direct partition) targets; and conversely the extent along the line $x = \rho$ is that of the $R_\alpha(r)$ with the width of the $S_\gamma(R)$. The behaviour of the kernels $k^{(2)}$ and $\overline{k}^{(2)}$ is somewhat simpler: there is no singular behaviour in the integrands and the range from the origin is simply that of the target wavefunctions; we also expect them to be relatively smooth.

Due to the singularities in the integrand, although integrable, we expect quite sharp peaks in the kernels along the lines $x = \rho$ and $x = 2\rho$ with relatively little contributions elsewhere, except close to the origin. Typical kernels have been plotted in figure 3.1. We can now see why some care is necessary employing a numerical quadrature for the exchange potentials. If the singular behaviour were along lines $x = $ constant or $\rho = $ constant we may have been able to factor some of it out with a carefully chosen Gaussian quadrature. However, in our case a separate quadrature would have to be calculated for each value of x or ρ as well as basis functions. An analysis of the computational effort alone (not to mention reprogramming) showed this approach to be very inefficient. Instead, we might expect that a division of the range up into many subranges with low order Gaussian rules or Simpson's rule with variable step size across the range would work well (it should be pointed out that high order rules are not suitable to apply to integrands of this nature since polynomial expansions are not suitable for fitting sharply peaked functions.) In practice both were found to perform equally well.

Since the kernels altogether dominate the storage requirements of most calculations and errors in the quadrature often dominate the calculation overall (especially close to a resonance) a great deal of effort is required to choose the appropriate combination of quadratures. The only easy way is by trial and error, although a simple prescription is easy to employ. It was found that performing a relatively small calculation employing a small number of states on each centre (a few lower eigenstates and some high-lying pseudostates) and calculating the solution error at each point on the wavefunction by back-substitution any inadequacy of the radial quadrature was easy to spot. By noting that the integrand is sharply peaked along the lines $x = \rho$ and $x = 2\rho$ one could readily correct the problem. After only a few iterations a suitable set of points was generated which was found to perform well

Figure 3.2: Kernel memory saving scheme illustrated for the exchange (Ps) partition kernels.
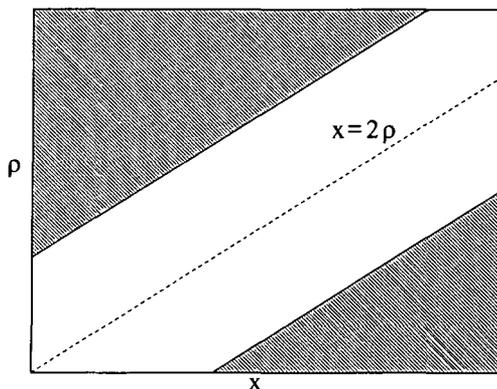
across the entire energy range studied. Using this method it was relatively easy to determine whether or not a high solution error was due to the exchange quadrature or something else and the program parameters could be readily systematically improved.

Furthermore, it was found empirically that when performing the radial quadrature with the basis functions there was sometimes a drastic loss of significant figures due to subtractions. A study in which the positive and negative contributions were summed separately and compared just before the final summation found that as many as 6 significant figures were sometimes lost. Although the code for this was significantly slower due to the frequent comparison-branch instructions this was found to have a very noticable effect on the results. For this reason the separate summation was retained permanently.

Since much of the time spent evaluating the exchange kernels is involved in construction of the target wavefunctions at many values of r and ρ, it was found that a Chebyshev interpolation procedure was more efficient than direct evaluation of the targets every time; 48 point rules were used. The last coefficients, which are a measure of the accuracy of the interpolation, were less than around 10^{-9} in the direct partition and 10^{-13} in the exchange.

A further small reduction in the storage requirements was obtained by noting that many of the elements of the kernels, if we take a square area $x < x_{\max}$ $\rho < \rho_{\max}$, are negligible; these need not be calculated or stored. Since when the Ps($n = 2$) states are included it is the positronium that is of longest range, the

range to be covered by x and ρ is governed by the extent along the line $x = 2\rho$. In the direct partition grid points outside the range $(x - \Delta\rho)/2 < \rho < (x + \Delta\rho)/2$ were discarded and similarly in the exchange partition those outside the range $2\rho - \Delta x/2 < x < 2\rho + \Delta x/2$ (illustrated in figure 3.2). Based on the discovery that up to about 6 significant figures were sometimes lost Δx and $\Delta\rho$ were chosen so that only regions of the kernels that had dropped to below about 10^{-6} were excluded. The results were found to be insensitive to the choice of Δx and $\Delta\rho$ and a significant saving in storage was made.

Kernel elements were automatically zeroed if either of the target internal coordinates, r or R, exceeded a cut-off point at which the target wavefunction had dropped to a small fraction of the maximum. This fraction was chosen to be 10^{-7}.

3.4 Choice of the Inner Region and Propagation

The choice of the inner region in calculations involving the $\mathrm{Ps}(n = 2)$ states was governed by the extent of the exchange kernels. For most calculations the inner region in the direct partition was chosen to be $0 < x < 40$ and that of the exchange partition $0 < \rho < 30$; the R-matrix was then calculated at points $x \approx 38$ and $\rho \approx 28.5$ from which it was then propagated to $x = \rho = 200$ and the solution matched to Coulomb functions [142]. The scattering K-matrices were then determined by matching the propagated solutions to Coulomb (or Riccati-Bessel) functions at a radius of 200 a.u. Propagation to larger distances was found to be unnecessary.

3.5 Choice of Fitting Meshs

We now turn our attention to the choice of points r_q in the functional (2.45). Since the minimum-norm formalism was found to be superior to the least-squares in all but the smallest of calculations we limit our discussion to the former only.

Clearly the total number of points will depend on the number of basis functions which will in turn depend on energy, the number of functions increasing as the

Table 3.3: Example grids used in least-squares calculations. These ones are suitable for up to 250 eV.

direct partition	0.005		7.0		16.0		28.0		40.0
order of rule		56		56		56		56	
exchange partition	0.005		6.0		12.0		21.0		30.0
order of rule		56		56		56		56	

square root of the collision energy. A compound rule composed of rules of order between about 50 and 70 were found to work best. Due to the fact that the order of the error term increases with the order of the rule and hence the smoothness of the integrand, rules of order much higher than 70 were avoided. Rules composed of a larger number of lower order rules were found to give poor results. The reason for this is unclear, however it is conjectured that these rules suffer from a lack of continuity of the solution derivatives across the boundaries.

Examples of grids used are displayed in table 3.3.

3.6 Run-Time Checks

A number of run-time checks were performed during the calculations in order to verify the stability and accuracy. These included:

1. construction of the scattering wave functions for all channels and solutions and verification that they did indeed satisfy the scattering equations;

2. checks for the accuracy with which the boundary conditions were obeyed;

3. checks for convergence of the solution expansion coefficients;

4. checks of the symmetry of the initial and final R-matrices and the K-matrix; and

5. calculation of the exchange potentials at the matching point.

The normalised solution errors (the absolute error divided by the maximum value of the solution) were mostly found to be below about 5×10^{-4} for the most significant solutions, though usually much better, and below an absolute value of around 10^{-4} otherwise. The boundary conditions were obeyed to typically much better than 5×10^{-5} and convergence of the solution expansion coefficients was generally to within 10^{-5} of the largest coefficient, but often better. For the largest (~ 60 channel) calculations the accuracy of the linear solver was around 10^{-9}, obtained by back-substitution of the solution vectors, and the symmetry of the R- and K-matrices was always satisfactory. The exchange potentials at the edge of the inner region were generally found to be less than 10^{-4} of their peak value in the most significant solutions and always less than around 10^{-4} in absolute magnitude, although again almost always much better than this, justification of the choice of the inner region.

More details of the code, including sample output, are given in appendix A.

3.7   Conditioning

The linear equations arising from the least-squares and minimum-norm methods are known to be inherently poorly conditioned. Since for a converged calculation the number of channels can be as high as 60 and the number of simultaneous equations as high as 5000, the factors leading to this are a major concern. In order to investigate this a Singular Value Decomposition (SVD) method was used to obtain the solution, from which an estimate of the condition number could be made. Once the conditions leading to ill-conditioning had been identified, however, it was found that a robust LU-decomposition method [104] gave better results with a drastic reduction in computing resources.

The most significant factors leading to ill-conditioning were: (a) the position of the boundary condition; and (b) the number of scattering basis functions used. We discuss these in turn.

For problems where all channels were open, the positioning of the boundary condition was not a concern. For calculations involving closed channels high in

the continuum (pseudostates), however, it was found that the boundary condition should be placed close (less than ~ 1 a.u.) from the outer edge of the solution region. Closed channel solutions were found to have excessively large coefficients if the boundary condition was far in due to the rapid exponential increase in the asymptotic region; this resulted in overly large condition numbers.

The basis functions employed in the expansion of the scattering wavefunction contributed significantly to ill-conditioning if the set contained linear dependence with a rapid increase in the condition number as redundant basis functions were added. Although a small number of oscillatory basis functions are beneficial in the smaller (9-state) calculations, the use of these was found to increase the degree of ill-conditioning in the larger cases and did not improve the convergence. For this reason they were not used in these cases. The number of channels was found to have a negligible affect on the conditioning of the problem, with the issues mentioned above being a much stronger constraint on the size of target basis which could be tackled using this method.

There would thus be no fundamental problem, as far as I am aware, with increasing the number of channels further using this method.

Notes

[1] For targets up to f-states a total angular momentum of $J = 20$ leads to a maximum scattering angular momentum of $L_i \leqslant 23$.

Chapter 4

Close Coupling Results

In this chapter we present the results of this work [143]. The reactions e^+-H and e^+-He$^+$ were considered, though, due to the extensive amount of studies that have been made on the former collision system, the emphasis was mainly on the latter. Collisions on the helium ion were considered over a wide range of energies, from low-energy elastic scattering below the first threshold up to around 250 eV, well above the ionisation threshold.

Much of the work of previous authors has been referenced in previous chapters and discussed where appropriate and so only work of relevance to the discussion is mentioned here.

4.1   Hydrogen

Positron-hydrogen scattering has been investigated by a great many other authors and so was largely just used here as a test of the accuracy of the minimum-norm method. The results of Bransden and Noble [2] using the least-squares method were verified, which in turn were found to agree well with the results of Mitroy and Stelbovics (see Bransden and Noble). The minimum-norm results were found to be identical, indicating the quality of the choice of parameters in both works.

A number of resonances have been found in the e^+-H system. The first was found by Higgins and Burke [31] who discovered a resonance in the coupled-static approximation for s-wave scattering at an energy of 2.62 Ryd and width 0.31 Ryd.[1]

63

Table 4.1: Threshold energies for positrons scattered by He$^+$(1s). Units in eV.

	Excitation	Positronium Formation	
He$^+$(n=2)	40.772		
		Ps(1s)	47.612
He$^+$(n=3)	48.373		
He$^+$(n=4)	51.019		
He$^+$(n=5)	52.246		
		Ps(n=2)	52.719
He$^+$(n=6)	52.911		
		Ps(n=3)	53.667
Ionisation	54.423		54.423

The existence of this resonance has since been confirmed and numerous other resonances discovered; see [28] and references cited therein. A number of resonances have been tabulated by Mitroy and Stelbovics [48]. A few of these resonances have been studied using the minimum-norm method as part of this work in order to test the ability of the method to resolve narrow resonance structure. Shown in figure 4.1 is a particular narrow resonance, of width $\sim 10^{-4}$ Ryd, which clearly demonstrates the ability of the minimum-norm method to resolve such fine structure. A number of other resonances were also verified.

Large 33-state close coupling calculations with pseudostates [30] have been shown to agree very well with experiment up to 100 eV [21] endorsing the use of the method.

4.2 He$^+$

Although a significant amount of work has been done on positron collisions with neutral targets, work on positron collisions with ionic targets so far has been somewhat limited. In the case of ionic targets the Born series is of less value than for

Figure 4.1: e$^+$-H resonance produced using the minimum-norm method. The calculations shown are for $J = 2$. Calculations using two basis sets are shown: (1) the right-hand resonance (solid curves) is that of a CC(3,3) calculation using a Slater target set; (2) the left-hand resonance (dashed curves) was produced using the same model but with a Laguerre target set. The discrepancy between the two is due to the non-exactness of the Laguerre targets, although on the energy scale shown, this is obviously a very small difference. The down-arrow indicates the position of the resonance as predicted by Mitroy and Stelbovics [48] of width 1.73×10^{-4} Ryd ($\Delta k \sim 10^{-4}$ a.u.); the right arrow indicates that the Ps(1s) cross section is to be read from the right-hand axis, all other cross sections to be read from the left-hand axis.
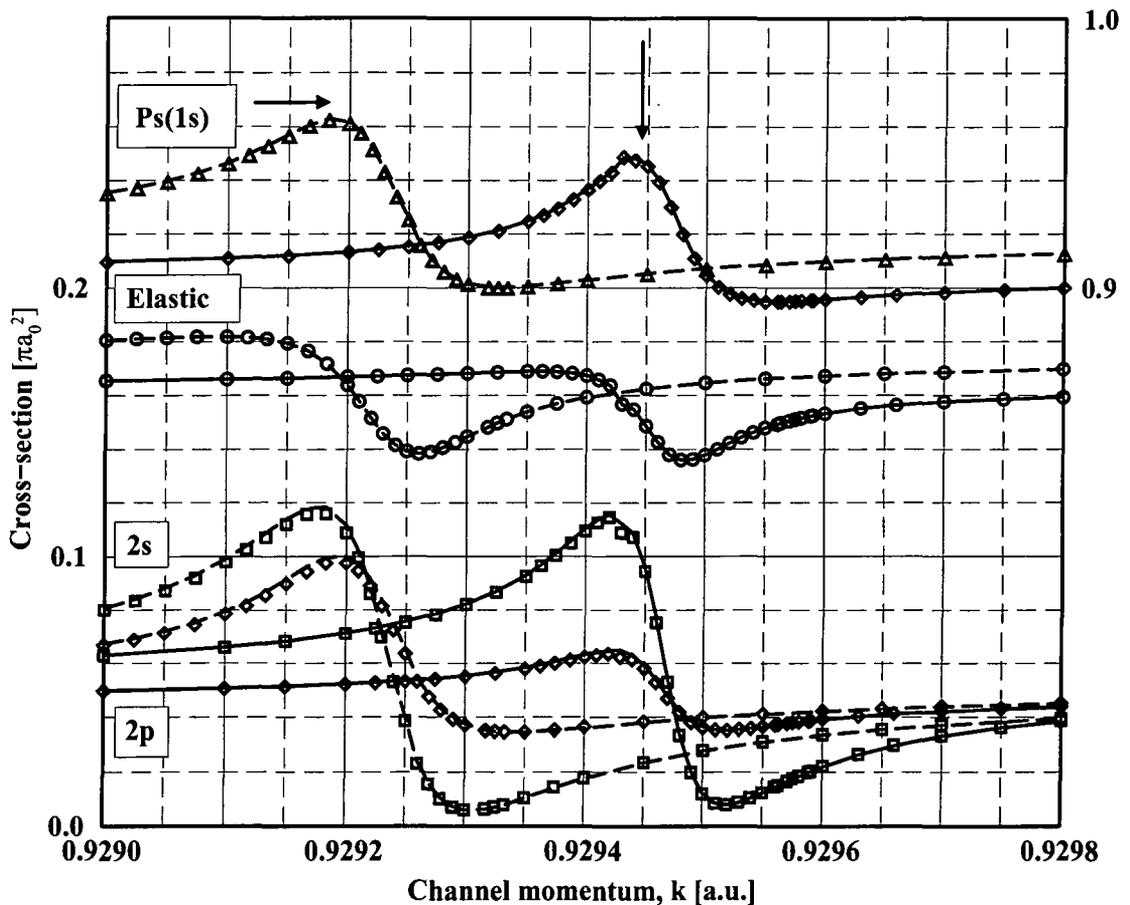
neutral targets, except at very high energies, due to a divergent term that appears in the second-order expansion; first order Born calculations for e^+-He^+ scattering have, however, been reported by Fojón *et al* [144–146] for energies from 250 eV upwards. Also, results for positronium formation in the ground state using an optical potential model have been reported by Gianturco and Melissa [83]. Other work on e^+-He^+ scattering has been restricted to smaller basis sets (Khan, Mazumder and Ghosh [137], Abdel-Raouf [147]) or lower partial waves (Shimamura [129], Igarashi and Shimamura [37].

Numerous calculations have been performed in this work using the minimum-norm and least-squares methods with a variety of basis sets and over a wide range of energies. The most common basis sets employed are defined in table 3.1 (p. 51). Also, for convenience, the threshold energies are displayed in table 4.1. It was decided to only include pseudostates on the ionic centre since experience of converged calculations for positron-hydrogen scattering by Kernoghan *et al* [30] using a 33-state model consisting of 30 states on the hydrogen showed the extra states on the positronium to be unnecessary when compared to an 18-state model with pseudostates equally distributed on both centres. Moreover, the 33-state results were found to suffer much less from pseudoresonance structure than the 18-state results omitting the need for artificially smoothing.

Here, we discuss firstly results obtained using real (eigen) state targets alone. We then make the extension to larger calculations employing both real states and pseudostates discussing, in turn, scattering in two major energy intervals: low energy, below about 47.6 eV, in which only a limited number of channels are open; and high energy, above 60 eV, in which both positronium production and ionisation are energetically feasible.

2-, 6- and 9-State

Previous studies of the e^+-He^+ system have been limited. Bransden and Noble [2] were first to apply the least-squares method using 2-, 6- and 9-state models. The optical potential approach has been used by Gianturco and Melissa for a variety of systems [81–83] including H and He^+; the agreement between the optical potential

and least-squares methods, however, was poor. It has been a subject of the work in this part of this thesis to extend the least-squares method of Bransden and Noble to include pseudostates in the hope of resolving this discrepancy. Also of interest was the problem of trying to resolve the disagreement in other calculations over whether resonances existed at certain collision energies in the e^+-He^+ system. Resonances have been reported by Ho [148], Bhatia and Drachman [149] and Igarashi and Shimamura [37]; these will be discussed further later on. As a test of the minimum-norm-with-pseudostates method all results obtained by Bransden and Noble were reproduced and found to be identical.

Low Energy (Below 47.6 eV)

We consider now the energy region below the positronium formation threshold in which only a limited number of processes are energetically possible. Within this region there is just one threshold: that of $n = 2$ excitation. These regions have previously been studied by several authors [37, 129, 137, 147–149]. Those results are compared with those obtained using the minimum-norm approach and the question is addressed as to whether resonances occur in the region immediately below the positronium formation threshold.

Each of the two regions are addressed in turn.

0–40 eV

We begin by discussing the lower region in which only elastic scattering is possible. This region is particularly interesting because of the bounds which exist on the phase shift. The region has previously been studied a number of other workers [129, 137, 147], but, as far as I know, only for s, p and d-wave scattering.

Harris model variational calculations have been carried out for s-wave e^+-He^+ collisions by Shimamura [129] at scattering energies between 6.62 eV and 37.53 eV using 56 trial functions. The calculated phase shift is found to increase to a maximum at around 12–14 eV, becoming increasingly repulsive as the energy approaches the $n = 2$ threshold. These results are displayed in figure 4.2a as the dot-dash line, as are results by Khan *et al* [137] (dashed line) obtained using the Callaway variant

Figure 4.2: Elastic scattering phase shifts for e$^+$ scattering by He$^+$ below the inelastic threshold (40.772 eV): O 27-state minimum-norm; □ Khan *et al* [137]; ◇ Shimamura [129]. (a) $J = 0$; (b) ——— $J = 1$; – – – $J = 2$.
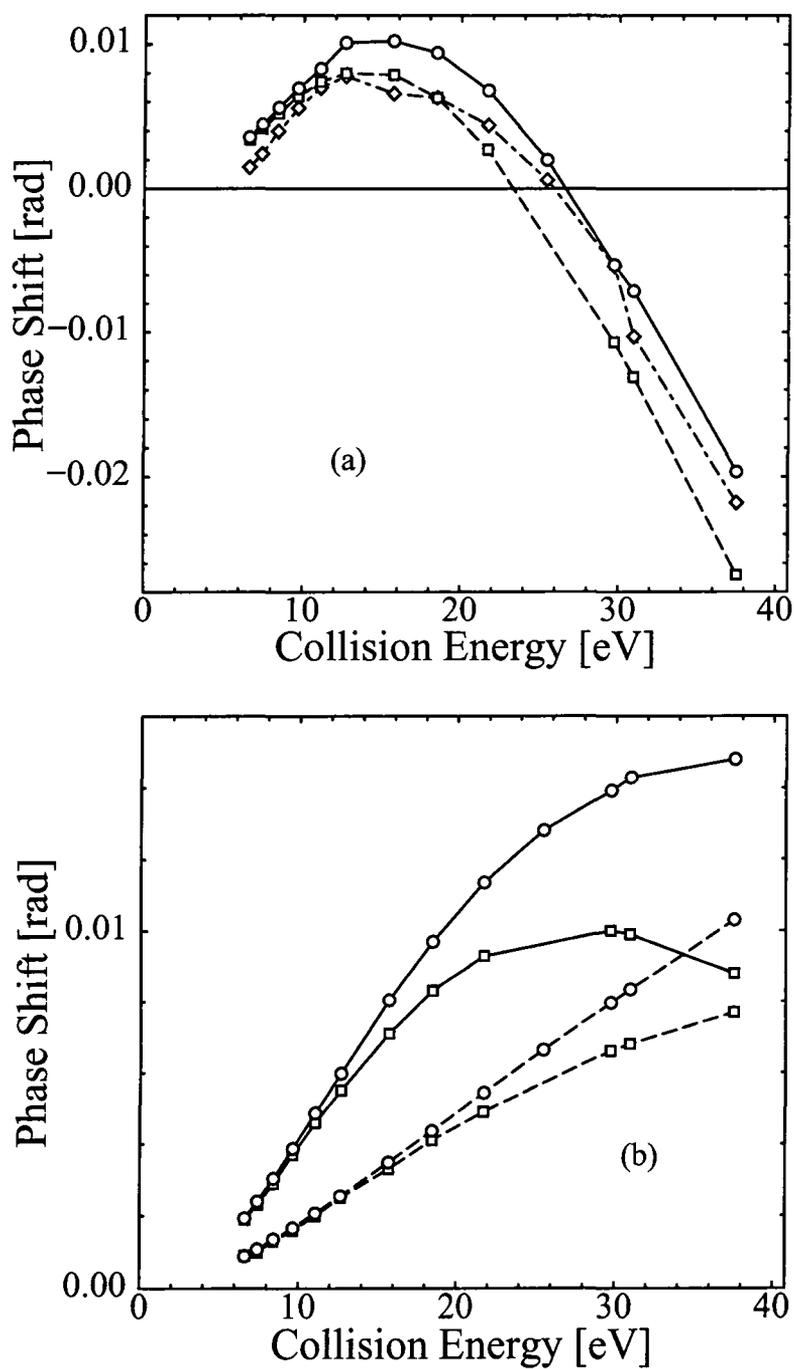
of the polarised orbital model. Minimum-norm results are shown by the solid line; these were calculated using a 27-state model which corresponds to the 29-state model less the Ps($n = 2$) states. There is good overall agreement between the three calculations. The phase shift obtained with the minimum-norm approach is, however, 23% higher than the Harris model results at 12.65 eV and 11% higher at 37.53 eV. The minimum-norm results are found to lie above the variational and polarised orbital results at all energies. Given that the results reflect a lower bound on the phase shift we expect the minimum-norm calculation to be a better approximation.

In figure 4.2b minimum-norm eigenphases are compared with polarised orbital results for p- and d-wave elastic scattering. At higher energies the polarised orbital phases begin to drop significantly below the minimum-norm results while the minimum-norm results continue to rise as the threshold is approached, evidence for the greater completeness of the 27-state close coupling. In fact it is known that the omission of the Ps formation channels, as in the Callaway polarised orbital method, can sometimes lead to a potential which is more repulsive than it should be. Shown in figures 4.3 and 4.4 are cross sections for $J = 0$ and phase shifts for $J = 1$ respectively using different models. In figure 4.3 convergence of the elastic scattering cross section for a scattering energy of $E = 34.8$ eV with and without the inclusion of the Ps(1s) state is depicted whilst in figure 4.4 phase shifts for a number of models have been computed across the energy range. It can be seen that the single Ps state is indeed necessary and cannot be accounted for by inclusion of the n=9 states on the direct centre. A complete set of numerical values for these phase shifts is provided in table 4.2 (p. 71).

To summarise then. In the low energy region there is substantial agreement between the minimum-norm 27-state model and the Harris variational results and polarised orbital results. This serves as a good test of both the minimum-norm code and of the close coupling model. At the lowest energies the agreement is very close indeed; however, at the higher energies there is indication that the 27-state model is in fact more complete and that the inclusion of states on the positronium centre contributes significantly to the overall completeness of the close coupling

Figure 4.3: Convergence of the $J = 0$ elastic scattering cross section for e^+-He^+ at an energy of $E = 34.8$ eV. The results of the solid curve have allowed for exchange by including the Ps(1s) channel while the dashed results exclude the coupling. The eigenstates and pseudostates used were the same as those generated for the 27-state basis (table 3.2).
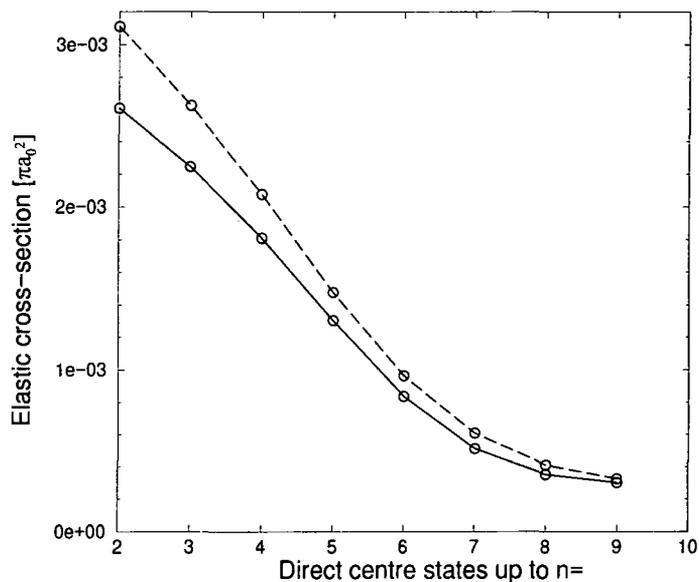

Figure 4.4: Comparison of $J = 1$ phase shifts for different models for e^+-He^+ below the inelastic threshold (40.772 eV): □ Khan, Mazumder and Ghosh [137]; △ 27-state without coupling; ◊ 27-state without coupling but with n=9 states added; ○ full 27-state.
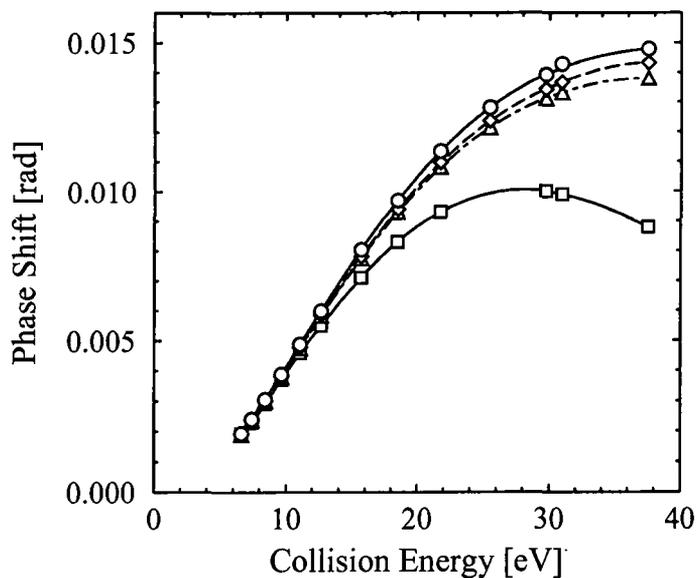
Table 4.2: Elastic scattering phase shifts for e$^+$ scattering by He$^+$ below the inelastic threshold (40.772 eV). Phase shifts are shown for total angular momenta (J) of 0, 1 and 2.

| Energy (eV)	Phase Shift (rad)						
	$J = 0$			$J = 1$		$J = 2$	
	present	*Khan*[a]	*Shim.*[b]	*present*	*Khan*[a]	*present*	*Khan*[a]
6.62	0.356(-2)	0.34(-2)	0.15(-2)	0.192(-2)	0.19(-2)	0.893(-3)	0.90(-3)
7.41	0.446(-2)	0.42(-2)	0.24(-2)	0.239(-2)	0.23(-2)	0.108(-2)	0.10(-2)
8.43	0.560(-2)	0.52(-2)	0.40(-2)	0.304(-2)	0.29(-2)	0.134(-2)	0.13(-2)
9.65	0.695(-2)	0.64(-2)	0.56(-2)	0.387(-2)	0.37(-2)	0.167(-2)	0.16(-2)
11.07	0.829(-2)	0.74(-2)	0.70(-2)	0.487(-2)	0.46(-2)	0.207(-2)	0.20(-2)
12.65	1.008(-2)	0.80(-2)	0.78(-2)	0.598(-2)	0.55(-2)	0.254(-2)	0.25(-2)
15.70	1.022(-2)	0.79(-2)	0.66(-2)	0.804(-2)	0.71(-2)	0.349(-2)	0.33(-2)
18.45	0.942(-2)	0.63(-2)	0.63(-2)	0.970(-2)	0.83(-2)	0.437(-2)	0.41(-2)
21.71	0.680(-2)	0.27(-2)	0.44(-2)	1.135(-2)	0.93(-2)	0.543(-2)	0.49(-2)
25.47	0.201(-2)	-	0.06(-2)	1.281(-2)	-	0.664(-2)	-
29.73	−0.532(-2)	−1.07(-2)	−0.54(-2)	1.392(-2)	1.00(-2)	0.796(-2)	0.66(-2)
30.94	−0.710(-2)	−1.31(-2)	−1.03(-2)	1.428(-2)	0.99(-2)	0.833(-2)	0.68(-2)
37.53	−1.965(-2)	−2.68(-2)	−2.18(-2)	1.480(-2)	0.88(-2)	1.030(-2)	0.77(-2)

[a] Kahn, Muzumder and Ghosh [137]
[b] Shimamura [129]

expansion even at these relatively low energies.

40–47.6 eV

The region between the $n = 2$ excitation threshold at 40.8 eV and the capture threshold at 47.6 eV is of special interest because of reported s- and p-wave resonances [37, 148, 149]. Although low-lying resonances are well established in the case of e$^+$-H collisions the dominance of the Coulomb repulsion between the positron and the helium ion suggests that similar resonances in the e$^+$-He$^+$ system should not be expected. Nonetheless, stabilisation calculations carried out by Bhatia and Drachman [149] indicated the possibility of a resonance at an energy of 44.5 eV and of a second s-wave resonance above the capture threshold. These results were

Figure 4.5: e⁺-He⁺ scattering below the capture threshold. Upper graph: cross sections (—— elastic scattering; — — — 2s excitation; — · — 2p excitation). Lower graph: eigenphase shifts versus collision energy (eigenphase sum given by the solid line).
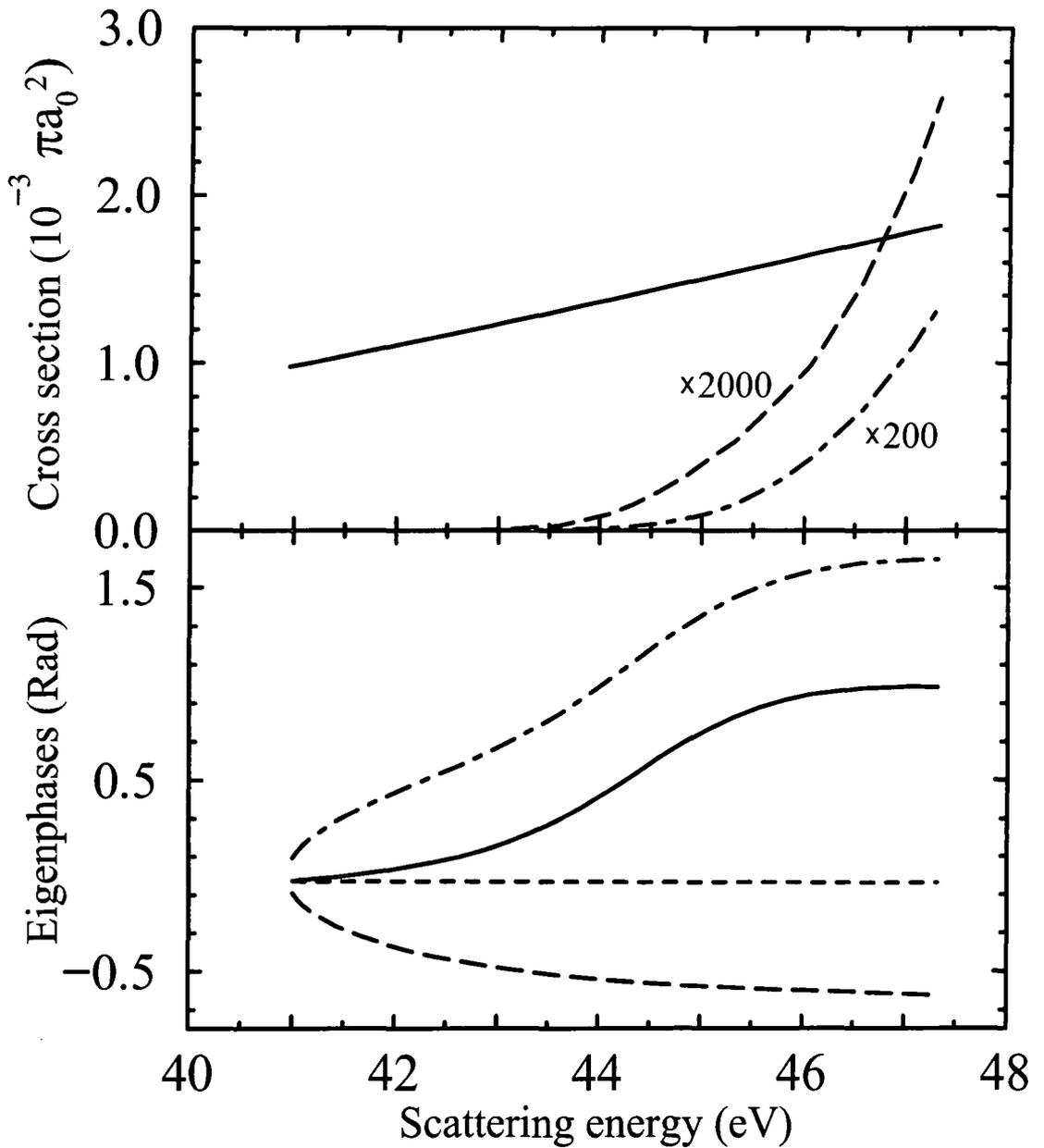
subsequently confirmed by Ho [148] using a complex-coordinate rotation method. The lower energy resonance was located at 44.491 eV and found to have a width of 3.52 eV. No conclusive evidence was discovered for the mechanism causing the formation of the resonance but it was suggested that it might arise as a result of attractive polarisation forces. More recent hyperspherical close-coupling calculations by Igarashi and Shimamura [37] discount the existence of any very broad resonances but detect very narrow Feshbach resonances just below the capture threshold.

Cross sections and eigenphases calculated with the minimum-norm method using the 29-state model are displayed in figure 4.5. Two of the eigenphases are repulsive and vary slowly with the scattering energy; the third eigenphase is attractive and increases monotonically between the two thresholds. The eigenphase sum is indicated by the solid line. Although there is some indication of an increased slope around 44 eV the results show no sign of a broad resonance at 44.5 eV. The cross sections are also seen to be smooth over the entire energy range. A 9-state calculation over the same energy region also showed no sign of any resonance and a similar calculation for p-wave scattering concluded the same thing. In the minimum-norm approach it is not feasible to search for the very narrow (width 2.1×10^{-4} eV) resonance found by Igarashi and Shimamura [37] since it is difficult to obtain accurate results very close to thresholds.[2]

The elastic scattering results at 47.25 eV are found to be approximately a factor of 2 lower than the corresponding results of Igarashi and Shimamura at 47.62 eV. Similarly, the $n = 2$ excitation cross section, which is very small, is about a factor of 5 smaller than the hyperspherical value. Convergence as a function of basis set excluding the Ps(1s) state was studied for a scattering momentum of $k = 1.82$, corresponding to $E = 45.1$ eV. The results indicated that the 29-state calculation is well converged.

Intermediate Energy (60–250 eV)

We now discuss the energy region above the ionisation threshold. As discussed above this has been studied previously by Gianturco and Melissa [81–83] using an optical potential approach and Bransden and Noble [2] using the least-squares

approach with eigenstate expansions on each centre only. The two approachs were found to disagree considerably and it is our primary interest here to investigate the effect of the addition of pseudostates to the smaller close coupling models with a view to re-evaluating the discrepancy.

The largest basis set employed was the 29-state. It was found empirically, however, that the $n = 2$ states on the Ps centre could in fact be dropped for values of the total angular momentum between $J = 7$ and $J = 12$ since, in these cases, coupling to these channels is negligible. Furthermore it was found that for $J > 12$ the coupling between the partitions could be entirely omitted with no effect on the results. The pseudostate set used in the calculation includes a representation of the $He^+(n=3)$ states sufficiently accurate for them to be interpreted as eigenstates. Numerical values of the 29-state model cross sections are provided in table 4.3.

A comparison was made between the 29-state basis and a number of other bases for $J = 1$ up to around 300 eV. $J = 1$ was chosen since (1) the number of channels is relatively small and so it was possible to make comparisons with larger basis sets using the available computing resources (not possible with higher J); and (2) all of the major cross sections are significant, unlike $J = 0$ where only elastic scattering is large enough to reliably deduce differences between the bases. It was found that with the 29-state basis it was necessary to include the $n = 2$ positronium states up to at least 200 eV for two reasons: (1) to minimise the pseudoresonance structure in the region ~ 100–150 eV; and (2) for convergence in the elastic cross section. The elastic cross section was found to be around 7% higher in the 27-state model (29-state less the Ps($n = 2$) states) at 175 eV. Other bases were generated by diagonalising different numbers of Laguerre functions to generate up to $n = 8$ and $n = 9$ states. Including all of the generated states we denote these bases n8 and n9 respectively. Interestingly it was found that the elastic and 2s and 2p excitation cross sections were not sensitive to the inclusion of the Ps($n = 2$) states with the n8 model; the n8 basis discussed here thus only includes the ground state on the positronium centre. Below around 250 eV the three bases were found to differ very little; however, above 250 eV the elastic cross sections were found to diverge between the bases. At 250 eV the elastic cross section was around 3–4% lower in the

	Energy [eV]								
	60	75	100	125	150	175	200	225	250
Elastic	6.55(-3)	8.38(-3)	1.04(-2)	1.16(-2)	1.26(-2)	1.31(-2)	1.35(-2)	1.35(-2)	1.35(-2)
2s	5.93(-3)	8.88(-3)	9.79(-3)	9.43(-3)	8.76(-3)	7.85(-3)	7.03(-3)	6.36(-3)	5.78(-3)
2p	2.58(-2)	5.27(-2)	7.08(-2)	7.23(-2)	7.19(-2)	6.95(-2)	6.65(-2)	6.36(-2)	6.07(-2)
3s	8.60(-4)	2.46(-3)	2.89(-3)	2.50(-3)	2.31(-3)	2.08(-3)	1.86(-3)	1.68(-3)	1.52(-3)
3p	1.42(-3)	7.55(-3)	1.34(-2)	1.47(-2)	1.49(-2)	1.44(-2)	1.38(-2)	1.32(-2)	1.26(-2)
3d	3.73(-4)	1.26(-3)	1.74(-3)	1.66(-3)	1.58(-3)	1.45(-3)	1.31(-3)	1.17(-3)	1.06(-3)
n=2 excitation	3.18(-2)	6.16(-2)	8.05(-2)	8.17(-2)	8.07(-2)	7.73(-2)	7.35(-2)	6.99(-2)	6.65(-2)
n=3 excitation	2.66(-3)	1.13(-2)	1.80(-2)	1.89(-2)	1.88(-2)	1.79(-2)	1.70(-2)	1.61(-2)	1.52(-2)
Total excitation	3.48(-2)	7.88(-2)	1.15(-1)	1.20(-1)	1.18(-1)	1.13(-1)	1.07(-1)	1.02(-1)	9.69(-2)
Ps(1s)	5.51(-3)	1.14(-2)	1.44(-2)	1.26(-2)	1.01(-2)	7.24(-3)	4.58(-3)	3.23(-3)	2.30(-3)
Ps(2s)	2.40(-4)	9.19(-4)	1.04(-3)	2.55(-3)	1.33(-3)	1.07(-3)	1.19(-3)	6.40(-4)	3.83(-4)
Ps(2p)	3.02(-4)	8.43(-4)	1.87(-3)	1.43(-3)	5.94(-4)	2.51(-4)	2.82(-4)	1.71(-4)	5.12(-5)
Ps(n⩽2)	6.05(-3)	1.32(-2)	1.74(-2)	1.66(-2)	1.20(-2)	8.55(-3)	6.06(-3)	4.05(-3)	2.74(-3)
Ps(n⩾3)	3.34(-4)	1.09(-3)	1.79(-3)	2.46(-3)	1.18(-3)	8.13(-4)	9.08(-4)	5.00(-4)	2.68(-4)
Ps total	6.39(-3)	1.43(-2)	1.91(-2)	1.91(-2)	1.32(-2)	9.37(-3)	6.96(-3)	4.55(-3)	3.00(-3)
Ionisation	2.37(-5)	2.46(-3)	2.17(-2)	3.54(-2)	4.89(-2)	5.54(-2)	5.76(-2)	5.83(-2)	5.71(-2)
Electron loss	6.41(-3)	1.67(-2)	4.09(-2)	5.45(-2)	6.21(-2)	6.48(-2)	6.45(-2)	6.29(-2)	6.01(-2)
Total	4.77(-2)	1.04(-1)	1.66(-1)	1.86(-1)	1.93(-1)	1.91(-1)	1.85(-1)	1.78(-1)	1.70(-1)

n8 basis than the 29-state basis; the n9 basis was inbetween. It seems, then, that above around 250 eV it is necessary to include the higher energy states and that states should not be omitted from the diagonalised sets. Below 250 eV, however, the 29-state basis was found to be superior to the other bases since it supressed the pseudoresonance structure better than the other models.

The term ionisation is used here to mean the promotion of the electron into the continuum, to be contrasted with electron loss which is removal of the electron from the target nucleus, i.e. the sum of ionisation and capture. The ionisation cross section has been estimated by simply adding the contribution of each of the continuum pseudostates rather than by using the more elaborate ansatz of Kernoghan et al [29]. Total excitation has been estimated by summing over the negative energy states, eigenstates and pseudostates, in the direct partition excluding the ground state. The total cross section has been defined as the sum of the elastic, total excitation and electron loss cross sections.

Results were calculated for the first 21 partial waves up to a maximum of $J = 20$, with corrections for the omitted higher J being estimated by the use of a Geometric Progression (GP) [150]. The use of a GP for estimating the contribution of higher J up to infinity is standard practice, although some authors [29, 30] choose to use the first Born approximation for excitation cross sections. Results are calculated up to a maximum value of J, J_i; it is then assumed that the partial cross sections for $J \geqslant J_{i-1}$ may be estimated by the series

$$a \left(1 + \frac{1}{r} + \frac{1}{r^2} + \frac{1}{r^3} \cdots \right) \tag{4.1}$$

where $a = \sigma_{J_{i-1}}$ and $r = \sigma_{J_i} / \sigma_{J_{i-1}}$; the correction due to the omitted J is then given by

$$\Delta\sigma = \frac{\sigma_{J_{i-1}}}{1 - \sigma_{J_i}/\sigma_{J_{i-1}}} - \sigma_{J_i} - \sigma_{J_{i-1}}. \tag{4.2}$$

The basis for this assumption is that the partial cross sections decrease exponentially with J which can be justified by a semiclassical treatment of the collision process for large values of the impact parameter [150]. Clearly the partial cross sections must be falling smoothly as a function of J, having passed the peak value,

for the GP to be accurate; the correction should also be small to give reliable results. A simple test of how reliable the correction is may be made by extrapolating the partial cross sections from two different values of J_i and comparing; this was done in generating the results of this section.

The corrections applied to the 29-state model were typically very small: less than 0.02% at all energies for the elastic cross section; less than 0.06% for 2s excitation; no more than 0.2% for ionisation; and less than 1% for ground-state capture. The corrections were found to increase with the collision energy for most cross sections, 2p capture being the notable exception peaking at around 14% at 175 eV. Of the excitation cross sections, corrections to the 2p excitation were the largest, ranging from less than 0.01% at the lowest energy to a little over 4% at the highest, 250 eV. The largest percentage corrections to all cross sections were to the 2s capture. These were up to 40% at the highest energy; however, in terms of absolute magnitude this equates to less than 5% of the ground-state capture cross section and less than 4% of the total capture. The largest corrections in terms of absolute magnitude were, by a large margin, those of the 2p excitation. The corrections to the total cross section may thus be deduced to be less than 2%.

Selected minimum-norm cross sections obtained using the 29-state model are displayed in figure 4.6 as a function of collision energy. The total He$^+$ excitation cross section, indicated by the diamond points, is seen to reach a broad maximum of around 0.12 πa_0^2 at a collision energy of around 110–140 eV. The major contribution to the excitation cross section arises from excitation to the $n = 2$ states, the latter reaching a broad maximum of just over 0.08 πa_0^2 in the energy region 100–150 eV before decreasing smoothly to a value of 0.066 πa_0^2 at the highest energy, 250 eV. Also shown are ionisation (stars) and electron loss (crosses). The ionisation cross section rises gradually to a maximum value of 0.058 πa_0^2 at 225 eV; similarly, the electron loss cross section rises to a broad maximum, centred at around 180 eV, before falling slowly and converging with ionisation.

Finally in figure 4.6 the total positronium formation cross section is shown by the triangular points. A break-down of the individual contributions is shown in figure 4.7. The maximum is around 0.02 πa_0^2 and occurs at about 115 eV. The

Figure 4.6: Converged cross sections for e⁺-He⁺ scattering above the capture threshold: ♦ total excitation; ■ $n = 2$ excitation; ▲ total Ps formation; * ionisation; × electron loss.
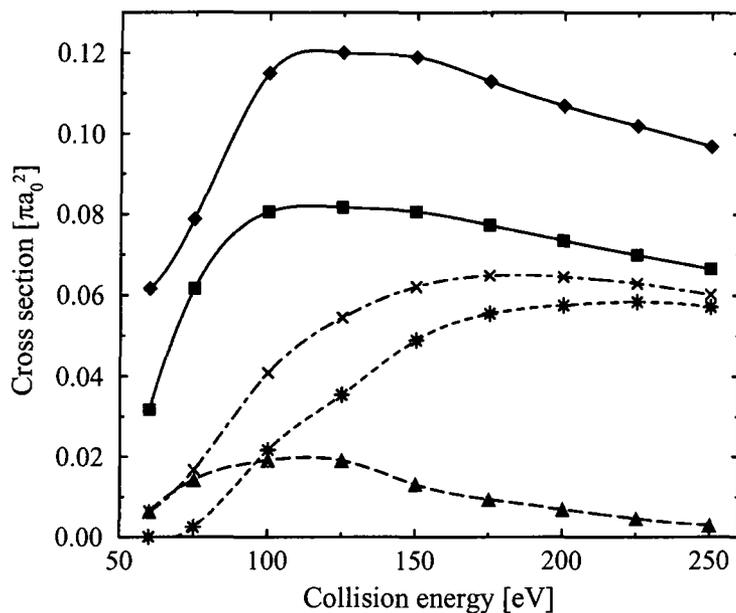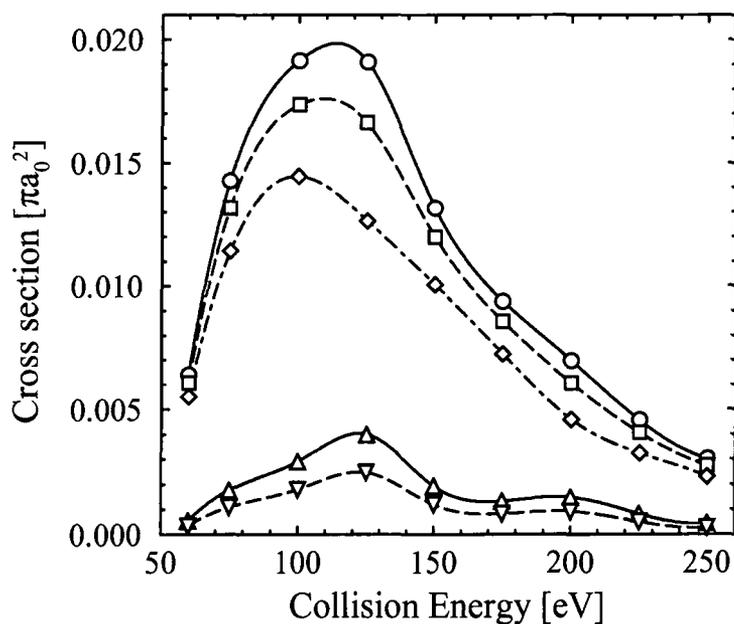

Figure 4.7: Total positronium formation cross section and the major contributions: ○ total Ps formation; □ Ps(n⩽2); ◇ Ps(1s) only; △ Ps($n = 2$); ▽ Ps(n⩾3).

dominant contribution to the cross section is ground-state capture. The maximum contribution of the $n = 2$ capture to the total is 0.004 πa_0^2 at 120 eV; the contribution from Ps($n \geqslant 3$) is much smaller still, peaking at around 0.0025 πa_0^2. The contribution from target states Ps($n \geqslant 3$) was estimated from the $n = 2$ capture using a $1/n^3$ extrapolation:

$$\sigma_{\text{Ps}}(n \geqslant 3) = 8\sigma_{\text{Ps}}(n = 2) \sum_{n=3}^{\infty} \frac{1}{n^3}. \tag{4.3}$$

Shown in figure 4.8 are the partial contributions to the total ground-state capture as a function of J. Below around 100 eV the dominant contributions are from the lower J, with relatively little contribution from the higher J. Above 100 eV the convergence becomes slower, with significant contributions to the total cross section coming from the higher J. Evidence for pseudostructure can be seen in the $J = 1$, 2 and 3 cross sections above 100 eV; however, since there is a significant contribution from the higher J there is no obvious sign of structure in the total ground-state capture as shown in figure 4.7; for this reason it was not considered necessary to artificially smooth the partial cross sections as is occasionally done by other authors.

Shown in figure 4.7 and in more detail in figure 4.9 are the contributions to capture from the $n = 2$ states. Capture into the 2s state is seen to be marginally larger than 2p capture at most energies; both of these cross sections have a low energy peak, with maxima at around 125 eV and 100 eV respectively, and a smaller peak at around 200 eV. The pseudostructure here is more substantial, showing clearly in the total $n = 2$ capture cross section. This, however, was to be expected, since the same behaviour was found by Kernoghan *et al* [29, 30] in the case of e$^+$-H collisions. The result is a Ps($n = 2$) cross section which is, on average, around 0.002 πa_0^2 in magnitude, peaking strongly between 100 and 150 eV, and decaying rapidly at 250 eV. Since the $n = 2$ contribution to the total capture cross section is very small and since, as can be seen from figure 4.7, it has no clear observable effect on the smoothness of the total Ps($n \leqslant 2$) cross section, smoothing of the cross sections was again considered unnecessary. Also, due to the pseudostructure in the $n = 2$ capture, pseudostructure is also observed in the corrective factor for

Figure 4.8: Partial cross sections for capture into the ground state of positronium for total angular momentum $J = 1, 2, \ldots 9$ (the $J = 0$ partial cross section has been omitted since it is negligible).
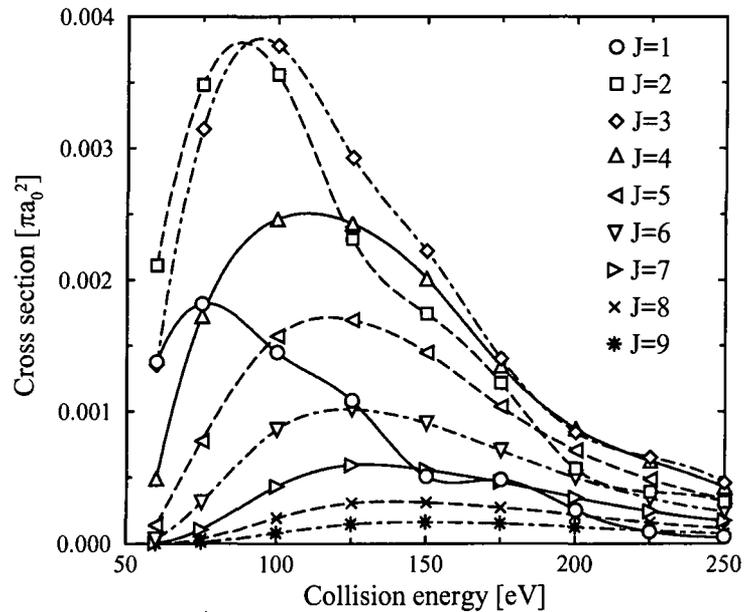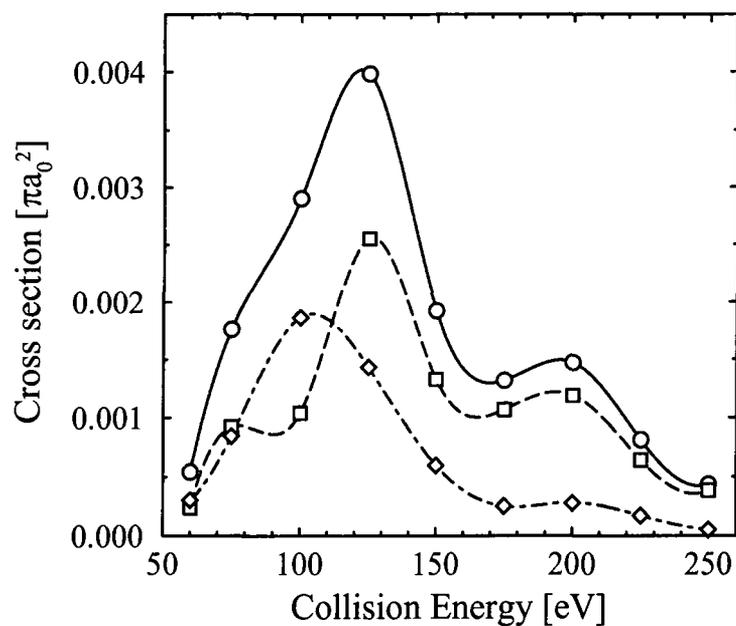

Figure 4.9: Positronium cross sections for capture into the $n = 2$ states: $\square$ 2s; $\Diamond$ 2p; $\bigcirc$ total $n = 2$ (i.e. 2s+2p).

the higher positronium states. Once again, however, this structure is too small compared to the total positronium capture cross section to require smoothing.

The extent with which the cross sections vary with the basis may be examined with reference to table 4.4. Tabulated are selected results from the 29-, 20-, 6- and 2-state bases. Also displayed in figure 4.10 (p. 83) for graphical comparison are elastic, 2s, 2p and $n = 3$ excitation, ground-state capture, ionisation and electron loss. Total cross sections from the 29- and 20-state bases are displayed in figure 4.11 (p. 84) along with total excitation and electron loss for the 29-state basis. All results were obtained using the minimum-norm approach. The 2- and 6-state results were found to be identical to those obtained previously by Bransden and Noble [2] using the least-squares approach.

It can be seen that there is good agreement between the 29- and 20-state results in most cross sections. The 2s, 2p and $n = 3$ excitation cross sections differ by less than 5% at most energies; the 2s cross section in the 20-state approximation, however, dips to almost 10% lower at 150 eV. This dip correlates with anomalous bumps in the ground-state capture, ionisation, electron loss and total cross sections within the same model that also all occur at 150 eV. Since this dip is not evident in any of the 29-state results it can be concluded then that this is merely due to pseudostructure. The 6-state approximation is seen to be quite a good approximation to the 2s and 2p cross sections at the higher energies, approaching to within 5% of the 29-state results in the 2p and 11% in the 2s. The elastic cross section at the lower energies also appears to be well converged, differing in the 29- and 20-state calculations by less than 3% below 125 eV, although above 125 eV the 20-state calculation can be seen to deviate significantly from the smooth curve of the 29-state calculation.

Ground-state capture is also in reasonably good agreement between the 29- and 20-state calculations, differing by less than 21% at all energies. The 29-state calculation is seen to be very smooth whereas the 20-state shows a little sign of structure around 100–150 eV. It should be remembered, however, when comparing capture cross sections that the 20-state model does not account for capture into excited levels of the positronium whereas the 29-state model does. Although the

Table 4.4: Cross sections (in units of πa_0^2) for positron collisions with He$^+$(1s). Comparison of results using different target basis sets.

				Energy [eV]				
	60	75	100	125	150	175	200	225
Elastic	[a] 6.55(-3)	8.38(-3)	1.04(-2)	1.16(-2)	1.26(-2)	1.31(-2)	1.35(-2)	1.35(-2)
	[b] 6.62(-3)	8.54(-3)	1.07(-2)	1.20(-2)	1.35(-2)	1.46(-2)	1.49(-2)	1.45(-2)
	[c] 8.52(-3)	1.13(-2)	1.39(-2)	1.71(-2)	1.74(-2)	1.74(-2)	1.71(-2)	1.67(-2)
	[d] 1.05(-2)	1.29(-2)	1.80(-2)	1.91(-2)	1.94(-2)	1.91(-2)	1.86(-2)	1.79(-2)
2s	[a] 5.93(-3)	8.88(-3)	9.79(-3)	9.43(-3)	8.76(-3)	7.85(-3)	7.03(-3)	6.36(-3)
	[b] 5.70(-3)	8.50(-3)	9.77(-3)	9.12(-3)	7.90(-3)	7.23(-3)	6.56(-3)	6.02(-3)
	[c] 2.31(-3)	4.47(-3)	7.07(-3)	6.76(-3)	6.63(-3)	6.33(-3)	6.00(-3)	5.65(-3)
2p	[a] 2.58(-2)	5.27(-2)	7.08(-2)	7.23(-2)	7.19(-2)	6.95(-2)	6.65(-2)	6.36(-2)
	[b] 2.60(-2)	5.08(-2)	6.82(-2)	7.24(-2)	7.13(-2)	6.86(-2)	6.57(-2)	6.27(-2)
	[c] 1.23(-2)	3.28(-2)	5.15(-2)	5.76(-2)	6.10(-2)	6.20(-2)	6.16(-2)	6.03(-2)
n=3 excitation	[a] 2.66(-3)	1.13(-2)	1.80(-2)	1.89(-2)	1.88(-2)	1.79(-2)	1.70(-2)	1.61(-2)
	[b] 2.69(-3)	1.08(-2)	1.76(-2)	1.88(-2)	1.85(-2)	1.76(-2)	1.67(-2)	1.58(-2)
Total excitation	[a] 3.48(-2)	7.88(-2)	1.15(-1)	1.20(-1)	1.18(-1)	1.13(-1)	1.07(-1)	1.02(-1)
	[b] 3.49(-2)	7.81(-2)	1.29(-1)	1.54(-1)	1.65(-1)	1.60(-1)	1.58(-1)	1.52(-1)
Ps(1s)	[a] 5.51(-3)	1.14(-2)	1.44(-2)	1.26(-2)	1.01(-2)	7.24(-3)	4.58(-3)	3.23(-3)
	[b] 5.54(-3)	1.21(-2)	1.66(-2)	1.43(-2)	1.22(-2)	8.21(-3)	5.51(-3)	3.83(-3)
	[c] 2.15(-3)	8.56(-3)	1.75(-2)	2.07(-2)	1.56(-2)	1.11(-2)	7.77(-3)	5.50(-3)
	[d] 7.14(-3)	2.75(-2)	4.22(-2)	3.49(-2)	2.47(-2)	1.69(-2)	1.15(-2)	8.01(-3)
Ps(n≤2)	[a] 6.05(-3)	1.32(-2)	1.74(-2)	1.66(-2)	1.20(-2)	8.55(-3)	6.06(-3)	4.05(-3)
Ionisation	[a] 2.37(-5)	2.46(-3)	2.17(-2)	3.54(-2)	4.89(-2)	5.54(-2)	5.76(-2)	5.83(-2)
	[b] 3.43(-7)	1.44(-3)	1.61(-2)	3.30(-2)	4.70(-2)	4.79(-2)	5.13(-2)	5.09(-2)
Electron loss	[a] 6.41(-3)	1.67(-2)	4.09(-2)	5.45(-2)	6.21(-2)	6.48(-2)	6.45(-2)	6.29(-2)
	[b] 5.56(-3)	1.35(-2)	3.27(-2)	4.73(-2)	5.91(-2)	5.61(-2)	5.68(-2)	5.47(-2)
Total	[a] 4.77(-2)	1.04(-1)	1.66(-1)	1.86(-1)	1.93(-1)	1.91(-1)	1.85(-1)	1.78(-1)
	[b] 4.71(-2)	1.00(-1)	1.73(-1)	2.13(-1)	2.37(-1)	2.31(-1)	2.29(-1)	2.21(-1)

[a] 29-state calculation
[b] 20-state calculation
[c] 6-state calculation: He$^+$(1s,2s,2p)+Ps(1s,2s,2p)
[d] 2-state calculation: He$^+$(1s)+Ps(1s)

Figure 4.10: Comparison of the 29-, 20-, 6- and 2-states bases. In figures (a)–(e): ○ 29-state; □ 20-state; ◇ 6-state; △ 2-state. In figure (f): * ionisation; × electron loss; —— 29-state; – – – 20-state.
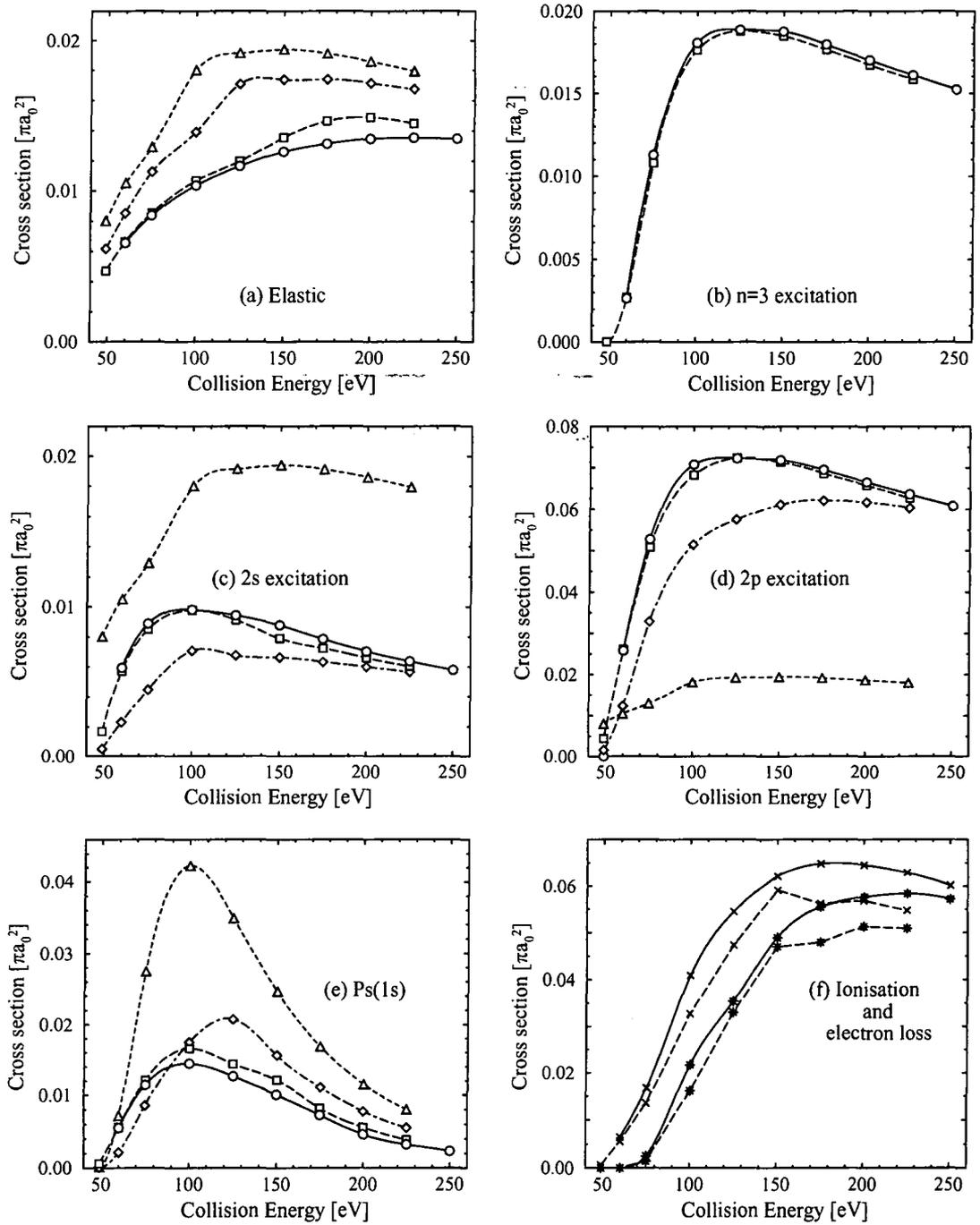
Figure 4.11: Total cross sections. ○ 29-state; □ 20-state. Total excitation ◆ and electron loss × cross sections from the 29-state basis have also been plotted for comparison.
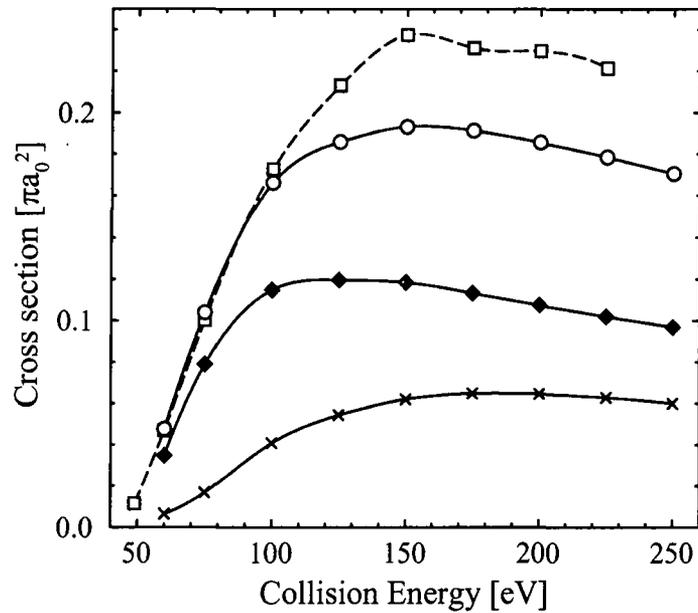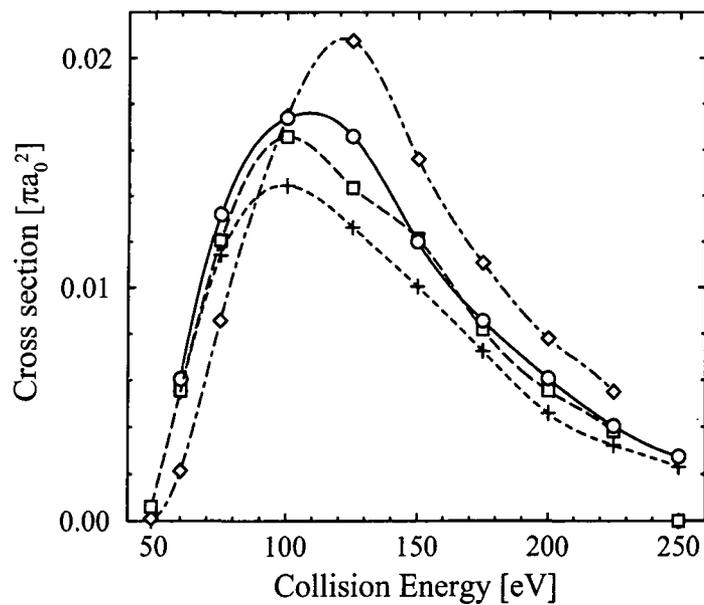

Figure 4.12: Comparison of the capture cross sections. Plotted is the $Ps(n\leqslant 2)$ cross section in the 29-state approximation ○ for comparison with the $Ps(1s)$ cross sections of the 20-state □ and 6-state ◇ approximations. The $Ps(1s)$ cross section in the 29-state approximation + is also shown.

contribution of the $n = 2$ capture is quite small when compared to capture into the ground-state, there is still enough flux going into the $n = 2$ states to significantly widen the discrepancy between the two models. It is thus more instructive to instead compare the ground-state capture of the 20-state model with the Ps($n \leqslant 2$) capture cross section of the 29-state model. This is shown in figure 4.12; numbers are also given in table 4.4 (p. 82). It can be seen that the agreement is very good, although there is a little discrepancy in the region 100–150 eV in which, as has already been pointed out, the 20-state calculation is not entirely smooth. Agreement is to within 8% at all energies excluding 125 eV.

From this data we may also assess the contribution to the cross sections of the Ps($n = 2$) states. The total $n = 2$ capture is small compared to ground-state capture at the lowest energy, 60 eV, climbing to between 20 and 30% in the central region before falling to 32%, 25% and 19% at energies of 200, 225 and 250 eV respectively. Above around 250–300 eV we may expect then that inclusion of the Ps($n = 2$) states is unnecessary.

It is interesting to note that the 6-state model offers a surprisingly good approximation for the ground-state capture cross section. This result is in contrast to the case of positron scattering by hydrogen atoms where a 6-state model provides a very poor estimate of the values obtained with large pseudostate sets [28]. The 2-state results are approximately a factor of 2 higher than those of the other calculations.

Ionisation and electron loss are not so well represented by the 20-state calculation. Referring to figure 4.10f we see that although both the 29- and 20-state results are smooth (excluding the points at 150 eV for the 20-state) the 20-state results are significantly below those of the larger basis. Recalling, however, that the 20-state basis includes only three s-states on the He$^+$ and the 29-state basis includes eight, this is not surprising. One might also expect that, for this reason, the total excitation is not well represented. Referring to table 4.4 we see that this is indeed the case; the two models agree very well at the lowest energies but differ greatly as the collision energy increases, by up to around 50% or 0.05 πa_0^2 between 125 and 225 eV. The total cross section is also not given well by the 20-

Table 4.5: Comparison of the Ps(1s) formation cross section of the 29-state model with the CBA and CDW-FS results of Fojón *et al* [144–146] and the optical potential results of Gianturco and Melissa [83]. All cross sections are in πa_0^2.

E (eV)	CBA	CDW-FS	Optical potential	Minimum-norm
250	4.8(-3)	1.8(-3)	6.9(-2)	2.30(-3)
300	-	-	2.7(-2)	-
500	9.8(-4)	5.4(-4)	-	-

state model (figure 4.11) above around 125 eV, being significantly larger than the 29-state model. The discrepancy, which is around 0.04–0.05 πa_0^2, is due largely to the discrepancy in the total excitation rather than that of ionisation and electron loss which is much smaller. Despite the large disagreement above 100 eV the 20- and 29-state results agree well, to less than 4%, at the lower energies for the total cross section and total excitation cross section.

From the discussions above we conclude that the introduction of pseudostates on both the Ps and He$^+$ centres, as done for example by Kernoghan *et al* [28, 29] in the case of positron-hydrogen scattering, is unnecessary in the cases of the transitions considered here although the effect of the introduction of a 3$\bar{p}$ state on the positronium might be interesting to investigate.

Results of Coulomb Born (CBA) and Continuum Distorted Wave Final State (CDW-FS) calculations by Fojón *et al* [144–146] and the optical potential results of Gianturco and Melissa [83] are compared with the present results in table 4.5. It can be seen from the table that the 29-state result agrees well with the CDW-FS, which, due to the inclusion of higher order distortion terms, one would expect to be better than the CBA at this energy; none, however, agree at all with the optical potential result. The optical potential result at 300 eV also appears to be significantly larger than the CBA and CDW-FS results at 250 and 500 eV. It appears likely then that the optical potential calculation is in error in some way and we conclude that the 29-state model agrees well with the distorted wave calculation.

4.3 Summary and Conclusions

Results have been presented for positron scattering by He^+ ions at energies between 6 eV and 250 eV. A complete set of converged cross sections has been given, including ionisation and positronium formation, excluding only annihilation. It has been demonstrated that the minimum-norm extension of the least-squares method has enabled the computation of results using larger basis sets with the inclusion of pseudostates. It was also demonstrated that the minimum-norm method is suitable for computing the resonant cross sections found in positron-hydrogen scattering by previous authors. It was seen that a 29-state basis, which includes states up to $\overline{8s}$, $\overline{8p}$, $\overline{8d}$ and $\overline{8f}$ on the He^+ centre and 1s, 2s and 2p on the positronium centre, gave smooth cross sections which were almost free of pseudostructure. Pseudostructure was only really evident in the excited state capture cross sections which was, compared to the ground state capture cross section, too small to be noticed in the total capture cross section. The ground state capture cross section was found to be consistent with CDW-FS results of Fójon *et al* [144–146]. Low energy elastic scattering eigenphases were also obtained which were found to be in good agreement with previous work. The eigenphases obtained above the $n = 2$ excitation threshold show no evidence for the formation of the broad s-wave resonance reported by other authors.

Notes

[1]Resonance widths may be computed using the program of Tennyson and Noble [151].

[2]The problem of approaching thresholds stems from the evaluation of the Coulomb functions for cases where $\eta = Z/k$ (Z is the residual nuclear charge and k is the channel momentum) is large, i.e. k is small. In regions where η is large the Coulomb functions can become inaccurate. This is beyond the scope of this thesis and so is not discussed here; instead see, for example, Noble [152]. The Coulomb functions here are thought to be accurate to within $|k| = 0.01$ of threshold.

PART II: CTMC and Laser-Assisted Formation of Antihydrogen

Chapter 5

Heavy Particle Capture by Hydrogen and Positronium

5.1 Introduction

The interaction of heavy particles, such as antiprotons, with simple atoms has become a subject of great importance since the development of low-energy antiproton beams [19]. The interaction of pions with liquid helium was discussed long ago by Condo [153] who postulated the mechanism by which these pions may be absorbed by the helium in states which are very long-lived compared to what one might expect.

Two isssues of current interest relate to the capture of antiprotons by atoms, namely, the spectroscopy of cold antihydrogen [17, 18, 154, 155] and the dynamics of highly excited antiprotonic atoms [156–159]. An essential aspect of these studies is the knowledge of the rate of formation of these systems and the nature of the states that are formed. Although the structure of these systems is becoming well understood [160, 161], the dynamics of formation is less well understood.

The predominant inelastic process arising from fast antiproton collisions is ionisation of the target. This process is relatively well understood at present and has been comprehensively discussed by Knudsen and Reading [162]. According to theory, below the ionisation threshold the importance of capture increases rapidly. Overviews of theoretical approaches to antiproton capture by small atoms and

molecules have been given by Cohen [163, 164] in which the role of classical modelling has been highlighted.

The Classical Trajectory Monte Carlo (CTMC) method was introduced by Abrines and Percival [165] to calculate capture and ionisation cross sections for proton-hydrogen collisions [166]. It has been applied extensively in ion-atom collision studies to predict excitation and rearrangement processes in three-body processes [167, 168]. It has been particularly successful in quantitative estimates of electron capture cross sections over a broad region of energies around the collisional ionisation threshold.

The main advantage of the CTMC method is that it is relatively simple and inexpensive to execute for three-body systems without approximation. Conversely, converged fully quantum mechanical or semi-classical simulations often require very large scale computations. For this reason there has always been an interest in constructing classical models for capture processes. Its success owes much to the characteristic nature of these processes, whereby the formation of the exotic atom involves capture of a heavy particle, such as an antiproton, into a high angular momentum Rydberg state. By the correspondence principle one expects that classical mechanics should be a good approximation in this situation, since circular or near circular hydrogenic orbits of high principle quantum number are particularly well described. Moreover, due to the high mass of the proton and antiproton, it is resonable to assume also that the nuclear motion might also be well described by a classical path. It is thus ideally suited to collisions involving matter such as muons, pions and antiprotons as it offers a fully consistent treatment of the collision process, treating all possible reactions on an equal footing. In the case of ionisation processes involving exotic particles the CTMC approach has an added advantage over quantum mechanical calculations in that continuum processes, which are vitally important in this context, are well modelled, something that is sometimes difficult in a fully quantum simulation. Indeed it has been shown in the case of μ^{-}–H collisions that the method performs remarkably well for muon capture below the ionisation threshold when compared with methods which treat the electron quantally [169, 170]. The CTMC method can be used over a wide range of energies;

the precise range of validity, however, is sometimes difficult to determine, but will exclude regions in which quantal effects such as tunnelling and interferences are important.

Several extensions to the basic method have been made in order to extend its flexibility. An extension to cover multielectron targets, given by Kirschbaum and Wilets [171], has been applied with some success [163, 172]. Extra constraints were introduced to the classical motion, suggested by an analysis of the Heisenberg uncertainty principle, without which the multielectron targets would have been unstable to autoionisation. Further developments to this theory made by Cohen *et al* [172] have turned the CTMC method into what is termed Fermi Molecular Dynamics (FMD); recent reviews include [163, 169, 173]. These have successfully treated molecular targets, such as H_2 [172], as well as atoms and ions, such as helium and neon [163, 164]. An alternative approach to many electron targets based on a frozen atomic core has been given by Peach *et al* [174] and applied to the case of collisions between atoms and ions of hydrogen and helium [175]. A method due to Olson [167] allows the state of the captured particle to be analysed in a quasi-classical way. This method is of particular interest in the study of exotic atom formation where the details of the capture orbital determine the subsequent evolution of the complex. An alternative phase-space distribution for the hydrogen target, which cannot be modelled exactly by classical mechanics, has been investigated by Cohen [176].

The capture of exotic particles by atomic hydrogen has received attention from a number of other approaches besides CTMC. The first was the Adiabatic Ionisation (AI) approach used by Wightman [177]. Since then, nonadiabatic effects have been included by more sophisticated methods: Diabatic States (DS) [178, 179]; Time-Dependent Hartree Fock (TDHF) [180]; Classical-Quantal Coupling (CQC) [170]; and the Perturbed Stationary States (PSS) model [181]. These calculations, when compared on their relative merits and restrictions, have further endorsed the use of the classical approach. Since these methods have been well discussed in a review by Cohen [182] we do not discuss them any further here.

In this chapter results of classical simulations for processes leading to the for-

Table 5.1: Examples of relatively heavy negatively charged particles suitable for the CTMC program. 1 a.u. of mass is defined as the mass of the electron, 0.511003 MeV/c^2. Data taken from [183].

Particle	Symbol	Classification	Mass		Mean lifetime
			(a.u.)	(MeV/c^2)	(seconds)
Antiproton	$\bar{p}$	Baryon	1836.15	938.28	-
Negative muon	μ^-	Lepton	206.77	105.66	2.20×10^{-6}
Negative pion	π^-	Meson	273.12	139.57	2.60×10^{-8}
Negative kaon	K^-	Meson	966.08	493.67	1.24×10^{-8}

mation of such systems are presented. In particular cross sections for antiproton capture by atomic hydrogen to form protonium, and by positronium to form antihydrogen are given. The effect of the presence of a laser on the antihydrogen formation rate is also investigated.

5.2 Theory

In what follows atomic units are used throughout unless stated otherwise.

Reactions

In the present work the Classical Trajectory Monte Carlo (CTMC) method has been used to study reactions involving antiprotons ($\bar{p}$), negative pions (π^-) and negative muons (μ^-) impacting on atomic hydrogen and also antiprotons on positronium (Ps). For example, the reactions for antiproton-atom collisions dealt with here are

$$\bar{p} + (T, e^-) \longrightarrow \begin{cases} \bar{p} + (T, e^-)_{n,l} & \text{elastic/inelastic scattering} \\ (T, \bar{p})_{n,l} + e^- & \text{antiproton capture} \\ \bar{p} + T + e^- & \text{ionisation} \end{cases} \qquad (5.1)$$
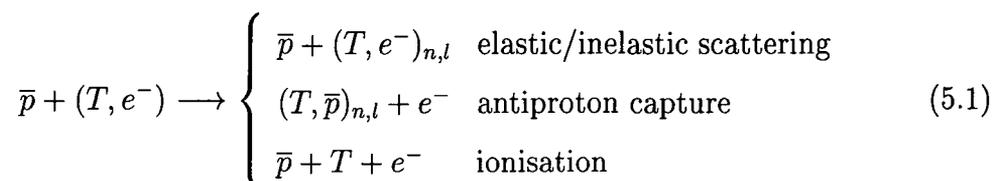
Figure 5.1: CTMC coordinates.
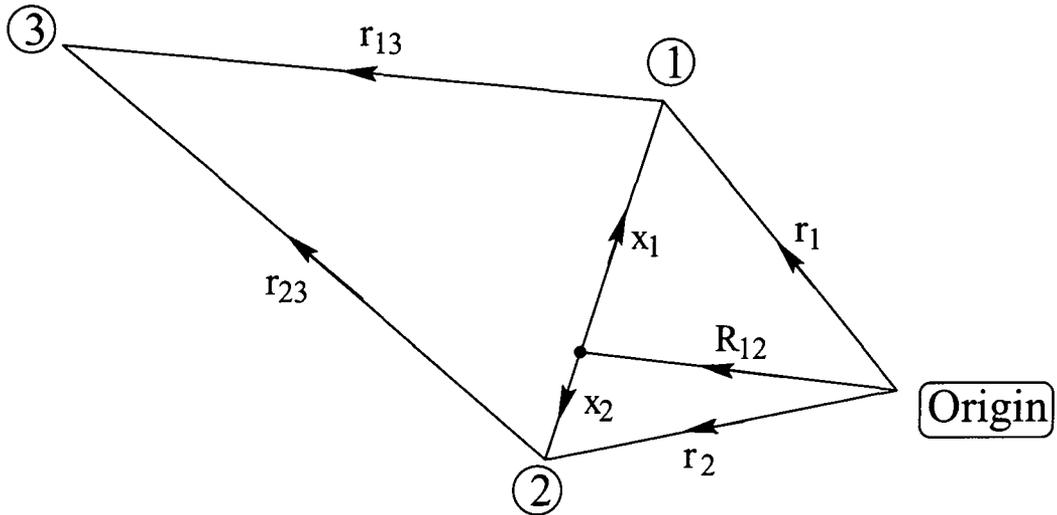
in which the target 'nucleus', T, can be either a proton or positron and the reaction can take place in the presence of external fields. The subscripts n, l represent the principle and angular momentum quantum numbers respectively. Note that, in the programming of the simulation, the code was kept general enough for the masses of all three particles to be changed, and so isotopes D and T of hydrogen could also be modelled. The antiproton may also be replaced by any other negatively charged particle. Examples of a few particles and their basic properties are given in table 5.1.

In all that follows the target atom is prepared in its ground state.

Co-ordinates and Hamiltonian

Consider the three-body problem in which the ith particle mass and coordinate are labelled as m_i and $\mathbf{r}_i$ respectively, the two-body combined mass is denoted by $m_{ij} \equiv m_i + m_j$, and the interparticle distance by $\mathbf{r}_{ij} = \mathbf{r}_j - \mathbf{r}_i$. The Jacobi coordinates, shown in figure 5.1, can then be written as

$$\mathbf{R}_{ij,k} = \mathbf{r}_k - \mathbf{R}_{ij} = \mathbf{r}_k - (m_i \mathbf{r}_i + m_j \mathbf{r}_j)/m_{ij}. \tag{5.2}$$

It follows then that the Hamiltonian is given by

$$H = \frac{p_{12}^2}{2\mu_{12}} + \frac{p_{12,3}^2}{2\mu_{12,3}} + \sum_{i<j} \frac{k_{ij}}{r_{ij}} + \frac{P^2}{2M} \tag{5.3}$$

where the masses and reduced masses are given by

$$\mu_{ij} = m_i m_j \, m_{ij}^{-1} \tag{5.4a}$$

$$\mu_{ij,k} = m_{ij} m_k \, M^{-1} \tag{5.4b}$$

$$M = m_{12} + m_3; \tag{5.4c}$$

M is the total mass. The momenta are defined as

$$\mathbf{p}_{ij} \equiv \mu_{ij} \dot{\mathbf{r}}_{ij} \tag{5.5a}$$

and

$$\mathbf{p}_{ij,k} \equiv \mu_{ij,k} \dot{\mathbf{R}}_{ij,k}. \tag{5.5b}$$

Since we are using atomic units $k_{ij} = Z_i Z_j$, where Z_i is the charge on the ith particle. The charges are chosen so that

$$Z_1 Z_2 < 0 \quad \text{and} \quad Z_2 Z_3 < 0; \tag{5.6}$$

the projectile, particle 3, may then bind with particle 2. In the centre of mass frame the term $P^2/2M = 0$. The center of mass collision energy, E, is related to the laboratory collision energy, E_{lab}, by

$$E = \frac{m_{12}}{M} E_{\text{lab}} = \frac{p_{12,3}^2}{2\mu_{12,3}} \tag{5.7}$$

and to the relative collision velocity by

$$v = \sqrt{2E/\mu_{12,3}}. \tag{5.8}$$

Monte-Carlo Procedure

The CTMC procedure is well documented [164, 165, 184] but briefly it consists of the following steps

1. Monte Carlo sampling of initial conditions $(t = 0)$;

2. integration of the equations of motion; and

3. identification of the exit channel in the asymptotic region $t \to +\infty$.

Many trajectories are performed for each collision energy until satisfactory statistics are obtained. The number of trajectories performed depends on the collision energy, the cross section required and the accuracy desired.

For a given collision energy, E, the initial conditions are specified by seven parameters: six for the target and one for the projectile. The projectile is launched towards the target from a prescribed fixed distance, d, with a variable impact parameter, b.

The initial conditions for the target are specified by six parameters. Of the six parameters, three are angles, two describing the orientation of the orbital plane, the third placing the axis of the orbit within the plane. The remaining three parameters specify the angular momentum of the orbit, which determines the shape of the paths of the particles, the initial position of the particles on these paths, and the target energy. Implicitly we assume that the perturbing ion, and/or the laser pulse, has not yet arrived so that the two-body motion is purely Keplerian.

The initial state of the target was modelled by the microcanonical distribution [185]. This prescribes the sampling of position and momentum phase space, $\rho = \rho(\boldsymbol{r}, \boldsymbol{p})$, by the constraint

$$\mathcal{K}\,\delta(E_0 - E) = \mathcal{K}\,\delta\left(E_0 - \frac{p^2}{2\mu_{12}} - \frac{k}{r}\right) \tag{5.9}$$

where $E_0 = -\mu_{12}/2$ and $\mathcal{K}$ is a constant. It has been shown by Pitaevski [186] that this produces a distribution in momentum space

$$\rho(\mathbf{p}) = \frac{8p_0^5}{\pi^2(p_0^2 + p^2)^4}. \tag{5.10}$$

The constant $p_0^2 = -2\mu_{12}E_0$. It is interesting to note that this is exactly the same as the quantum mechanical distribution. It can also be shown [165] that the probability distribution is uniform in squared angular momentum, l^2, and so we may thus define an angular momentum parameter β by

$$\beta = \frac{l^2}{l_{\mathrm{max}}^2}, \quad 0 \leqslant \beta \leqslant 1 \tag{5.11}$$

which has a uniform distribution over the given range; the maximum angular momentum, l_{max}, is given by

$$l_{\mathrm{max}}^2 = \frac{\mu k^2}{2|E_0|}. \tag{5.12}$$

The remaining four parameters required for the atom consist of three Euler angles ϕ, θ, χ [187–190] and a time translation parameter Λ. The equation for a Keplerian orbit may be shown [191] to be

$$\Lambda = \xi - e \sin \xi, \quad \Lambda = \frac{2\pi t}{T} \in (0, 2\pi) \tag{5.13}$$

where T is the time period and Λ is uniformly distributed in the given range. e is termed the eccentricity and along with ξ is related to the Cartesian representation of the orbit by

$$\begin{aligned} x &= a(\cos \xi - e) \\ y &= a\sqrt{1 - e^2} \sin \xi \end{aligned} \tag{5.14}$$

where

$$a = \frac{|k|}{2|E_0|} \tag{5.15}$$

is the semi-major axis. The Euler angles are given by uniform distributions in the ranges

$$\begin{aligned} 0 &\leqslant \phi < 2\pi \\ -1 &< \cos \theta \leqslant 1 \\ 0 &\leqslant \chi < 2\pi \end{aligned} \tag{5.16}$$

It is shown in [165] that this results in a distribution which is microcanonical; i.e. the distribution in (5.9) is constant over the five parameters $\beta, \Lambda, \phi, \cos \theta$ and ξ.

Employing the co-ordinate system defined in figure 5.1 we have, for the target,

$$\mathbf{r}_{12} = a \begin{pmatrix} \cos \xi - e \\ (1 - e^2) \sin \xi \\ 0 \end{pmatrix} \tag{5.17a}$$

$$\dot{\mathbf{r}}_{12} = \begin{pmatrix} \dot{\mathbf{r}}_{12} \cos \theta - \mathbf{r}_{12}\dot{\theta} \sin \theta \\ \dot{\mathbf{r}}_{12} \sin \theta + \mathbf{r}_{12}\dot{\theta} \cos \theta \\ 0 \end{pmatrix} \tag{5.17b}$$

where

$$r = a(1 - e\cos\xi) \tag{5.18a}$$

$$\theta = \tan^{-1}\left(\frac{(1-e^2)^{1/2}\sin\xi}{(\cos\xi - e)}\right) \tag{5.18b}$$

$$\dot{r} = \left|\frac{2}{\mu}\left(E_0 - \frac{k}{r}\right) - r^2\dot{\theta}^2\right|^{1/2} \cdot \begin{cases} +1, & \text{if } 0 \leqslant \theta < \pi \\ -1, & \text{if } \pi \leqslant \theta < 2\pi \end{cases} \tag{5.18c}$$

$$\dot{\theta} = \frac{l}{\mu r^2}, \tag{5.18d}$$

and for the projectile

$$\mathbf{r}_{23} = \begin{pmatrix} d \\ b \\ 0 \end{pmatrix} - \frac{m_1}{m_{12}}\mathbf{r}_{12} \tag{5.19a}$$

$$\dot{\mathbf{r}}_{23} = \left(\frac{2E_{\text{CoM}}}{\mu_{12,3}}\right)^{\frac{1}{2}}\hat{\mathbf{x}} - \frac{m_1}{m_{12}}\dot{\mathbf{r}}_{12}, \tag{5.19b}$$

where a Cartesian basis has been used.

Equations of Motion

The dynamics can be solved by integration of the equations of motion in either the Hamiltonian or Lagrangian form. The Hamiltonian formalism has been favoured in the past as it is more efficient in the use of symmetry arguments which reduce the computation. In practice it is much simpler and highly effective to work with the physically equivalent six (independent) second-order differential equations of motion following directly from Newton's second law. These were solved by resolving the equations into their Cartesian coordinates, resulting in the 12 first-order coupled ordinary differential equations. The equations of motion are given by [165]

$$\dot{\mathbf{r}}_{12} = \mathbf{v}_{12} \tag{5.20a}$$

$$\dot{\mathbf{r}}_{23} = \mathbf{v}_{23} \tag{5.20b}$$

$$\dot{\mathbf{v}}_{12} = m_{12}^{-1}\frac{\mathbf{r}_{12}}{|\mathbf{r}_{12}|^3} - \frac{\mathbf{r}_{31}}{m_1|\mathbf{r}_{31}|^3} - \frac{\mathbf{r}_{23}}{m_2|\mathbf{r}_{23}|^3} \tag{5.20c}$$

$$\dot{\mathbf{v}}_{23} = m_{23}^{-1}\frac{\mathbf{r}_{23}}{|\mathbf{r}_{23}|^3} - \frac{\mathbf{r}_{12}}{m_2|\mathbf{r}_{12}|^3} - \frac{\mathbf{r}_{31}}{m_3|\mathbf{r}_{31}|^3}, \tag{5.20d}$$

which were then solved numerically using an 8th order Runge-Kutta method of the Numerical Algorithms (NAg) library [192]. Several other integrators were also tried using a simple two-body Kepler system before finally settling on the Runge-Kutta routine. The random number generator from the NAg library [193] was also used.

The accumulation of errors in the integration was monitored by regular checks of the conservation laws, for example, in laser-free collisions trajectories exceeding a relative error of 1 part in 10^4 were discarded from the sample. The reason for failures such as these and also those which did not converge within the integration routines was a close approach between two or more particles resulting in excessively stiff equations. This accounted for almost all failures. Trajectories which failed to enter a prescribed exit channel within a time limit of 10^6 were also rejected. A detailed analysis of some of the individual trajectories which were terminated at $t = 10^6$ were found to enter an exit channel given a little more integration time. The total number of failures did not exceed 0.1% and were thus much less than the statistical fluctuations. On the basis of computing time then it was chosen to ignore them. For all of the calculations the relative numerical precision was 10^{-10}. It was found that this gave the best balance, using double precision arithmetic, between integrator accuracy and accumulation of round-off errors.

Exit Tests

At intervals, a series of tests were performed in order to determine if the collision was over, and if so, the exit channel was identified. These tests, which are similar to those of [184], are displayed in table 5.2.

Defining the classical (continuous) principle quantum number n_c of the capture state by

$$n_c = \left(\frac{\mu_{23}}{2|E_{23}|} \right)^{1/2} \tag{5.21}$$

and the angular momentum number l_c by

$$l_c = \mu_{23}|r_{23} \wedge \dot{r}_{23}| \tag{5.22}$$

we may associate with these semi-quantal numbers n and l by the relations [167,

Table 5.2: Exit tests for scattering, capture and ionisation. A plus sign indicates that the test must be passed, a minus sign indicates that it must be failed and a zero indicates that the test is not made. E_{ij} and $V_{ij} = k_{ij}r_{ij}^{-1}$ denote the centre of mass energy and the interparticle potential respectively of particles i and j, where $r_{ij} = |\boldsymbol{r}_i - \boldsymbol{r}_j|$. The particles are numbered such that 1 and 2 compose the atom in the initial state, i.e. $Z_1 Z_2 < 0$, and $Z_1 Z_3 > 0$. r_{th} was chosen to be 10 and $\gamma = 0.4$.

	test	scattering	capture	ionisation
1.	$\boldsymbol{r}_{13}.\dot{\boldsymbol{r}}_{13} > 0$	+	+	+
2.	$r_{13} > r_{\text{th}}$	+	+	+
3.	$r_{12} > r_{\text{th}}$ or $r_{23} > r_{\text{th}}$	+	+	+
4.	$E_{12} > 0$	-	+	+
5.	$E_{23} > 0$	+	-	+
6.	$\gamma|E_{12}| > |V_{13}| + |V_{23}|$	+	0	+
7.	$\gamma|E_{23}| > |V_{13}| + |V_{12}|$	0	+	+
8.	$r_{12} > r_{\text{th}}$ and $r_{23} > r_{\text{th}}$	0	0	+
9.	$\boldsymbol{r}_{12}.\dot{\boldsymbol{r}}_{12} > 0$ and $\boldsymbol{r}_{23}.\dot{\boldsymbol{r}}_{23} > 0$	0	0	+
10.	$r_{12} < r_{23}$	+	-	0
11.	$r_{12} > r_{23}$	-	+	0
12.	$E_{12} < 0$	+	-	-
13.	$E_{23} < 0$	-	+	-
14.	$\boldsymbol{R}_{23,1}.\dot{\boldsymbol{R}}_{23,1} > 0$	0	+	0
15.	$\boldsymbol{R}_{12,3}.\dot{\boldsymbol{R}}_{12,3} > 0$	+	0	0

184]

$$\left[(n-1)(n-\tfrac{1}{2})n\right]^{\frac{1}{3}} < n_c \leqslant \left[n(n+\tfrac{1}{2})(n+1)\right]^{\frac{1}{3}} \tag{5.23a}$$

and

$$l < \frac{n}{n_c} l_c \leqslant l+1 \tag{5.23b}$$

The weighting n/n_c is to ensure that the inequality $l < n$ is satisfied at all times. From the theory of Keplerian orbits, the relative separation r of two particles is in the range given by

$$0 < r \leqslant 2a = \left|\frac{k}{E}\right| = \frac{2|k|n_c^2}{\mu} \tag{5.24}$$

and so the density of orbits is proportional to n_c^2. Integrating between the limits of the inequality in equation (5.23a) we obtain

$$\int_{\left[(n-1)\left(n-\frac{1}{2}\right)n\right]^{1/3}}^{\left[n\left(n+\frac{1}{2}\right)(n+1)\right]^{1/3}} n_c^2 \, \mathrm{d}n_c \propto n^2. \tag{5.25}$$

which agrees with the total quantum degeneracy

$$\sum_{l=0}^{n-1}(2l+1) = 2\frac{n(n-1)}{2} + n = n^2. \tag{5.26}$$

Statistics and Cross Sections

After sufficient sampling of phase-space involving N trajectories in total, the cross sections for capture (σ^c) and ionisation (σ^i) are calculated

$$\sigma^{c,i} = 2\pi \int_0^\infty p^{c,i}(b)b \, \mathrm{d}b. \tag{5.27}$$

In practice this was calculated by the quadrature

$$\sigma^{c,i} = 2\pi \sum_{j,k} p^{c,i}(j,b_j)b_j \, w_k \, \Delta b_k \tag{5.28}$$

where $p^{c,i}(j,b_j)$ is the probability of a capture/ionisation event happening at an impact parameter $b_k \leqslant b_j \leqslant b_k + \Delta b_k$ for a collision, labelled j $(1 \leqslant j \leqslant N)$. The

weights w_k were taken according to Simpson's rule and the range of integration covered all values of the impact parameter for which $p^{c,i}(j, b_j) \neq 0$.

If we were to take a distribution of trajectories in which the distribution of impact parameters is proportional to $b\,db$ in a range $(0, b_{\max})$ we may write

$$n_i(b)\,db = \frac{2\pi N p_i(b) b\,db}{\pi b_{\max}^2} = \frac{2 N p_i(b) b\,db}{b_{\max}^2} \qquad (5.29)$$

where N is the total number of trajectories, then (5.27) becomes

$$\sigma_i = \frac{\pi b_{\max}^2}{N} \int_0^{b_{\max}} n_i(b)\mathrm{d}b = \pi b_{\max}^2 \frac{n_i}{N} \qquad (5.30)$$

where n_i is the total number of events i. The standard statistical error in σ_i is then

$$\Delta\sigma_i = \sigma_i \left(\frac{N - n_i}{N n_i}\right)^{\frac{1}{2}} \qquad (5.31)$$

This is the method used in previous CTMC simulations [164, 166, 184].

In the present work an importance sampling function was used in randomizing the impact parameter, b. The dominant contribution to most cross sections comes from a region centred on a specific impact parameter, the peak, which we call $b = b_0$, and there is little contribution from b close to zero and b large. It makes sense then to choose a set of impact parameters concentrated around b_0. The distribution used is given by

$$\left.\begin{array}{l} b = b_0\sqrt{x} \\[4pt] b = b_0 - b_m \ln x \end{array}\right\} \ 0 \leqslant x \leqslant 1 \qquad (5.32)$$

where x is uniform in the range given and values of b were chosen so that they fell in the ranges $b < b_0$ and $b \geqslant b_0$ in the ratio approximately 1:4. The values of b_0 and b_m were chosen by experimentation. It was found that for antiproton capture b_0 could be chosen accurately using a formula suggested by the small-angle scattering formula (see e.g. [139]), where $b_0 = AE^{-1/4}$ for a potential $V = kr^{-4}$, and b_m was chosen to be 1.0. For ionisation it was found that $b_0 \approx 1.0$ and $b_m \approx 2.0$ for all energies.

Presence of a Laser Field

The presence of a laser introduces a perturbation which, in the dipole approximation and with the choice of the length gauge, has the form

$$H' = -F(t)\cos(\omega t + \varphi)\sum Z_i \mathbf{r}_i \cdot \mathbf{e} \qquad (5.33)$$

where $\mathbf{e}$ is the direction of polarization of the laser, ω is the angular frequency, and $F(t)$ is the electric field amplitude. The phase of the laser, φ, is significant whenever the optical cycle time is longer than the time taken for the collision interaction. At higher velocities it is necessary to choose a random selection of phases to allow for this variability. The peak field, F_{max}, is related to the light intensity, I, by $F_{\text{max}} = \sqrt{2I/\varepsilon_0 c}$. In this work the field strength is measured in atomic units. The field was ramped smoothly on and off over a timescale τ such that

$$F(t) = F_{\text{max}} \times \begin{cases} \sin^2(\pi t/2\tau), & 0 \leqslant t \leqslant \tau \\ 1, & \tau < t < \Delta T - \tau \\ \sin^2(\pi(\Delta T - t)/2\tau), & \Delta T - \tau \leqslant t \leqslant \Delta T. \end{cases} \qquad (5.34)$$

A large number of collisions are simulated which sample the full range of particle phase space and take into account the random laser pulse. For the case of perpendicular polarisation the angle of the impact parameter in the yz plane was also randomised.

5.3 Field-Free Capture

In this section results for antiproton capture in the absence of fields are presented [194]. Results for antiproton capture and collisional ionisation were used to establish the accuracy of the code, within the validity of a classical model, and to extend the range of the data. The statistical error due to the random sampling of the Monte Carlo procedure, denoted by the standard deviation s, was sufficiently small that the error bars, $\pm s$, are smaller than the point sizes in the figures. Sample results for the hydrogen target are given in table 5.3 which are found to agree well with previous simulations [172].

Table 5.3: Capture cross section, $\sigma^c = \sum_{nl} \sigma^c_{nl}$, for antiproton collisions with atomic hydrogen.

E (a.u.)	σ^c (πa_0^2)	E (a.u.)	σ^c (πa_0^2)
0.100	5.03	0.430	2.73
0.125	4.44	0.460	2.68
0.150	4.10	0.480	2.62
0.175	3.83	0.500	2.58
0.200	3.62	0.510	2.49
0.225	3.48	0.520	2.20
0.250	3.36	0.530	1.85
0.275	3.25	0.540	1.40
0.300	3.14	0.550	1.02
0.325	3.03	0.560	0.64
0.350	2.96	0.580	0.31
0.375	2.88	0.600	0.16
0.400	2.81	0.620	0.09

Table 5.4: Total capture cross sections (σ^c) for pion (π^-) collisions with atomic hydrogen.

E (a.u.)	σ^c (πa_0^2)	E (a.u.)	σ^c (πa_0^2)
0.100	5.13	0.500	2.65
0.120	4.67	0.520	2.42
0.150	4.20	0.540	2.08
0.200	3.73	0.560	1.64
0.250	3.47	0.580	1.16
0.300	3.22	0.600	0.76
0.350	3.03	0.620	0.44
0.400	2.90	0.640	0.31
0.425	2.82	0.660	0.19
0.450	2.74	0.680	0.14
0.480	2.71	0.700	0.11

Figure 5.2: Comparison of capture cross sections for antiprotons ○ and negative pions □ incident on atomic hydrogen. Also shown for comparison are Perturbed Stationary State results ◇ of Ohtsuki *et al* [181].
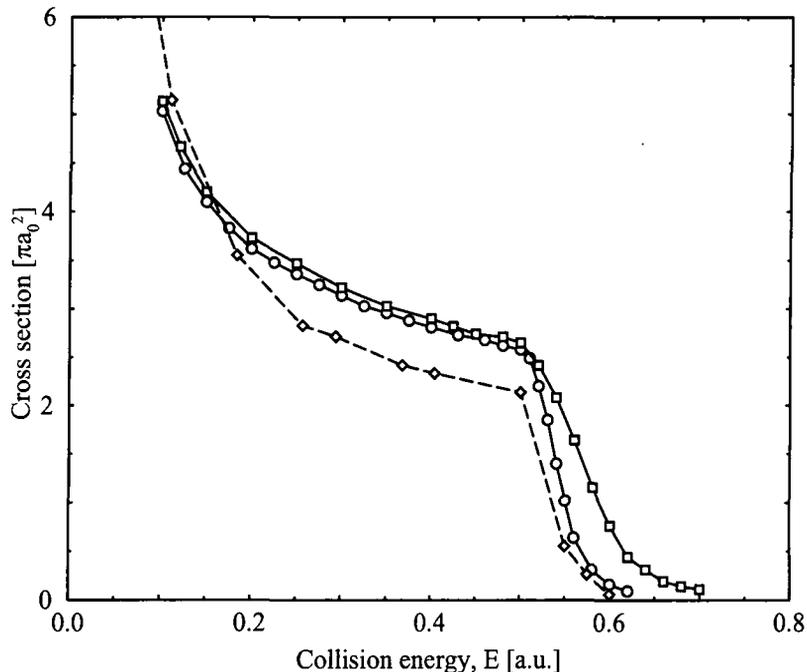
The present data is more extensive and statistically accurate than previous CTMC simulations [164, 172, 184, 195]. As an example of the sampling error the cross section for capture for $E = 0.2$, given by $\sigma^c = 3.62 \ \pi a_0^2$, was obtained from $N = 5 \times 10^4$ trajectories which equates to a standard deviation of $s = 0.02 \ \pi a_0^2$, that is, less than 1%. Similarly the cross section for collisional ionisation, σ^i, of positronium for $E_{\text{lab}} = 10$ keV, given by $\sigma^i = 0.32 \ \pi a_0^2$, was obtained from $N = 10^5$ trajectories with $s = 0.01 \ \pi a_0^2$, around 3%.

It has been noted [164] that cross sections for capture of μ^- ($m_\mu \approx 207 \ m_e$) [164, 170, 178, 184] and $\bar{p}$ by hydrogen are very similar. This reflects the fact that the electron ejection process at low energies involves a centrifugal energy barrier against the incident particle approaching the critical distance of ionisation [196] rather than a condition dependent on the collision velocity, and is termed adiabatic ionisation [163]. Results from the present CTMC work for negative pion π^-

Figure 5.3: Partial cross sections, $\sigma_n^c = \sum_l \sigma_{nl}^c$, for protonium formation in a quasi-quantum level n, following antiproton-hydrogen collisions. Collision energy in atomic units: $\bigcirc$ $E = 0.05$; $\square$ $E = 0.1$; $\Diamond$ $E = 0.2$; $\triangle$ $E = 0.3$; ∇ $E = 0.4$.
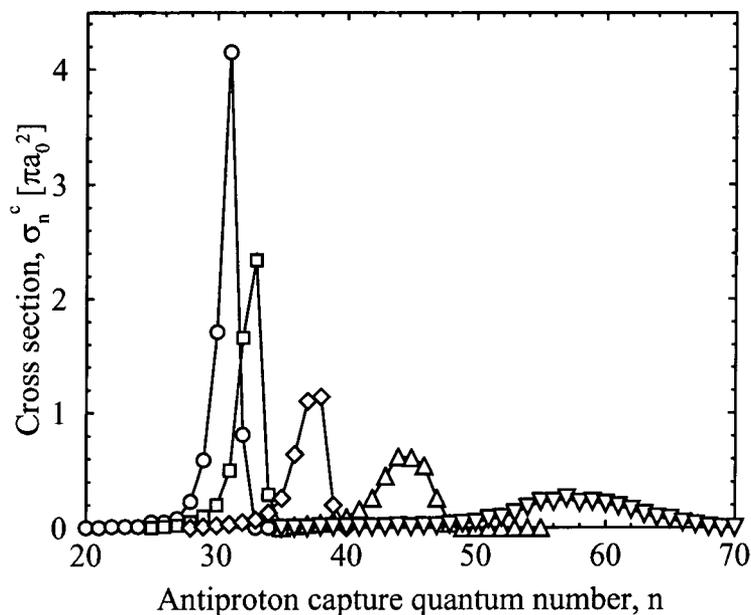
Figure 5.4: Partial cross sections $\sigma_l^c = \sum_n \sigma_{nl}^c$ for protonium formation in a quasi-quantal state l following antiproton-hydrogen collisions. Collision energy in atomic units: $\bigcirc$ $E = 0.1$ and $\square$ $E = 0.3$.
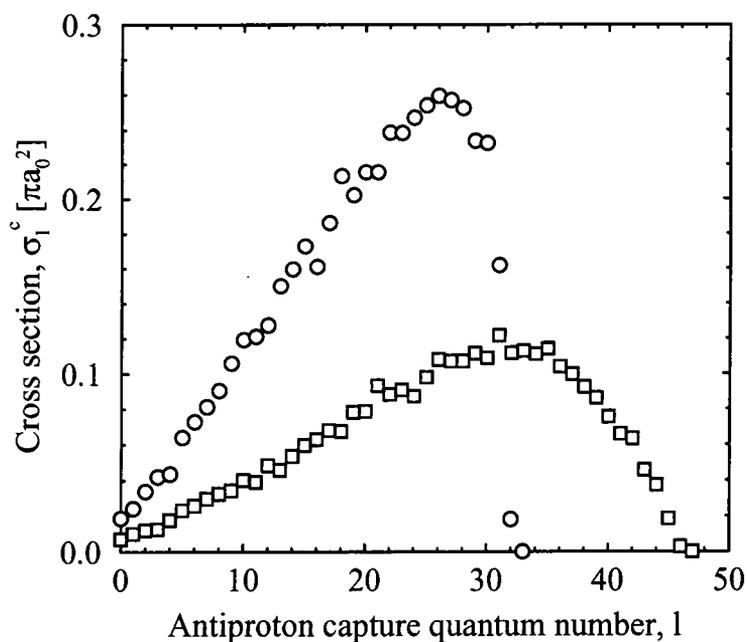
$(m_\pi \approx 273 \, m_e)$ capture by hydrogen are given in table 5.4 and plotted with the antiproton results for comparison in figure 5.2. It can be seen that the data presented here follows this trend very well.

The distribution of antiprotons in subshells, σ_{nl}^c, has been considered by Cohen [164, 197]. If the electron is liberated with an energy, $\varepsilon > 0$, (in the center of mass frame) then the protonium energy, $E_n = -\mu_{23}/(2n^2)$, is determined by $E_n = E - \mu_{12}/2 - \varepsilon$. Slow electron escape, $\varepsilon \approx 0$, means that capture can occur near the level $n_{\max} \approx \sqrt{\mu_{23}/(1 - 2E)}$. As can be seen from figure 5.3 the dominant capture indeed occurs near this limit. The sharpness of the σ_n^c distributions indicates a thin capture shell around the atom corresponding to $n \gg 1$ and partially explains why classical theory works rather well in this case. At higher energies the ejected electron energy spectrum is broader, corresponding to antiproton-electron collisions in which momentum and energy transfer is required to effect capture. This leads to a broadening in the σ_n^c distribution and the maximum of the curve then favours lower n. Since the target atom has spherical symmetry, the summation over all $n-$ and m-levels yields cross sections which reflect the statistical weight $\sigma_l^c \propto (2l+1)$ [163]. In figure 5.4 the distributions, σ_l^c, are seen to follow this trend until the cut-off at $l \sim n_{\max}$ corresponding to the n distribution (figure 5.3). Using the semiclassical correspondence $l \sim \mu_{12,3} vb$, figure 5.4 can also be viewed as the weighted capture probability $bp^c(b)$ which has a sharp cut-off for orbits which pass the atom outside the capture radius, R_c. The antiprotons are captured into a wide distribution of states including a small proportion in the nearly circular orbits $l \sim n$ associated with long-lived states of antiprotonic helium [158].

At energies above the ionisation threshold the capture cross section falls away rapidly as a result of the requirement for momentum matching [198] and quantal or classical perturbation theory can be applied. For example, the distorted-wave Born approximation for antiproton capture to the ground state, $\bar{H}(1s)$, at $E_{\text{lab}} = 61$ keV is $\sigma^c = 0.56 \, \pi a_0^2$ [198]; the less reliable plane-wave Born approximation predicts $1.60\pi a_0^2$. The classical estimate is much smaller at $\sigma = 0.18 \, \pi a_0^2$. At energies below 100 keV the plane-wave Born approximation leads to gross over-estimates of the cross section [163].

Figure 5.5: Capture ● and ionisation ■ cross sections for antiproton impact on positronium, and their dependence on the antiproton kinetic energy, E_{lab}. Comparison with CTMC results of Ermolaev [195] for capture,◊ and ionisation, △. The laboratory and centre of mass energies are related by (5.7).
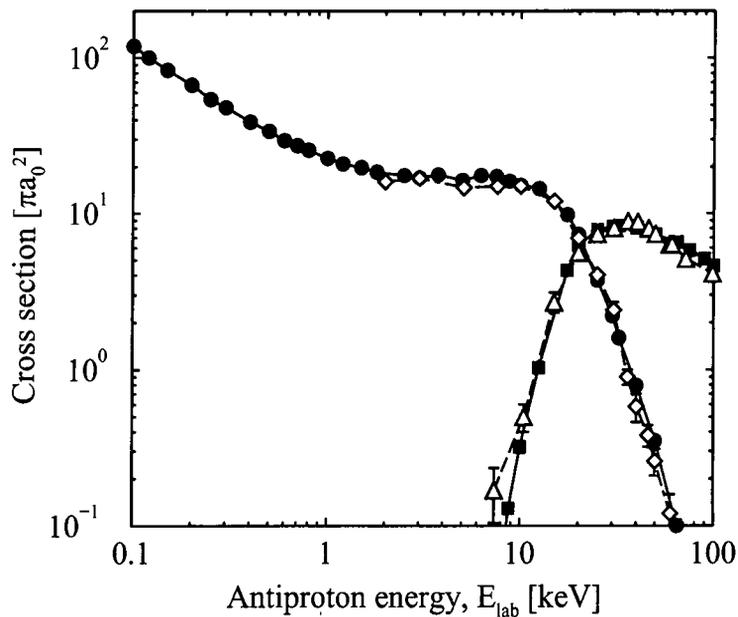
Figure 5.6: Capture $p(b)$ of antiprotons by hydrogen as a function of impact parameter. The numbers refer to the impact energies.
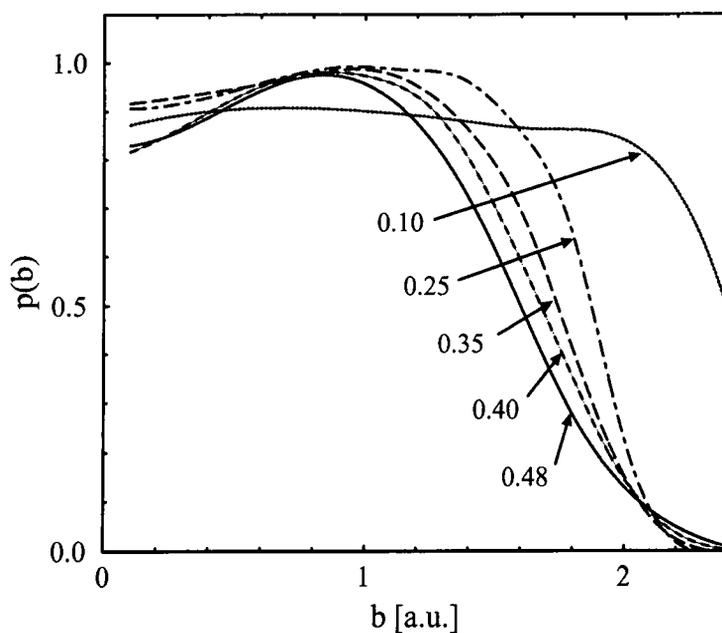
Table 5.5: Capture (σ^c) and ionisation (σ^i) cross sections for antiproton $(\bar{p})$ collisions with positronium (Ps). The laboratory and centre of mass energies are related by (5.7).

E_{lab} (keV)	σ^c (πa_0^2)	E_{lab} (keV)	σ^c (πa_0^2)	σ^i
0.10	119.0	5.00	16.4	0.00
0.12	100.0	6.25	17.6	0.00
0.15	83.7	7.50	17.4	0.02
0.20	67.2	8.75	16.2	0.13
0.25	54.4	10.0	15.2	0.32
0.30	48.0	12.5	14.5	1.0
0.40	38.9	17.5	9.8	4.3
0.50	33.9	20.0	7.3	6.2
0.60	29.5	25.0	3.7	7.8
0.70	27.4	30.0	2.2	8.2
0.80	25.6	32.5	1.6	8.3
1.00	22.7	40.0	0.79	8.0
1.20	21.0	50.0	0.35	7.3
1.50	19.8	65.0	0.10	6.5
1.80	18.6	75.5	0.05	5.8
2.50	17.6	90.0	0.00	5.1
3.00	17.0	100	0.00	4.6
3.75	17.8			

Antiproton collisions with positronium has been proposed as an efficient means of producing cold antihydrogen [17]. Indeed this scheme has been proved feasible by the capture of protons by positronium [57, 58]. CTMC results from the current work for this process are shown in figure 5.5 along with previous results for $E_{\mathrm{lab}} > 2$ keV by Ermolaev [195]. The results agree very well with experimental results [57, 58] for the charge conjugate reaction $p + \mathrm{Ps} \longrightarrow \mathrm{H} + e^+$. In [57, 58] the cross section for hydrogen formation at 13.3 keV is determined to be $\sigma^c = 9 \pm 3$ πa_0^2, compared with the current results of 10 πa_0^2, and at $E_{\mathrm{lab}} = 11.3$ keV, $\sigma^c = 30 \pm 10$ πa_0^2, compared with the CTMC results, 15 πa_0^2.

It can be seen in figure 5.5 that the capture cross section for positronium has a prominent plateau feature over the energy range 2–10 keV. This is suggestive of a geometric target corresponding to a critical capture radius. Employing the principles of conservation of energy and angular momentum and assuming that capture occurs at an antiproton-positron radius, R_c, where the electronic energy becomes positive, we arrive at the adiabatic formula [163] for the cross section in terms of the critical distance

$$\sigma^c = \kappa \pi R_c^2 \left[1 + E^{-1}(R_c^{-1} + \varepsilon_i) \right],\tag{5.35}$$

where $\kappa \leqslant 1$ is an empirical factor representing the efficiency of capture and $\varepsilon_i = -\frac{1}{2}\mu_{12}$ is the target energy. If we assume that R_c corresponds to the limit of the classical electron distribution this simple model seems to explain the general trends in tables 5.3, 5.4 and 5.5. In fact the data is very well represented by the following fits for the parameters: for $\bar{p} + \mathrm{Ps}$, $R_c = 3.5$, $\kappa = 0.96$. For $\bar{p} + \mathrm{H}$, the fit is not quite as good; we find $R_c = 1.60$, $\kappa = 0.87$, gives a reasonable approximation to the data. Given that the Ps radius is twice as large as that of H one might expect that $R_c(\bar{p} + \mathrm{Ps}) \approx 2R_c(\bar{p} + \mathrm{H})$. It can be seen from the fitted values that this is indeed the case to a good approximation $(3.5/1.6 = 2.2)$. Shown in figure 5.6 are $p(b)$ capture probabilities as a function of impact parameter for antiprotons on atomic hydrogen. The saturation of capture for smaller impact parameters suggested by the adiabatic model is clearly visible.

The capture radius model suggests that an increase in the antihydrogen production cross section might be obtained if the positronium could be either excited or polarised by an external field. This would improve the efficiency of experimental designs to produce cold antimatter. In simple terms the positronium atom would have a larger orbit and charge volume and hence R_c would be increased.

5.4 Laser-Assisted Capture

The enhancement of capture due to laser assistance has been studied in the Born approximation [199], however it has been established [163] that for laser-free collisions this model is inadequate at energies below the ionisation threshold [198]

Table 5.6: Capture (σ_L^c) and ionisation (σ_L^i) cross sections for antiproton impact on positronium in the presence of a laser field. The laser polarisation is linear and oriented either parallel ($\parallel$) or perpendicular ($\perp$) to the antiproton beam. The laboratory and centre of mass energies are related by (5.7).

E_{lab} (keV)	Field strength F_{max} (a.u.)	λ (nm)	laser polarisation	σ_L^c (πa_0^2)	σ_L^i (πa_0^2)
1	.... without laser			23.0	0.00
	0.01	1064	$\perp$	24.3	0.04
			$\parallel$	25.5	0.05
		248	$\perp$	24.0	0.34
			$\parallel$	24.0	0.30
	0.02	1064	$\perp$	25.2	2.2
			$\parallel$	27.8	2.4
		248	$\perp$	39.0	†
			$\parallel$	40.0	†
15	.... without laser			12.1	2.6
	0.01	1064	$\perp$	9.8	6.7
			$\parallel$	11.0	4.4
		248	$\perp$	12.0	2.8
			$\parallel$	13.1	1.5
	0.02	1064	$\perp$	7.0	12.0
			$\parallel$	10.4	8.5
		248	$\perp$	11.0	7‡
			$\parallel$	13.0	6‡

† Too much ionisation was present at high impact parameters (photoionisation) for the ionisation cross section to be determined here.

‡ A small amount of photoionisation was present in the results here and an estimate of the ionisation cross section was made.

Figure 5.7: Photoionisation probability of positronium by a 248 nm laser. O $\tau = 40$; □ $\tau = 60$. Dashed and dot-dashed lines are linear regression fits. The different intercepts are a result of the different pulse rise times resulting in more/less time at peak intensity.
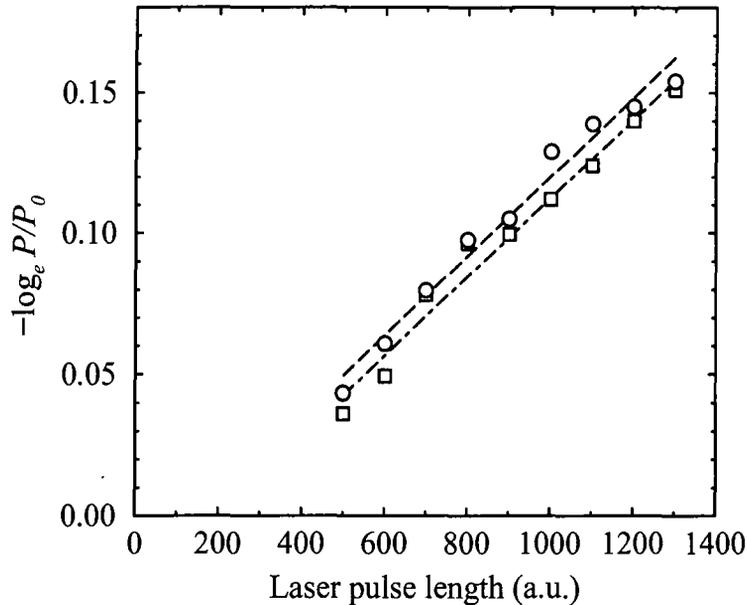
in that it grossly overestimates the capture process. Nonetheless, calculations at high energies using this approximation predicted an enhancement of capture in some cases by a factor of ten or more [199, 200]. However, a closer analysis revealed that, at the laser intensities considered, rapid photoionisation [201] would dominate the process resulting in the depletion of capture. Here the process is considered over the energy range of interest to experiment. In particular laser-assisted formation of antihydrogen is considered at two collision energies, $E_{lab} = 1$ keV and 15 keV, for laser wavelengths of $\lambda = 248$ nm and $\lambda = 1064$ nm linearly polarised with alignment parallel to and perpendicular to the collision axis (direction of the antiproton beam) [194].

We assume that the population of atoms P from an initial ensemble of P_0 as a function of pulse length ΔT follows the formula

$$\log \frac{P}{P_0} = -\Gamma(\Delta T).$$ (5.36)

Shown in figure 5.7 is a fit for the photoionisation rate of positronium subjected

to a 248 nm laser of peak field strength $F_{\text{max}} = 0.02$. The results of two ramping times are shown, $\tau = 40$ and $\tau = 60$.

Classical models of photoionisation have previously been used successfully in the qualitative understanding of the response of atoms to intense light [202]. In order to test the current classical model of laser-positronium interaction quantitatively the photoionisation rate of isolated positronium was calculated. Two field strengths, $F_{\text{max}} = 0.01$ a.u. and 0.02 a.u., corresponding to intensities of $I = 3.5 \times 10^{12}$ W cm^{-2} and $I = 1.4 \times 10^{13}$ W cm^{-2} respectively, were investigated. The ionisation yield was calculated for a variety of pulse lengths to establish a photoionisation rate Γ. At $I = 3.5 \times 10^{12}$ W cm^{-2} the classical model predicts that very little ionisation will occur: $\Gamma < 2 \times 10^{-7}$. For the stronger field, $\Gamma = 1.2 \times 10^{-4}$ for $\lambda = 248$ nm and $\Gamma = 1.1 \times 10^{-4}$ for $\lambda = 1064$ nm. These results were compared to accurate quantal calculations using the Floquet method [203]. For $\lambda = 248$ nm the Floquet method predicts a decay rate of $\Gamma = 1.80 \times 10^{-4}$ for $F_{\text{max}} = 0.01$ and $\Gamma = 1.26 \times 10^{-3}$ for $F_{\text{max}} = 0.02$. For $\lambda = 1064$ nm the quantal rates are estimated at $\Gamma \approx 1.5 \times 10^{-5}$ for $F_{\text{max}} = 0.01$ and $\Gamma = 4 \times 10^{-3}$ for $F_{\text{max}} = 0.02$. These results confirm that classical models can underestimate multiphoton ionisation rates by large factors. Note that for long-wavelength high-intensity light the dominant mechanism of photoionisation is through tunneling transitions, a process which is classically forbidden.

For $E_{\text{lab}} = 1$ keV the laser was ramped on over a time period of $\tau \approx 80$, beginning at an initial internuclear separation of $d = 40$, so that the laser had always reached full intensity during the collision. Tests of the pulse rise time taken over the range $\tau = 40$–120 found that the cross sections were not sensitive to the precise value of τ. Moreover, with the laser field intensities used, there was not a significant loss due to photoionisation over the typical collision times and so these losses could be neglected. Given that the optical cycle times are 147 a.u. for $\lambda = 1064$ nm and 34 a.u. for $\lambda = 248$ nm the random laser phase, φ, must be taken into account by statistical averaging. Displayed in table 5.6 are results for laser assisted antihydrogen formation. It was found that the combination of laser and antiproton was effective in producing ionisation of the positronium while neither were effective alone. At 1 keV the enhancement due to the laser was large, with a 4–

background laser in collisions with positronium has been modelled. Within the limitations of the classical model, for both the laser interaction and the collisional interaction, statistically accurate cross sections for protonium and antihydrogen formation were obtained over a wide range of energies and the energy dependence of the process was established. The results agree very well with experimental data for proton capture by positronium [57, 58]. The present calculations found that the addition of the laser field led to enhancement of the formation of antihydrogen of the order of 4–70% for an antiproton collision energy of 1 keV. It appears that the addition of a laser field could act as a useful accelerant for such schemes. While the classical model has shortcomings these preliminary results are promising. A more authoritative statement on the viability of such schemes would require quantal modelling of low-energy laser-assisted antiproton capture by positronium, or equivalently laser-assisted positron-atom scattering leading to the formation of positronium. Such a study seems warranted and worthwhile.

Concluding Remarks

The results of this thesis have added extra understanding to the area of exotic particle collisions using two very different computational approaches which reflect the different collisions systems studied.

In part I positrons were scattered off ionic targets using the close coupling approximation including pseudostates, the first complete study to be done for positron-ion scattering. For this, a new computational method, the minimum-norm method, was developed which is an extension of a previously reported least-squares method [2]. The minimum-norm method allowed the use of a larger basis, including a large number of pseudostates on one centre, and hence the determination of converged cross sections for all processes, including excitation, ionisation and electron capture. The development of the minimum-norm method and demonstration of its ability to compute converged positron-ion cross sections is a first step towards tackling more complex charged systems, such as Li^+.

In part II the production of protonium, $p\bar{p}$, and antihydrogen, $\bar{H}$, from antiproton collisions with hydrogen and positronium was investigated using the classical trajectory Monte Carlo (CTMC) method. Both of these processes are of great interest to experimentalists currently working on projects (ATRAP [14], ATHENA [15] and ASACUSA [16]) at CERN to produce significant quantities of these antiprotonic compounds for spectroscopic purposes. It is known that the production of $p\bar{p}$ and $\bar{H}$ will be limited to small quantities using current techniques and the development of ways to enhance the yield is crucial for the projects' success. Following this observation it was decided to investigate the effect of the application of a background laser field to the reaction $\bar{p}$-Ps. It was found, with the CTMC method, that the presence of the laser enhanced the yield of antihydrogen significantly. Following this observation it is suggested that a thorough investigation of the effects of laser enhancement using quantal modelling would be of great interest.

Appendix A

Close Coupling Code

In this appendix some of the more technical details related to the design, layout and operation of the code used to solve the close coupling equations are outlined. The discussion here is limited to details of the serial algorithm only; issues specific to the parallelisation of the code are instead addressed in appendix B.

Shown in figure A.1 is a flow diagram depicting the main order of calculation in the code. The code was written in modular form (table A.1, p. 118) making good use of the object-oriented capabilities of FORTRAN 90. Data belonging to each individual partition was confined almost exclusively to separate modules greatly reducing the simplicity and robustness of the code; most of the modular structure within the program though has not been depicted. The code used to construct major parts of the calculation, such as the basis functions, angular coefficients, R-matrix propagation, etc. was also confined to plug-in modules; this way it was much easier to enforce the principle of least privilege[1] among variables and to thoroughly test components of the code individually. Programming in this way is nowadays seen as good practice, particularly when writing large complex codes. Especially useful in this approach is the ability, if the modules are written well enough, to use modules in others codes: what is known as software recycling.

We begin by discussing the Dynamic Memory Manager (DMM), a central part of the robustness of the code, followed by a discussion, with examples, of the program output.

Figure A.1: Main program block diagram depicting main order of calculation.
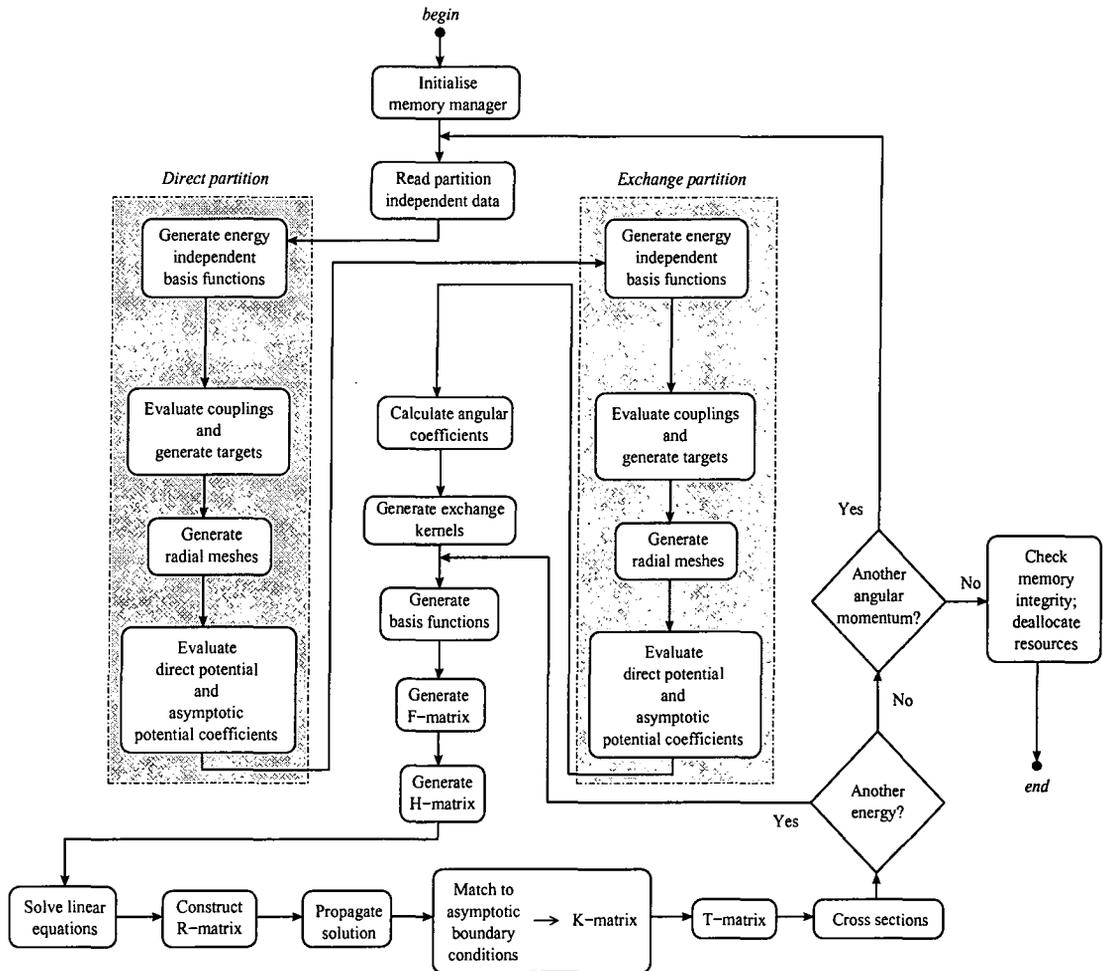
Dynamic Memory Manager

Of utmost importance in a numerical code is robustness and the ability to readily identify and eradicate bugs. Many of the bugs that are the most subtle and difficult to find are those that do not always cause an immediately obvious disturbance within the code. Especially in a numerical code such as this one a great number of these bugs are those which involve over-writing of data due to out-of-range subscripts used with array structures. These can, in many cases, be found by compiling the code with array-subscript-checking turned on (an option on many compilers). This, however, results in a large and slow code and so cannot be used for large-scale runs, during which a significant number of these bugs will not become apparent.

Table A.1: Modules within the close coupling code.

Module name	Brief description
am_algebra	Angular momentum algebra such as 3-j, 6-j and 9-j symbols, Clebsch- Gordan coefficients, Racah coefficients, ...
basis_fns	Laguerre, Slater, Calloway oscillatory and shifted Legendre functions
bf_prop	Performs R-matrix propagation
bf_ptrs	Defines pointers to basis functions and channel data
cheb	Chebyshev interpolation
coulomb	Generates Coulomb wave functions and Whittaker functions
direct	Direct partition code
dyn_memry	Dynamic memory management
exac	Angular coefficients for exchange kernels
exchange	Exchange partition code
gailitis	Gailitis asymptotic matching package
grids	Returns least-squares/minimum-norm and quadrature meshes
io_units	Control of program input and output
least_squares	Least-squares code
max_vals	Controls hard-wired program limits (no. channels etc.)
precisn	Precision parameters and machine dependent data
pseudo	Generates pseudostate targets using Laguerre functions
radial	Radial functions and grids for Slater targets
tgts	Defines target data
rkt_mats	Calculates R-, K- and T-matrices
timing	CPU timing information
tls1	Main program

Figure A.2: Hash table within the dynamic memory manager. The actual memory allocations are depicted as the dashed-line boxes which are pointed to by the allocation nodes of the hash table. These allocation nodes contain information regarding the size, contents type (integer, real, complex, scalar, n-dimensional array ...) and name. Shown is a close up of one of the allocation nodes.
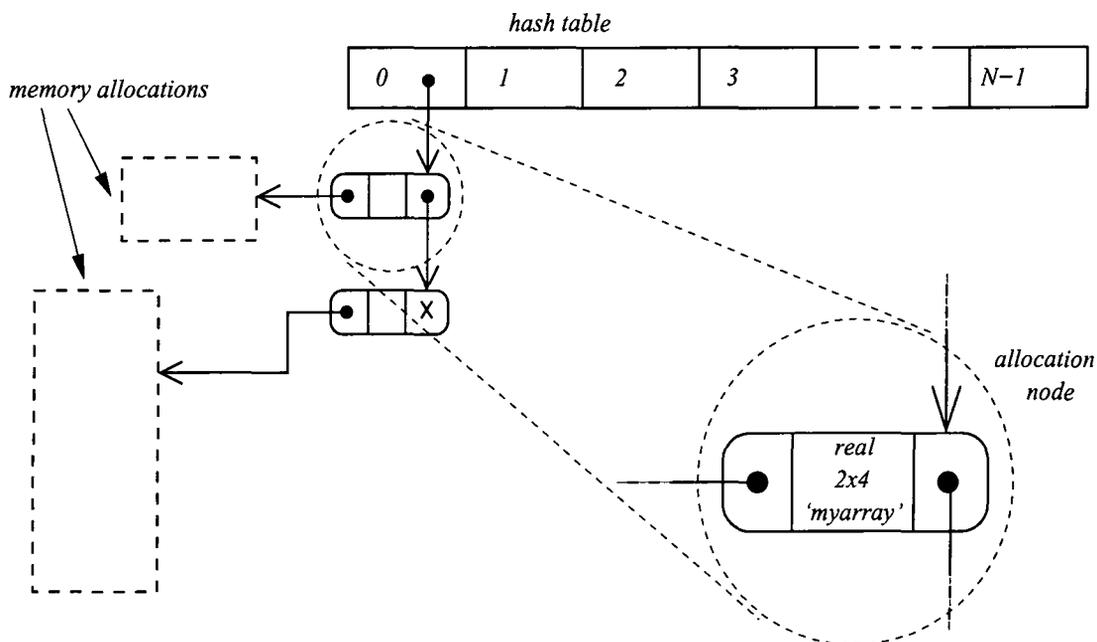
In the code, a memory manager was used (written in FORTRAN 90) to handle dynamic memory allocations.[2] Built into the manager were regular checks of the integrity of the memory that do not significantly slow down the code and at the same time are very good at warning the user of these kinds of bugs. The manager had a hash table structure depicted in in figure A.2. Memory allocations were made by calls to the manager; the manager then allocated the necessary space with additional 'padding' either side. In these padded areas set values were inserted in memory. Overwriting the end of the memory allocation would almost certainly involve corruption of these specific values which would then be quickly detected and flagged by an error. The manager also stores information regarding the allocation which is used to detect multiple allocations of the same name and, at the end of the program, whether or not all allocations have been removed, a sign of a possible program logic error somewhere. These memory allocations are organised by a hash

table structure: a number between 0 and $N-1$ is generated by each variable name, called a hash value, which then indexes the location of the variable attributes data in a table. Multiple allocations with the same number are simply strung together in a linked list structure. The hash table approach makes it quick and easy to locate a variable amongst a large number of allocations. Shown in table A.2 is selected output from the memory manager for a 29-state run, $J = 6$, showing memory usage information and statistics.

A further advantage of the DMM is that controlled access to memory allocations may be made with the DMM from anywhere within the program. A computer scientist may be horrified by this programming practice saying that it violates the principle of least privilege, which technically speaking it does; however, in a numerical code such as this one I believe that when used carefully it can be justified. Consider important allocations such as the direct potentials and exchange potentials. It is clear that there is only ever one of each in existence during the execution of the program and that they exist for the same duration every time. I can thus see no justification as to why, so long as the program logic is carefully constructed, these allocations should not be global.[3] Given the large amount of data generated by a program such as this one, making such allocations global drastically reduces the number of arguments that need to be passed between procedures and thus greatly enhances the readability of the program. This, in turn, leads to a lower likelihood of a programming error in data passing. There are, of course, a great number of other memory allocations for which the principle of least privilege should be enforced, but the distinction is generally quite clear.

Table A.2: Typical memory usage of the close coupling code. The data shown is from a 29-state calculation for $J = 6$.

HASH	NAME	d1	d2	d3	TYPE	SIZE
2	cfd	60	60	2	real	56.25kB
3	psi	225	440	0	real	773.44kB
3	cfe	4	4	2	real	0.25kB

4	phip	225	6300	0	real	10.81MB
5	phiq	800	6300	0	real	38.45MB
7	sphid	6300	0	0	real	49.22kB
8	v1	13440	2560	0	real	262.50MB
9	v2	13440	2560	0	real	262.50MB
10	kmat	61	61	0	real	29.07kB
13	mydp	22720540	0	0	real	173.34MB
14	hx1	800	0	0	real	6.25kB
17	xchl_opn	4	0	0	integer	0.02kB
20	sphiq	800	6300	0	real	38.45MB
24	rx1	800	0	0	real	6.25kB
25	kk	60	0	0	real	0.47kB
26	xi	32	0	0	real	0.25kB
27	sphi	225	6300	0	real	10.81MB
28	dquadr	224	2	0	integer	1.75kB
34	hm	6740	64	0	real	3.29MB
34	v1t	896	48000	0	real	328.13MB
37	mmats	14336	6740	0	real	737.19MB
37	phiqp	800	6300	0	real	38.45MB
37	hp	224	0	0	real	1.75kB
38	psiqp	640	440	0	real	2.15MB
45	hx	224	0	0	real	1.75kB
47	rp	225	0	0	real	1.76kB
49	equadr	224	2	0	integer	1.75kB
55	rx	225	0	0	real	1.76kB
57	kkp	4	0	0	real	0.03kB
59	vd	224	60	60	real	6.15MB
60	ve	224	4	4	real	28.00kB
62	phi	225	6300	0	real	10.81MB
63	psid	440	0	0	real	3.44kB
65	tmm	61	61	0	complex	58.14kB
65	v2t	896	48000	0	real	328.13MB
66	lsqw	14336	0	0	real	112.00kB

... continued from previous page

66	hp1	640	0	0	real	5.00kB
68	spsi	225	440	0	real	773.44kB
72	fm	6740	6740	0	real	346.59MB
75	psip	225	440	0	real	773.44kB
76	psiq	640	440	0	real	2.15MB
76	rp1	640	0	0	real	5.00kB
78	spsid	440	0	0	real	3.44kB
88	chl_opn	64	0	0	integer	0.25kB
90	plm	32	21	0	real	5.25kB
91	spsiq	640	440	0	real	2.15MB
92	phid	6300	0	0	real	49.22kB
95	wi	32	0	0	real	0.25kB
97	dchl_opn	60	0	0	integer	0.23kB
100	dpbuf	22720540	0	0	real	173.34MB

Number of allocations:		current =	50
		maximum =	61
		to date =	1753
TOTAL MEMORY ALLOCATED:		current =	2.71GB
		maximum =	2.72GB

Current memory allocations comprised of

integer:	7.52kB
real:	2.71GB
complex:	60.05kB

Mem limit set to	3.00GB

The integrity of the memory allocations was checked at regular intervals within the program, including at the very end and every time a deallocation was made. Due to the hash table structure the DMM is efficient and there is no observable degradation of performance through its use.

Sample Output

Shown in figure A.3 is sample output of some of the error diagnostics. The columns are, in order,

Figure A.3: Sample output from the minimum-norm code showing some of the error diagnostic output. The output has been truncated; only selected solutions have been shown. The 2p channel is one of the 2p excitation channels; the 1s channel corresponds to ground-state capture. Total angular momentum is $J = 2$; the collision energy is $E = 175$ eV; the collision system is e^+-He$^+$. The meanings of the columns and abbreviations are discussed in the text.

Channel	sol		Max. Error		Wfn. Max.	B.C.s	Exch. pot.		Chan.	#bfn	Coeff. conv					
# nme o	#	rx	nx Abs.	Norm.	Abs.	at	Abs.	Norm.	AM.	k	e-2	e-3	e-4	e-5	e-6	e-7
10 2p 1	1	1.9	20 1.E-06	3.E-06	4.4E-01	1.6	7.5E-08	3.5E-06	8.0E-06	3 3.14 105	71	75	79	83	87	94
	2	4.9	36 2.E-06	8.E-06	2.5E-01	1.6	3.8E-07	3.2E-06	1.3E-05		73	77	79	83	86	97
	3	4.9	36 4.E-07	6.E-06	6.3E-02	2.6	1.6E-07	1.2E-06	1.8E-05		73	77	79	83	87	97
	4	5.1	37 1.E-06	7.E-06	1.4E-01	1.6	7.2E-07	2.0E-06	1.5E-05		71	75	79	83	87	99
	5	4.6	34 5.E-06	4.E-05	1.3E-01	4.4	2.4E-06	2.2E-06	1.7E-05		71	75	79	83	86	101
	6	1.6	18 5.E-06	3.E-05	1.8E-01	1.7	1.1E-06	8.4E-06	4.6E-05		69	73	77	81	98	104
	7	1.4	17 4.E-06	2.E-05	2.0E-01	1.7	2.6E-06	9.7E-06	4.9E-05		69	73	77	80	99	*
	8	11.1	83 7.E-09	3.E-04	2.7E-05	4.6	9.0E-09	4.3E-06	1.6E-01		69	73	79	89	*	*
	9	4.6	34 1.E-05	3.E-06	3.9E+00	1.6	2.2E-06	3.4E-05	8.6E-06		71	75	79	81	85	92
	10	4.9	36 5.E-06	2.E-06	2.3E+00	1.7	2.2E-06	8.3E-07	3.7E-07		73	77	81	83	85	89
	11	4.6	34 2.E-06	3.E-06	6.8E-01	1.6	3.0E-07	6.4E-06	9.5E-06		71	75	79	83	85	92
	12	5.3	38 1.E-06	3.E-06	4.5E-01	1.7	1.5E-06	1.0E-06	2.2E-06		73	77	79	83	85	90
	13	4.2	32 2.E-06	4.E-06	4.8E-01	1.6	1.1E-06	5.8E-06	1.2E-05		69	73	78	82	86	93
	51	4.2	32 3.E-05	4.E-05	6.3E-01	4.6	7.1E-06	6.3E-06	1.0E-05		71	75	79	83	97	103
	52	4.9	36 8.E-06	5.E-05	1.5E-01	4.4	2.5E-06	1.6E-06	1.1E-05		69	73	77	81	92	104
	53	4.6	34 5.E-06	4.E-05	1.3E-01	4.4	1.7E-06	7.6E-07	5.9E-06		71	75	79	83	91	103
	54	1.9	20 4.E-06	2.E-05	1.9E-01	2.3	4.4E-07	4.4E-06	2.3E-05		69	73	77	81	95	104
	55	4.9	36 1.E-05	4.E-05	3.1E-01	5.4	4.1E-06	1.3E-06	4.3E-06		71	75	79	81	96	104
	56	1.9	20 1.E-05	4.E-05	2.2E-01	2.3	2.4E-06	6.2E-06	2.8E-05		71	75	79	81	99	105
	57	15.7	106 5.E-06	5.E-05	1.0E-01	1.9	3.3E-08	2.2E-04	2.1E-03		71	75	77	92	*	*
	58	10.9	82 6.E-06	7.E-05	8.1E-02	1.9	1.0E-06	1.9E-04	2.4E-03		69	73	77	82	105	105
	59	10.9	82 4.E-06	5.E-05	9.0E-02	1.7	5.5E-07	2.1E-04	2.3E-03		71	75	79	85	102	*

Channel	sol		Max. Error		Wfn. Max.	B.C.s	Exch. pot.		Chan.	#bfn	Coeff. conv					
# nme o	#	rx	nx Abs.	Norm.	Abs.	at	Abs.	Norm.	AM.	k	e-2	e-3	e-4	e-5	e-6	e-7
56 1s 1	1	1.4	18 2.E-04	3.E-04	4.7E-01	3.1	5.4E-06	7.5E-09	1.6E-08	2 4.33 110	72	74	82	102	*	*
	2	2.3	24 1.E-04	2.E-04	7.8E-01	2.4	1.0E-06	3.7E-09	4.8E-09		74	78	82	99	*	*
	3	8.4	81 5.E-05	2.E-04	2.7E-01	2.6	5.4E-07	9.3E-10	3.5E-09		74	78	86	95	*	*
	4	2.4	25 1.E-04	4.E-04	3.5E-01	1.8	2.9E-06	1.6E-09	4.5E-09		74	78	87	105	*	*
	5	2.6	26 2.E-04	1.E-04	1.3E+00	1.9	6.7E-06	9.6E-10	7.3E-10		72	76	81	90	109	*
	6	4.2	36 4.E-04	2.E-04	1.7E+00	1.0	2.4E-05	2.2E-09	1.3E-09		72	76	80	91	*	*
	7	4.2	36 7.E-04	3.E-04	2.5E+00	2.4	1.0E-05	6.9E-09	2.7E-09		72	76	80	86	*	*
	8	1.5	19 5.E-08	2.E-04	2.0E-04	1.6	1.1E-08	5.1E-08	2.6E-04		74	78	82	103	*	*
	9	2.3	24 1.E-03	2.E-04	5.4E+00	2.4	2.3E-05	5.6E-08	1.0E-08		74	80	88	106	*	*
	10	7.9	78 1.E-04	1.E-04	1.1E+00	2.1	2.3E-06	1.4E-09	1.3E-09		72	76	82	95	108	*
	53	4.5	38 7.E-05	6.E-05	1.1E+00	1.9	2.6E-06	4.3E-09	3.9E-09		74	78	82	88	*	*
	54	3.1	29 9.E-05	5.E-05	2.0E+00	3.3	1.2E-05	4.7E-09	2.4E-09		70	74	78	82	100	*
	55	4.4	37 4.E-04	8.E-05	4.8E+00	2.6	3.2E-05	1.2E-08	2.6E-09		68	74	78	82	*	*
	56	2.3	24 3.E-04	9.E-05	3.0E+00	1.8	3.7E-05	6.8E-09	2.2E-09		73	77	81	85	110	*
	57	1.4	18 9.E-05	7.E-05	1.3E+00	1.0	1.2E-05	3.8E-09	3.0E-09		72	76	80	84	107	*
	58	4.9	41 5.E-05	9.E-05	5.6E-01	1.6	2.2E-06	1.3E-09	2.3E-09		74	78	82	84	110	*
	59	7.9	78 5.E-05	3.E-05	1.6E+00	1.0	1.0E-05	3.3E-09	2.0E-09		70	76	80	82	96	108

- Channel sol
  # nme o #

  channel number, target name, open/closed status ($0 \Rightarrow$ closed, $1 \Rightarrow$ open) and solution number (from 1 to the total number of channels);

- ----- Max. Error -----
  rx nx Abs.   Norm.

  solution-channel maximum error, located at the point $x, \rho = $ rx, grid number nx, absolute magnitude Abs., normalised magnitude (absolute value $\div$ solution maximum value) Norm.;

- Wfn. Max.
  Abs.   at

  solution wavefunction maximum value, of magnitude Abs. and located at $x, \rho = $ at;

- B.C.s

  boundary condition absolute error, the difference between the solution at the boundary condition point and the boundary condition itself;

- Exch. pot.
  Abs.   Norm.

  exchange potential evaluated on the matching point (where the R-matrix is calculated), absolute value and normalised ($\div$ solution max.);

- Chan.
  AM.   k

  channel angular momentum and k-value (scattering momentum);

- #bfn

  number of basis functions in channel;

- ---- Coeff. conv -----
  e-2 e-3 e-4 e-5 e-6 e-7

  coefficient numbers, beyond which the coefficients are all less than 10^{-2}, 10^{-3}, 10^{-4}, 10^{-5}, 10^{-6} and 10^{-7} of the maximum value respectively.

The figure shows only selected lines from the output for a total angular momentum of $J = 2$ and a collision energy of 175 eV. Lines are for individual solutions for each channel separately; shown are a few of the lines from the solutions for channel 10 (one of the 2p excitation channels) and channel 56 (ground-state capture).

It can be seen that the solution errors are good in both channels, both in terms of absolute magnitude and relative to the wavefunction maximums; the boundary conditions are being obeyed (to be compared with the maximum solution value); and the exchange potentials are also very small on the boundary. There is one notable exception however: that of solution 8 in channel 10. The exchange potential here is quite significant with respect to the solution maximum, although small in magnitude. Channel 8, however, corresponds the 8s channel which, at 175 eV, is closed. The boundary condition in solution 8, when placed close to the outer boundary as in this case, forces an exponentially increasing solution in channel 8; channel 8 (not shown) is indeed found to reach its maximum value at the outer boundary. Since this is evidently unphysical and will be discarded when matching to the boundary conditions this solution may be neglected. It is important still, however, that the boundary condition is being obeyed in order to maintain linear independence between the solutions.

The coefficients are also seen to be well converged: to within 10^{-5} in all cases. Note the high momentum of 4.33 in the ground-state capture making it necessary for more basis functions in this channel. A few (5–10) more basis functions was sometimes found to be beneficial in the higher momentum channels in the direct partition also.

Shown in figure A.4 (p. 127) is a graphical depiction of some of the coefficients belonging to a 29-state calculation for $J = 1$, 175 eV. It can be seen from the plot that the coefficients are well behaved and well converged. In contrast, shown in figure A.5 (p. 128) are some of the coefficients for a 2-state calculation in which there is an inadequate total number of fitting mesh points. The same behaviour can also be observed if instead the distribution of points is inadequate. Care must be taken to avoid this situation, although with a little care and examination of the diagnostic output of the calculation it can be easily avoided.

Notes

[1]The principle of least privilege entails hiding certain data allocations from

certain parts of the program, only making them available to explicitly controlled areas of the code.

[2]Dynamic memory allocations are blocks of memory that are allocated explicitly within the code during run-time, as opposed to allocations that are made by the compiler. Memory allocated dynamically can vary in size from one execution to another and can be a function of input parameters or parameters determined by the program. Almost all of the memory allocated by a program such as this one is dynamic and it is of great importance to maintain the integrity of these allocations.

[3]Global memory allocations are those which are accessible from all parts of the program.

Figure A.4: Sample converged scattering wavefunction coefficients calculated using the minimum-norm method. The absolute values of the coefficients are plotted for the 1s–6s channels belonging to solution 1 of a 29-state calculation. The selected calculation is $J = 1$, 175 eV.
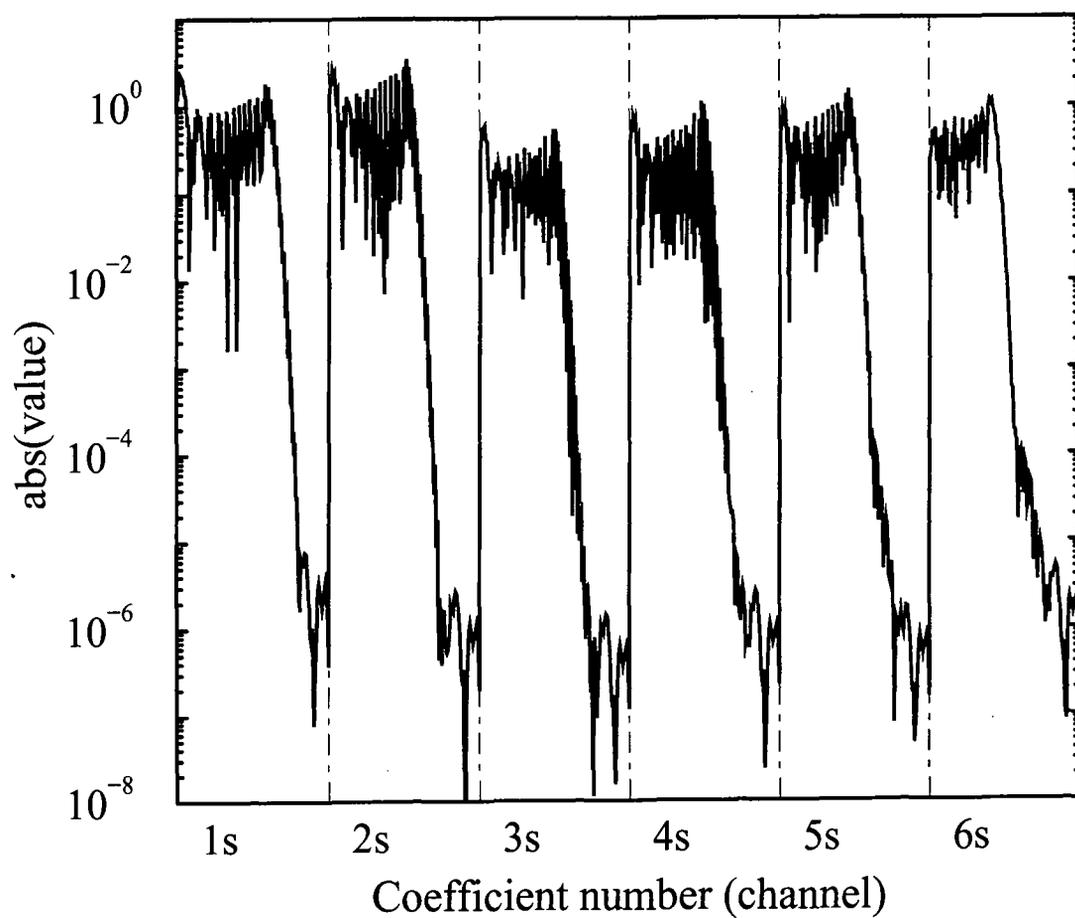
Figure A.5: Sample scattering wavefunction coefficients calculated using the minimum-norm method. The coefficients are evidently not well converged and there is something wrong. In fact in this case it is due to a lack of fitting mesh points, although similar behaviour would also be observed if there was an inadequate distribution of points. The absolute values of the coefficients are plotted for the 1s and Ps(1s) channels belonging to solution 1 of a 2-state calculation. The selected calculation is $J = 3$, 175 eV.
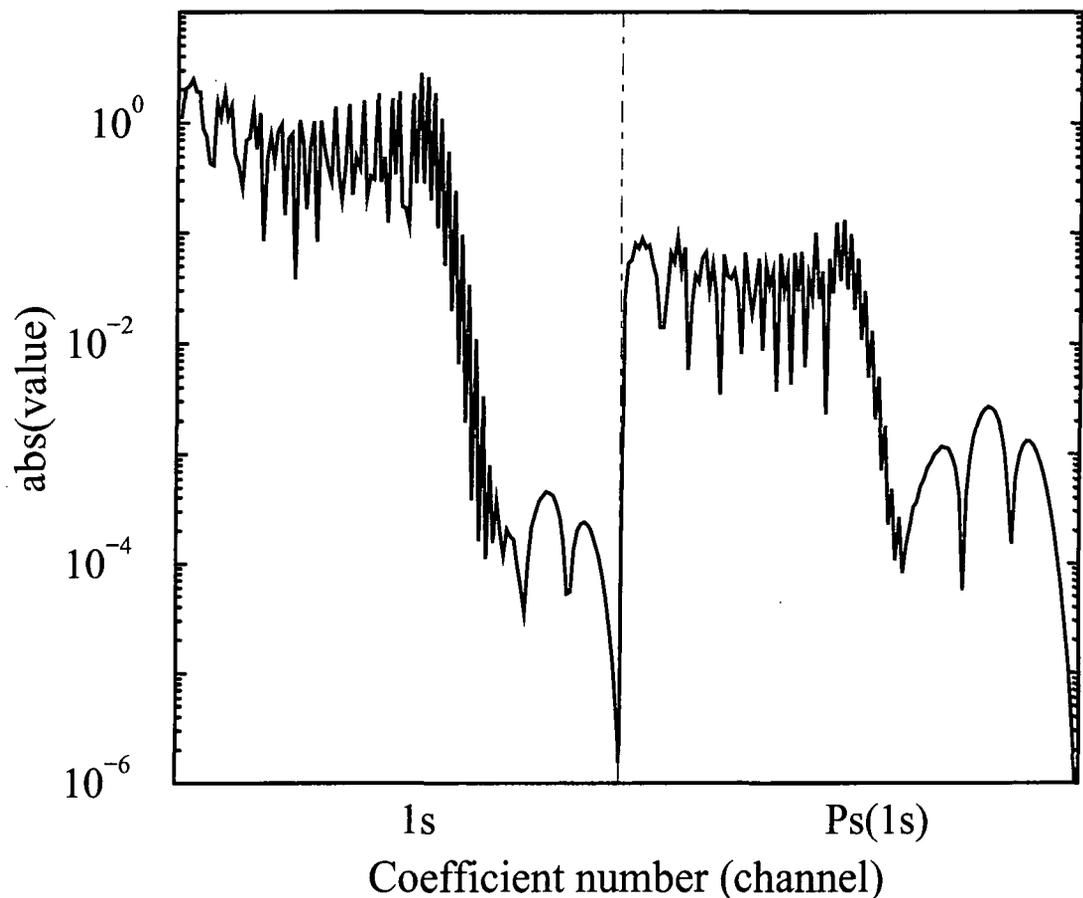
Appendix B

Development of a Parallel Version of the Close Coupling Code

Introduction

During the course of working with the least-squares/minimum-norm code it was decided that it would be beneficial to develop a parallel version of the code. In this appendix we discuss in some detail why this was felt to be necessary, how it was achieved and what effect it had on performance.

The motivation for extending the serial code to also be able to work in a parallel configuration arose from a number of issues:

1. the serial code was very computationally intensive and slow to generate results;

2. the least-squares code had been originally noted to be particularly suitable for parallelisation [2];

3. it was already running on a machine with parallel capabilities (in fact, a Silicon Graphics Origin 2000) and scope was spotted for being able to capitalise on the remaining 7 CPUs that were often available;[1]

4. for the largest close coupling sets the program was close to the memory limit of the current machine and so it was no longer possible to run separate copies

of the program concurrently (trivial parallelisation);

5. due to being so computationally intensive, larger basis set calculations would only be realistically tractable if it were able to utilise multiple processors, such as on a distributed memory massively parallel supercomputer;[2] and

6. in its serial form, due to the large memory consumption, it was limited to running mostly on shared memory machines only which typically can make much larger quantities of memory readily available for just one processor than can other machines.[3]

The plan was, originally, to eventually port the code to a distributed memory massively parallel machine, although subsequently this was found not to be necessary. The possibility of being able to run the program on a network cluster was also considered, if it was possible to design the parallelisation to be flexible enough, although this was certainly not a priority.

An algorithm was developed that would both satisfy the above requirements and be relatively quick to implement. The language that was chosen (the original code was written in FORTRAN 90) was the Message Passing Interface (MPI), in fact MPI-2, details of which may be found on the World Wide Web and in the standards document [204]. The reasons for this choice were its

- availability on a wide range of platforms with a good range of software (debugging and profiling) support;

- suitability to a wide range of different types of architecture, in particular the distributed and shared memory machines that were to be used;

- availability for C, C++ and FORTRAN (77 and 90) bindings; and

- explicit control over message passing and process control (the latter is only available in MPI-2 however).

The first two points are important for satisfying portability, although the algorithm must of course still be designed in such a way as to suit the various architectures.

Figure B.1: Diagram depicting the basic architecture of the Origin 2000 machine.
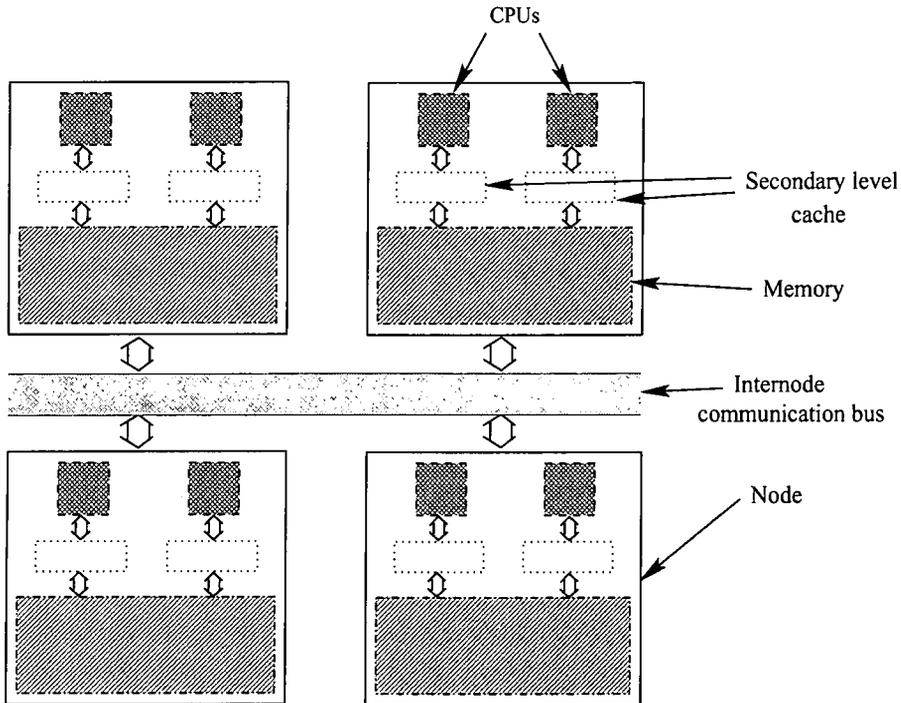
Other possibilities included: Parallel Virtual Machine (PVM), which is now obsolete; and SHared MEMory (shmem), which does not offer explicit control over message passing and is not portable.

Having discussed the reasons for undertaking a conversion of the code into parallel form we now discuss in more detail how this was achieved and what effect it had.

Implementation

Before discussing the algorithm it is appropriate to discuss the architecture of the target platform: the SGI Origin 2000.

The Origin 2000 is an 8 processor machine with, in this case, a total of 4GB of memory. Although to the user the machine is a shared memory machine these processors and memory are in fact arranged as 4 nodes each comprising of 2 processors, 1GB of memory and 8MB of secondary level cache[4] (figure B.1). The nodes are interconnected by a fast data bus; data allocation and transfer between

Figure B.2: Depiction of the partitioning of the M-matrix, $M_{ij\lambda}(r_q)$; each segment is labelled by the channel index i.
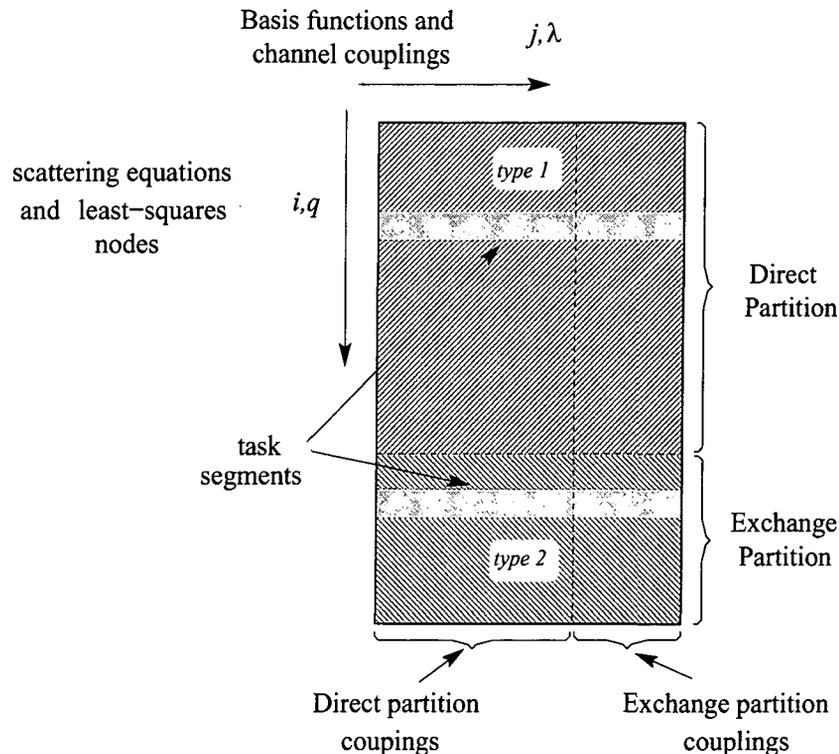
nodes is handled by the operating system, hence the system is a shared memory one, although memory accesses across this bus are significantly slower than those confined to a single node.

After consideration of the criteria discussed above and, in particular, the architecture of the Origin machine a master-slave configuration was adopted for the parallelisation since this was easy to code. The whole code was not parallelised since this was not deemed necessary; instead, only construction of the M- and F-matrices (equations 2.48 and 2.51a) was parallelised.

The parallelisation was achieved by a partitioning of the M-matrix into segments each corresponding to a particular channel i (equation 2.48); this is depicted in figure B.2. The M-matrix is indexed by j, λ and i, q where, remember, q indexes the quadrature and λ indexes the basis functions $\phi_\lambda^j(r_q)$ for couplings to a particular channel j. Since each task corresponds to a particular scattering equation there are typically up to around 60 tasks in the task pool.

It is in fact more convenient to divide the tasks into two task pools containing tasks of type 1 and type 2 respectively. The reason for this is that there is certain data common to tasks for which channel i belongs to the direct partition and those which belong to the exchange partition; these are what are labelled types 1 and 2. Slaves are initialised to either type 1 or type 2 at the beginning of execution, saving a certain amount of time in the initialisation for each task.[5] During type initialisation the slaves thus receive the basis functions and with each task initialisation they need only receive the relevant potential couplings.

The slaves also construct a segment of the F-matrix, $F_{j\lambda,j'\lambda'}$ (equation 2.51a), during each task which is returned to the master processes for collation upon completion of the task. This corresponds to sequence of dot products, one for each pair j, λ and j', λ'. The job of the master is to sum the contributions to the F-matrix from each task which, for speed purposes, is done by buffering the data returned from each task, thus allowing the data to be transferred each time in a single burst.

Now to the actual algorithm. Shown in figure B.3 on page 138 is a flow diagram depicting the modification to the serial code (figure A.1) required to construct the master process; the complete slave process is depicted in figure B.4, page 139.

All processes begin by initialising their respective MPI environments and memory managers; the master process then proceeds with the first part of the program, reading in program parameters and any precomputed data stored on disk followed by any preliminary calculations, such as angular couplings and generating the grids for discretisation of the equations. When the M- and F-matrix calculation is reached the task pools are initialised and the slaves are partitioned and initialised into type 1's and type 2's; their identities and status are also logged by the master and buffer memory is allocated. Communication channels were then opened by the master, one for each slave. These are non-blocking receive[6] calls which provide a mechanism by which the slaves can contact the master for data. The tasks are then distributed to the slaves and executed one-by-one. When both task pools are exhausted and all results have been received the master then proceeds with the rest of the program. In practice the master process also executes some tasks;[7] these tasks were chosen as the ones which involved the most data (type 2s) so as

to minimise duplication in memory.[8] Finally, all memory allocations were checked for integrity (see appendix A) and temporary ones discarded.

Observed Performance and Discussion

The impact on performance when run on the Origin machine was startling: there was not only a considerable increase in performance when run on anything from 2 to 8 processors but the performance increase was found to be superscalar![9] The increase in execution speed when operating on 6 CPUs was found to be around 8-fold: a superscalar factor of around 50%.[10] At first sight this is indeed a surprising result; how can this be possible?

Although as yet unverified[11] it is strongly suspected that the reason lies in the physical organisation of the memory within the Origin machine (figure B.1). As explained previously, memory is distributed physically between the nodes; memory access between nodes is much slower than when confined to within a single node and involves a large latency period. It is postulated that the increase in performance arises from the essentially explicit partitioning of data between processors within the program logic which assists the operating system in deciding upon the physical location of data during execution. The serial code, for the largest coupling cases considered, occupied considerably more memory than was available on one node alone and so would be spread across multiple nodes. This could clearly slow down execution in some cases.

In addition to the above there could possibly also be an increase in performance from the redesign of the algorithm when performing the dot products for the F-matrix elements. Instead of acting on data segments spanning all channels the dot products only acted on segments which were each only one channel in length and hence of dimension around 150 to 200. There is a possibility that the processors were able to make better use of cache memory with the smaller data segments and hence there were fewer cache misses than with the serial algorithm. The logic of cache operations is a complex subject and is clearly processor dependent; however, it is unlikely that the superscalar increase could all be attributed to a higher cache

hit rate.

One lesson is clear from the above findings: careful design of a program algorithm, taking into account the architecture of the machine to be used, is highly beneficial; use of all 8 processors with the above parallel code gave around an order of magnitude increase in program performance from only a modest amount of reprogramming. The subject of machine architecture and parallel programming algorithms is, however, a vast and complex one and will not be discussed any further here.

Notes

[1]The number of CPUs that were available of course depended on the usage of the machine by other users. A dynamic load-balancing scheme was planned which could be incorporated into the designed algorithm at a later stage. The modified code would have made use of the process-spawning capabilities of MPI, only made available in MPI-2, and could have controlled the number of threads (processes) running in order to utilise all available processors; it would have been dynamic in that the number of processes could have varied during program execution. In fact, with the particular machine being used, this was never found to be necessary and so was never carried out.

[2]A distributed memory machine is one in which each processor has its own memory which is physically separate to the rest of the machine apart from network-style communication pathways between processors; a processor with its memory and associated circuitry is often referred to as a node. A massively parallel machine is one composed of a great many nodes interconnected by a very fast communication backbone; the exact architecture can vary.

[3]A shared memory machine is a machine with multiple processors which all share the same memory resources. In fact what is often the case is that individual processors, or small numbers of processors (2 or 4), share the same memory on an equal footing (called nodes) but are given access to the memory belonging to other processors. This access is handled by the operating system and is transparent to

the user who views the total system memory as being available to each processor on an equal footing, analogous to virtual memory. The SGI Origin is an example of such a machine which will be discussed in more detail later.

[4]Cache is memory that resides between the processor and main memory (or other device, such as a hard disk) and stores (buffers) frequently accessed data from memory; it is much faster than main memory, operating at a speed closer to that of the processor, and helps to remove processor-memory bottlenecks. The processors have a small quantity (32kB) of primary level cache incorporated within them (faster than secondary level cache, but generally smaller).

[5]The type of a slave may change however during program execution if one of the task pools becomes exhausted before the other.

[6]Send and receive data operations in MPI can be classified into blocking and non-blocking types. Blocking operations are ones in which the library routine does not return control of execution to the calling code until the operation is complete; non-blocking calls return control immediately after the operation has been set up. The advantage of non-blocking operations is generally that program execution is not held up by slow communications; the programmer does, however, have to be aware that the operation may not, and probably will not, be completed for some time and so the data involved will not be immediately available. In this instance in the program non-blocking receives are used as a means by which the slaves can contact the master at any time, rather like a telecommunications pager.

[7]It should be noted that the fork of execution depicted in figure B.3 was achieved by program logic, with control over granularity chosen carefully, and not by the spawning of a concurrent process.

[8]The observant reader may question as to why data is being duplicated on a shared memory machine. The answer is that the program was originally destined for a distributed memory machine eventually. Also, as we shall see in the next section, this actually had quite a beneficial impact on speed on the shared memory machine.

[9]When the number of processors which a program is run on is increased from 1 to N one would expect an increase in execution speed of $P < N$ times. A program

which acheives an increase of $P > N$ is said to be superscalar.

[10]The increase in performance was a little difficult to ascertain with any great degree of precision since it varied depending on machine load from other users.

[11]The performance of a parallel code can be monitored using a piece of software called a profiler. The reasons for the superscalar increase were, unfortunately, never investigated this way due to time constraints.

Figure B.3: Block diagram depicting the order of execution of the master process.
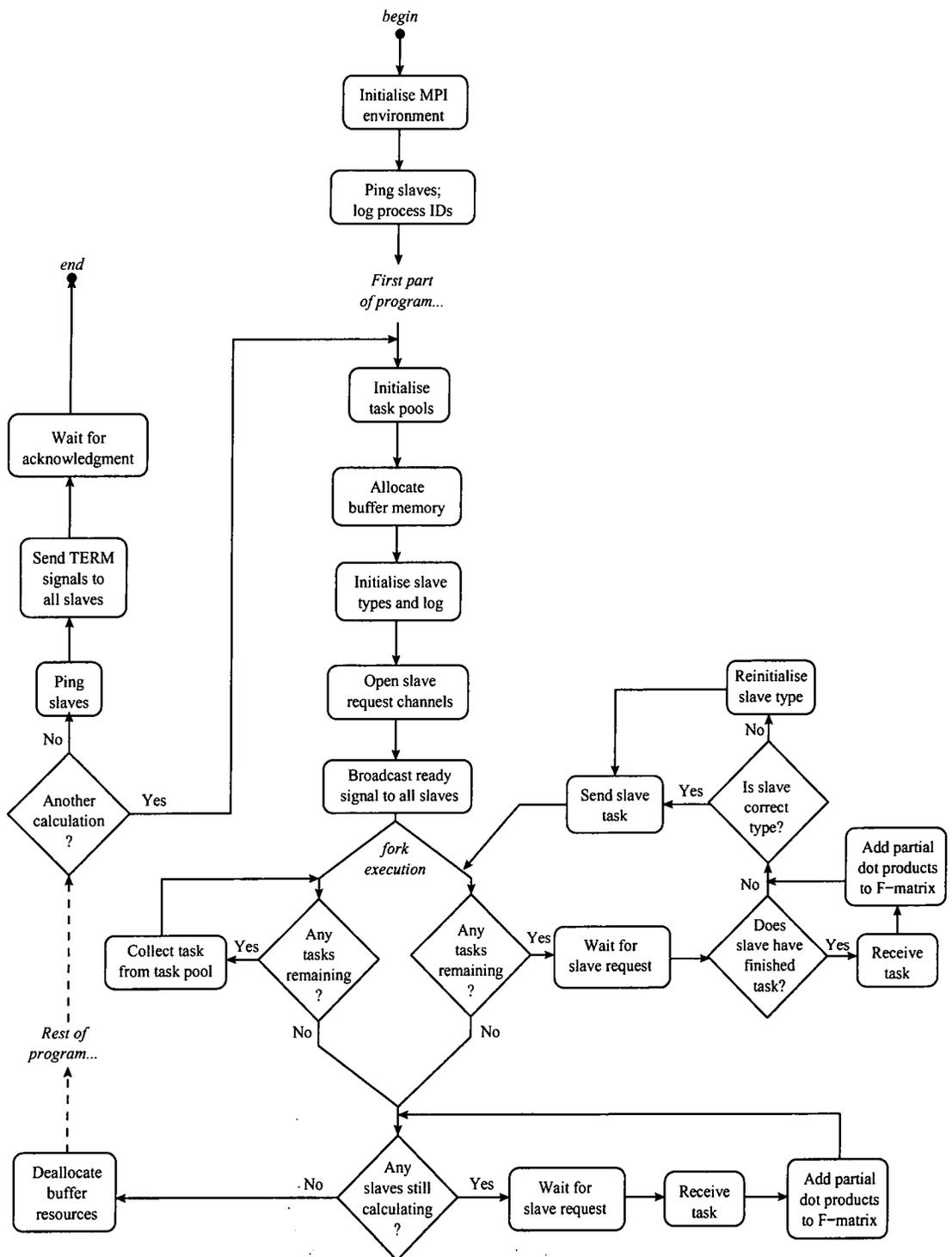
Figure B.4: Block diagram depicting the order of execution of the slave processes.
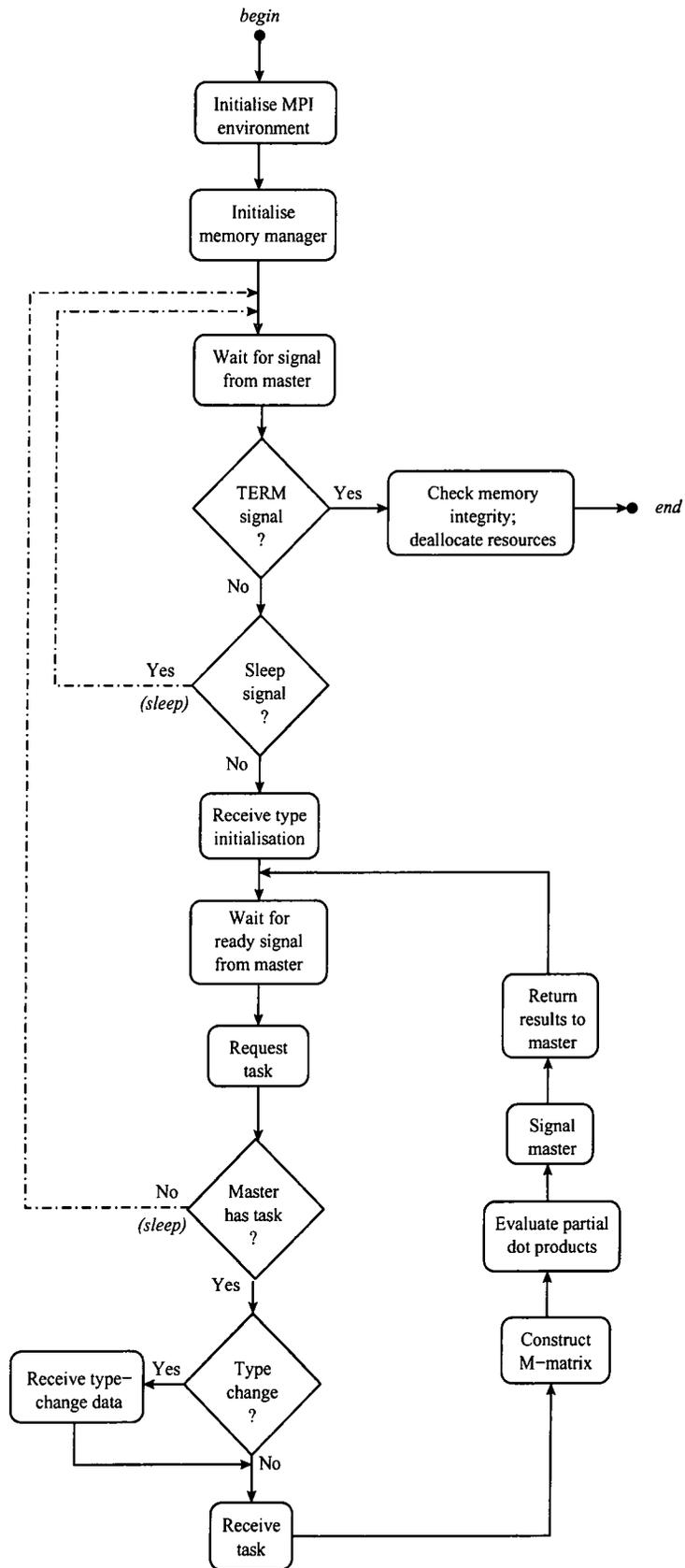
Appendix C

Evaluation of Close Coupling Matrix Elements

In this appendix we evaluate some of the matrix elements of the close coupling equations: the exchange potentials M_3 and M_4 and the direct potentials $V_{\alpha\beta}$ and $W_{\gamma\delta}$.

Matrix element M₃

Beginning from

$$M_3 \equiv \langle \overline{\phi} | H - E | \Psi_X^{JM} \rangle$$
$$= \sum_{\gamma L_\gamma} \int_0^\infty \rho \, d\rho \, K_{\alpha\gamma}(x, \rho) g_{\gamma L_\gamma}^J(\rho). \tag{C.1}$$

Writing this out in full

$$\sum_{m_\alpha m_\alpha'} \int d\hat{x} \int dr R_{n_\alpha l_\alpha}(r) \langle L_\alpha l_\alpha; m_\alpha' m_\alpha | JM \rangle Y_{L_\alpha m_\alpha'}^*(\hat{x}) Y_{l_\alpha m_\alpha}^*(\hat{x}) \times$$

$$\left[-\frac{1}{4}\nabla_\rho^2 - \nabla_R^2 - \frac{1}{R} + \frac{Z}{x} - \frac{Z}{r} - E \right] \times$$

$$\sum_{\substack{\gamma L_\gamma \\ m_\gamma m_\gamma'}} \frac{1}{\rho} g_{\gamma L_\gamma}^J(\rho) S_{n_\gamma l_\gamma}(R) \langle L_\gamma l_\gamma; m_\gamma' m_\gamma | JM \rangle Y_{L_\gamma m_\gamma'}(\hat{\rho}) Y_{l_\gamma m_\gamma}(\hat{R}), \tag{C.2}$$

where the Hamiltonian has been written out in full. Using the relation $d\boldsymbol{r} = 8d\boldsymbol{\rho}$, where $\hat{x}$ has been held constant, we can write

$$K_{\alpha\gamma}(x,\rho) = 8 \sum \langle L_\alpha l_\alpha; m'_\alpha m_\alpha | JM \rangle \langle L_\gamma l_\gamma; m'_\gamma m_\gamma | JM \rangle \int d\hat{x} \int d\hat{\rho}$$

$$R_{n_\alpha l_\alpha}(r) Y^*_{L_\alpha m'_\alpha}(\hat{x}) Y^*_{l_\alpha m_\alpha}(\hat{x}) \times$$

$$\left[-\frac{1}{4}\nabla^2_\rho - \nabla^2_R - \frac{1}{R} + \frac{Z}{x} - \frac{Z}{r} - E \right] \times$$

$$S_{n_\gamma l_\gamma}(R) Y_{L_\gamma m'_\gamma}(\hat{\rho}) Y_{l_\gamma m_\gamma}(\hat{R}). \quad \text{(C.3)}$$

We firstly use the relations

$$-\frac{1}{4}\nabla^2_\rho = -\frac{1}{4}\left[\frac{d^2}{d\rho^2} - \frac{L_\gamma(L_\gamma+1)}{\rho^2} + k'^2_\gamma \right] + \frac{1}{4} k'^2_\gamma \quad \text{(C.4a)}$$

$$-\nabla^2_R = -\frac{d^2}{dR^2} + \frac{l_\gamma(l_\gamma+1)}{R^2} \quad \text{(C.4b)}$$

and substitute

$$K_{\alpha\gamma}(x,\rho) \equiv K^{(1)}_{\alpha\gamma}(x,\rho) + K^{(2)}_{\alpha\gamma}(x,\rho) \cdot \left(-\frac{1}{4} \right) \left[\frac{d^2}{d\rho^2} - \frac{L_\gamma(L_\gamma+1)}{\rho^2} + k'^2_\gamma \right]. \quad \text{(C.5)}$$

We now have a product of four spherical harmonics to be evaluated, two of which require a change of variable. This may be accomplished by use of [205]

$$\mathcal{Y}^m_l(\boldsymbol{r}_A) = (-)^{l+m} \sum_{\lambda,\mu} \mathcal{Y}^\mu_\lambda(\boldsymbol{r}_B) \mathcal{Y}^{m-\mu}_{l-\mu}(\boldsymbol{R})$$

$$\begin{pmatrix} l & \lambda & l-\lambda \\ -m & \mu & m-\mu \end{pmatrix} \left[\frac{4\pi \hat{l}.\hat{l}!}{[2(l-\lambda)+1]!\hat{\lambda}!} \right]^{1/2}, \quad \text{(C.6)}$$

where $\boldsymbol{R} = \boldsymbol{r}_A - \boldsymbol{r}_B$,

$$\hat{l} \equiv 2l+1, \quad \text{(C.7)}$$

$$\begin{pmatrix} l & \lambda & l-\lambda \\ -m & \mu & m-\mu \end{pmatrix} \quad \text{(C.8)}$$

is a Wigner 3j symbol related to a Clebsch-Gordan coefficient by the relation

$$\begin{pmatrix} a & b & c \\ \alpha & \beta & \gamma \end{pmatrix} = (-)^{a-b-\gamma} \hat{c}^{-1/2} \langle ab; \alpha\beta | c - \gamma \rangle. \quad \text{(C.9)}$$

and

$$\mathcal{Y}_l^m(\boldsymbol{r}) \equiv r^l Y_{lm}(\hat{r}) \tag{C.10}$$

is termed a *solid spherical harmonic*. This leads to the relations

$$Y_{l_\alpha m_\alpha}^*(\hat{r}) = (-)^{l_\alpha + m_\alpha} \sum_{\substack{a,b \\ m_a, m_b}} \delta_{l_\alpha, a+b} \left[\frac{4\pi \hat{l}_\alpha!}{\hat{a}! \hat{b}!} \right] (2\rho)^a x^b \times$$

$$Y_{a m_a}(\hat{\rho}) Y_{b m_b}(\hat{x}) \langle ab; m_a m_b | l_\alpha - m_\alpha \rangle r^{-l_\alpha}$$

and

$$Y_{l_\gamma m_\gamma}(\hat{R}) = (-)^{l_\gamma} \sum_{\substack{c,d \\ m_c, m_d}} \delta_{l_\gamma, c+d} \left[\frac{4\pi \hat{l}_\gamma!}{\hat{c}! \hat{d}!} \right] (2\rho)^c (2x)^d \times$$

$$Y_{c m_c}(\hat{\rho}) Y_{d m_d}(\hat{x}) \langle cd; m_c m_d | l_\gamma m_\gamma \rangle R^{-l_\gamma}.$$

The products of spherical harmonics may now be evaluated using

$$Y_{l_1 m_1}(\hat{r}) Y_{l_2 m_2}(\hat{r}) = \sum_{lm} \left(\frac{\hat{l}_1 \hat{l}_2}{4\pi \hat{l}} \right)^{1/2} \langle l_1 l_2; m_1 m_2 | lm \rangle \langle l_1 l_2; 00 | l0 \rangle Y_{lm}(\hat{r}) \tag{C.12}$$

so that

$$I_{\hat{r}} \equiv \int d\hat{r} \, Y_{l_1 m_1}(\hat{r}) Y_{l_2 m_2}(\hat{r}) Y_{l_3 m_3}(\hat{r}) Y_{l_4 m_4}(\hat{r})$$

$$= \sum_{lm} \frac{(\hat{l}_1 \hat{l}_2 \hat{l}_3 \hat{l}_4)^{\frac{1}{2}}}{4\pi \hat{l}} \langle l_1 l_2; m_1 m_2 | lm \rangle \langle l_3 l_4; m_3 m_4 | lm \rangle$$

$$\langle l_1 l_2; 00 | l0 \rangle \langle l_3 l_4; 00 | l0 \rangle (-)^m. \tag{C.13}$$

Now, defining

$$O_{\alpha\gamma}^{(1)} \equiv r^{-l_\alpha} R_{n_\alpha l_\alpha}(r) R^{-1} \times$$

$$\left[-\frac{d^2}{dR^2} + \frac{l_\gamma(l_\gamma + 1)}{R^2} + V(x, \rho) - \eta_\gamma \right] R S_{n_\gamma l_\gamma}(R) R^{-l_\gamma}$$

$$= \sum_{\lambda=0}^{\infty} k_{\lambda, \alpha\gamma}^{(1)}(x, \rho) P_\lambda(\widehat{x\rho}) \tag{C.14a}$$

$$= 4\pi \sum_{\lambda, m_\lambda} \hat{\lambda}^{-1} k_{\lambda, \alpha\gamma}^{(1)}(x, \rho) Y_{\lambda m_\lambda}^*(\hat{x}) Y_{\lambda m_\lambda}(\hat{\rho})$$

and

$$O^{(2)}_{\alpha\gamma} \equiv r^{-l_\alpha} R_{n_\alpha l_\alpha}(r) S_{n_\gamma l_\gamma}(R) R^{-l_\gamma}$$

$$= \sum_{\lambda=0}^{\infty} k^{(2)}_{\lambda,\alpha\gamma}(x,\rho) P_\lambda(\widehat{x\rho}) \tag{C.14b}$$

$$= 4\pi \sum_{\lambda,m_\lambda} \hat{\lambda}^{-1} k^{(2)}_{\lambda,\alpha\gamma}(x,\rho) Y^*_{\lambda m_\lambda}(\hat{x}) Y_{\lambda m_\lambda}(\hat{\rho}),$$

where

$$V(x,\rho) = \overline{V}(\rho,x) = -R^{-1} + Zx^{-1} - Zr^{-1}, \tag{C.15}$$

we have

$$k^{(i)}_{\lambda,\alpha\gamma} = \frac{\hat{\lambda}}{2} \int_{-1}^{+1} \mathrm{d}(\widehat{x\rho}) P_\lambda(\widehat{x\rho}) O^{(i)}_{\alpha\gamma}. \tag{C.16}$$

We note that for real targets (C.14a) is much simplified since

$$\left[-\frac{\mathrm{d}^2}{\mathrm{d}R^2} + \frac{l_\gamma(l_\gamma+1)}{R^2} - \frac{1}{R} - \eta_\gamma \right] R S_{n_\gamma l_\gamma}(R) = 0 \tag{C.17}$$

Now, collecting together all the above results, we arrive at

$$K^{(i)}_{\alpha\gamma}(x,\rho) = 8(-)^{L_\alpha+L_\gamma} (\hat{L}_\alpha \hat{L}_\gamma)^{1/2} 2^{a+l_\gamma} \times$$

$$\sum_{a,b} \delta_{l_\alpha,a+b} \left[\frac{\hat{l}_\alpha!}{(2a)!(2b)!} \right] \sum_{c,d} \delta_{l_\gamma,c+d} \left[\frac{\hat{l}_\gamma!}{(2c)!(2d)!} \right] \times$$

$$\rho^{a+c} x^{b+d} \sum_\lambda k^{(i)}_{\lambda,\alpha\gamma}(x,\rho) \times$$

$$\sum_j \begin{pmatrix} b & d & j \\ 0 & 0 & 0 \end{pmatrix} \begin{pmatrix} L_\alpha & \lambda & j \\ 0 & 0 & 0 \end{pmatrix} \sum_k \begin{pmatrix} a & c & k \\ 0 & 0 & 0 \end{pmatrix} \begin{pmatrix} L_\gamma & \lambda & k \\ 0 & 0 & 0 \end{pmatrix} \mathcal{M} \tag{C.18}$$

where

$$\mathcal{M} = \sum (-)^{m_\alpha+m_k} \langle L_\alpha l_\alpha; m'_\alpha m_\alpha | JM \rangle \langle L_\gamma l_\gamma; m'_\gamma m_\gamma | JM \rangle$$

$$\langle ab; m_a m_b | l_\alpha - m_\alpha \rangle \langle cd; m_c m_d | l_\gamma m_\gamma \rangle \langle L_\alpha \lambda; m'_\alpha m_\lambda | j m_j \rangle$$

$$\langle bd; m_b m_d | j m_j \rangle \langle L_\gamma \lambda; m'_\gamma m_\lambda | k - m_k \rangle \langle ac; m_a m_c | k m_k \rangle. \tag{C.19}$$

Note that some Clebsch-Gordan coefficients have been converted to 3j symbols by use of the relation (C.9).

What remains to be evaluated is now the summation of Clebsch-Gordan coefficients $\mathcal{M}$. This is convenient to evaluate by the use of graphical methods, described in for example Brink and Satchler [188] and Zare [187]. In what follows we adopt the definitions of Zare which, the reader should note, differ slightly from those of Brink and Satchler in places. References to the original work are given in [187, 188]. In what follows, a plus sign denotes a counterclockwise node and a minus sign denotes a clockwise node.

Using the definition

$$\langle j_1 j_2; m_1 m_2 | j_3 m_3 \rangle = \hat{j}_3^{1/2}$$

$$\tag{C.20}$$

and the fact that

$$\langle ab; m_a m_b | l_\alpha - m_\alpha \rangle = \hat{l}_\alpha^{1/2}$$

$$\tag{C.21}$$

$$= (-)^{l_\alpha + m_\alpha} \hat{l}_\alpha^{1/2}$$

$$\tag{C.22}$$

we may write immediately

$$\mathcal{M} = (-)^{\phi_1} \hat{J} (\hat{l}_\alpha \hat{l}_\gamma)^{1/2} \hat{j} \hat{k} \times$$

$$(C.23)$$
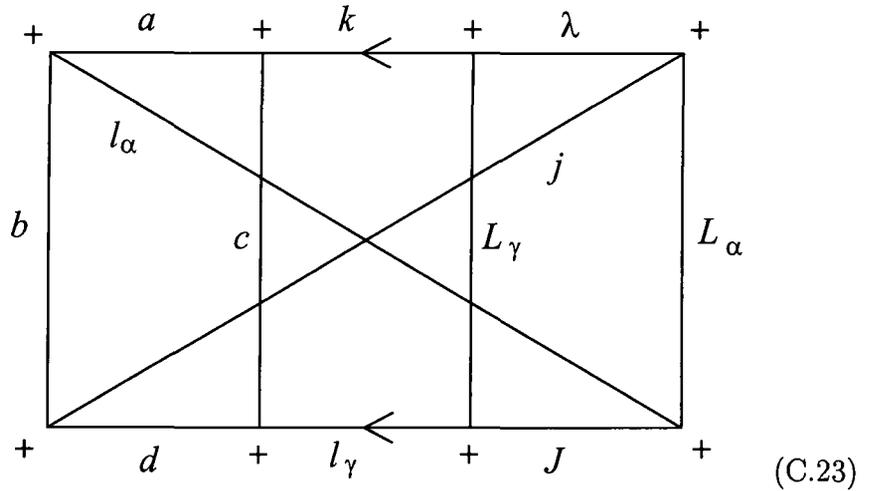
where the phase $\phi_1 = l_\alpha + k$. Rearranging the nodes and adding/cancelling arrows

$$\mathcal{M} = (-)^{\phi_1} \hat{J} (\hat{l}_\alpha \hat{l}_\gamma)^{1/2} \hat{j} \hat{k} \times$$

$$(C.24)$$
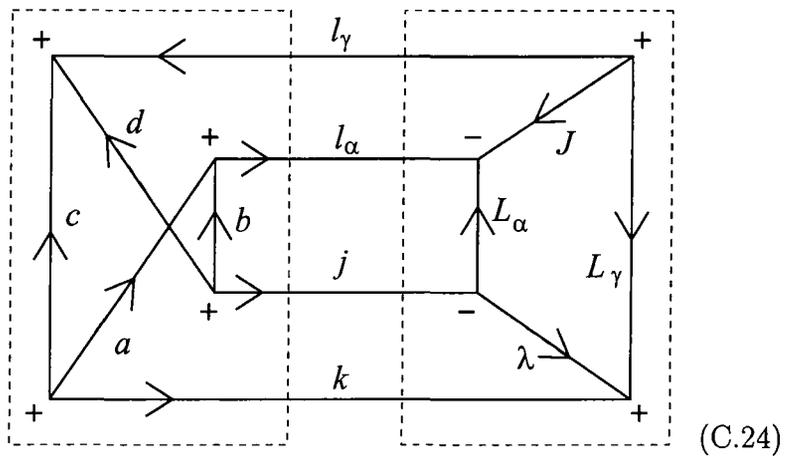
We note at this point that the diagram has been put in *normal form*: every internal line, a line that is connected at both ends, has exactly one arrow on it. The importance of this form is that any diagrams arising from coupling of angular momenta can be put into this form. The explicit demonstration that the diagram can be put into normal form thus serves as a useful check of the manipulation so far. Using the theorem
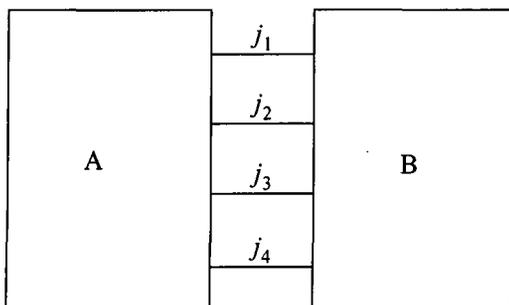
$$(C.25)$$

where A is a *closed block* (it has no external lines) and can be put into normal form, this may be written instead as the product of two diagrams

$$\mathcal{M} = (-)^{\phi'} \hat{J} (\hat{l}_\alpha \hat{l}_\gamma)^{1/2} \hat{j} \hat{k} \sum_y \hat{y} \times$$

$$(C.26)$$

where the new quantum number y, with corresponding magnetic quantum number m_y, has been introduced. The first of these terms is

$$(C.27)$$

Notice that this closed diagram (no external lines) is in normal form. Because of this it can be immediately interpreted as a $3nj$ symbol. In this case it can be shown

to be equal to the 9j symbol

$$\begin{Bmatrix} l_\alpha & l_\gamma & y \\ b & d & j \\ a & c & k \end{Bmatrix}$$

(C.28)

multiplyed by an additional phase factor $(-)^{\phi_2}$ arising from the rearrangement of arrows and node orientations, where

$$\phi_2 = y + l_\alpha + l_\gamma$$

(C.29)

(note that all quantum numbers are integers and hence $(-)^{2p} = 1$ for any quantum number p). The second term in (C.26) transforms to
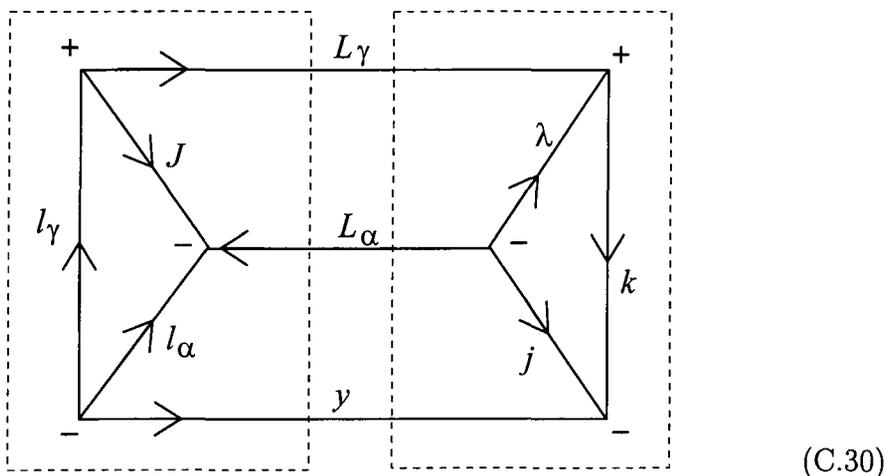
(C.30)

By application of the theorem
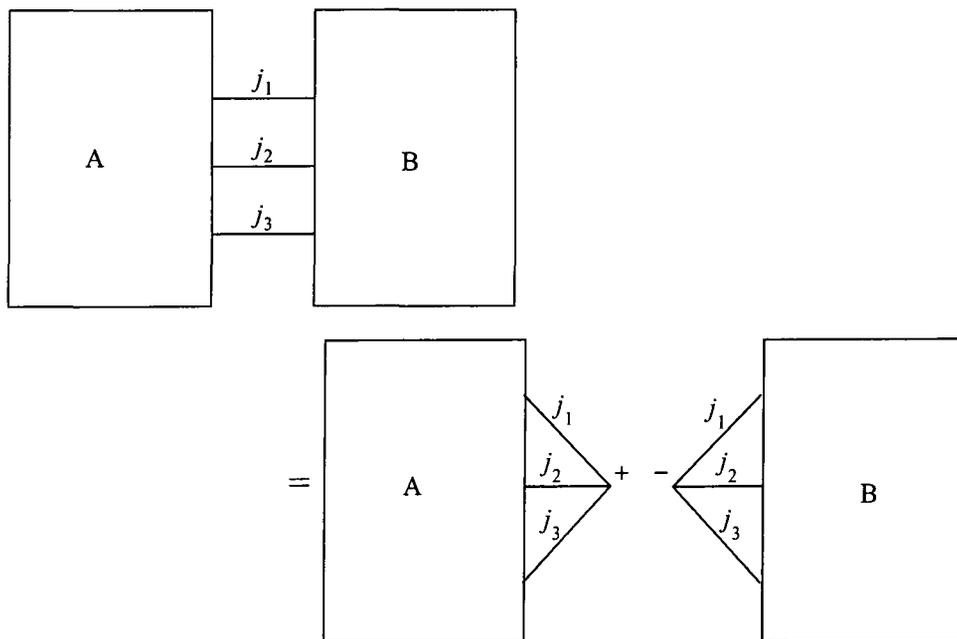
(C.31)

where once again A is a closed diagram in normal form, this transforms to the product

$$(C.32)$$

Once again these two diagrams, which can easily be shown to be put equivalent to diagrams in normal form, may be identified with $3nj$ symbols: in this case the $6j$ symbols

$$\begin{Bmatrix} y & L_\alpha & L_\gamma \\ J & l_\gamma & l_\alpha \end{Bmatrix} \tag{C.33a}$$

$$\begin{Bmatrix} y & k & j \\ \lambda & L_\alpha & L_\gamma \end{Bmatrix} \tag{C.33b}$$

respectively, multiplied by phase factors $(-)^{\phi_3}$ and $(-)^{\phi_4}$, where

$$\phi_3 = y + J + L_\alpha + l_\gamma \tag{C.34a}$$

$$\phi_4 = y + k + L_\gamma \tag{C.34b}$$

Collecting together phases:

$$\phi = \phi_1 + \phi_2 + \phi_3 + \phi_4$$
$$= J + L_\alpha + L_\gamma + \lambda \tag{C.35}$$

we have the final result for $\mathcal{M}$:

$$\mathcal{M} = (-)^{J+L_\alpha+L_\gamma+\lambda} \hat{j}\hat{k}(\hat{l}_\alpha\hat{l}_\gamma)^{1/2} \sum_y \hat{y}$$

$$\times \begin{Bmatrix} l_\alpha & l_\gamma & y \\ b & d & j \\ a & c & k \end{Bmatrix} \begin{Bmatrix} y & L_\alpha & L_\gamma \\ J & l_\gamma & l_\alpha \end{Bmatrix} \begin{Bmatrix} y & k & j \\ \lambda & L_\alpha & L_\gamma \end{Bmatrix}. \tag{C.36}$$

Notice that in this expression the summations have been reduced to only one and all magnetic quantum number dependence has disappeared.

To the reader who has used the graphical method before, or who verifies the derivation given here for $\mathcal{M}$, its power and usefulness quickly becomes apparent. Of course, to every graphical manipulation there exists a corresponding set of algebraic manipulations, but the graphical method has a number of advantages. Firstly, the notation is more compact: redundant magnetic quantum numbers are suppressed and certain phase factors and other factors are separated from the real subjects of the manipulation, improving clarity. Secondly, the manipulations are made by recognising geometric patterns. Furthermore, these manipulations may be practiced or tried out without inclusion of all of the calculational details before the full calculation is carried through; phase factors and other factors can be dropped whilst quick sketches are drawn in order to try out various manipulations. The calculation may then be carried out more carefully including all components of the graphs before finally evaluating all additional factors that are not accounted for in the graphs, as was done above when collecting together phase factors. For further reading the reader is referred to the literature previously cited and the references cited therein.

We thus have, finally,

$$
K_{\alpha\gamma}(x,\rho) = \sum_{ac\lambda} A_{ac\lambda}\left[k^{(1)}_{\lambda,\alpha\gamma}(x,\rho) + k^{(2)}_{\lambda,\alpha\gamma}(x,\rho) \times \right.
$$
$$
\left. \left(-\frac{1}{4}\right)\left\{ \frac{\mathrm{d}^2}{\mathrm{d}\rho^2} - \frac{L_\gamma(L_\gamma+1)}{\rho^2} + k'^2_\gamma \right\} \right] \quad \text{(C.37)}
$$

where

$$
A_{ac\lambda} = 8(-)^{J+\lambda} 2^{a+l_\gamma} \hat{l}_\alpha \hat{l}_\gamma (\hat{L}_\alpha \hat{L}_\gamma)^{1/2} x^{a+c} \rho^{l_\alpha+l_\gamma-(a+c)}
$$
$$
\left[\frac{(2\hat{l}_\alpha)!}{(2a)!(2l_\alpha-2a)!} \right]\left[\frac{(2\hat{l}_\gamma)!}{(2c)!(2l_\gamma-2c)!} \right] \times
$$
$$
\sum_j \hat{j} \begin{pmatrix} b & d & j \\ 0 & 0 & 0 \end{pmatrix} \begin{pmatrix} L_\alpha & \lambda & j \\ 0 & 0 & 0 \end{pmatrix} \sum_k \hat{k} \begin{pmatrix} a & c & k \\ 0 & 0 & 0 \end{pmatrix} \begin{pmatrix} L_\gamma & \lambda & k \\ 0 & 0 & 0 \end{pmatrix} \times
$$

$$\sum_y \hat{y} \begin{Bmatrix} l_\alpha & l_\gamma & y \\ b & d & j \\ a & c & k \end{Bmatrix} \begin{Bmatrix} y & L_\alpha & L_\gamma \\ J & l_\gamma & l_\alpha \end{Bmatrix} \begin{Bmatrix} y & k & j \\ \lambda & L_\alpha & L_\gamma \end{Bmatrix} . \tag{C.38}$$

From equation (C.5) we also have

$$K_{\alpha\gamma}^{(i)}(x, \rho) = \sum_{ac\lambda} A_{ac\lambda} k_{\lambda,\alpha\gamma}^{(i)}(x, \rho) \tag{C.39}$$

We note that in this form the kernels $k_{\lambda,\alpha\gamma}^{(i)}(x, \rho)$ are energy independent and depend only on the target expansion (2.21) and the total angular momentum J; all angular factors, also energy independent, are contained in the factor $A_{ac\lambda}$. For each energy all that needs to be evaluated is the derivative given by the last few terms in (C.37).

Matrix element M₄

The matrix element

$$M_4 \equiv \left\langle \overline{\psi} \left| H - E \right| \Psi_D^{JM} \right\rangle$$

$$= \sum_{\gamma L_\gamma} \int_0^\infty x dx \overline{K}_{\gamma\alpha}(\rho, x) f_{\alpha L_\alpha}^J(x) \tag{C.40}$$

is evaluated in much the same way as M_3. Holding $\hat{\rho}$ constant and using the relation $d\boldsymbol{R} = 8d\boldsymbol{x}$ we have

$$\overline{K}_{\gamma\alpha}(\rho, x) = 8 \sum_{m_\gamma m_\gamma'} \left\langle L_\gamma l_\gamma; m_\gamma' m_\gamma | JM \right\rangle \left\langle L_\alpha l_\alpha; m_\alpha' m_\alpha | JM \right\rangle \int d\hat{\rho} \int d\hat{x}$$

$$S_{n_\gamma l_\gamma}(R) Y_{l_\gamma m_\gamma}^*(\hat{R}) Y_{L_\gamma m_\gamma'}^*(\hat{\rho}) \times$$

$$\left[-\frac{1}{2}\nabla_x^2 - \frac{1}{2}\nabla_r^2 - \frac{1}{R} + \frac{Z}{x} - \frac{Z}{r} - E \right] \times$$

$$R_{n_\alpha l_\alpha}(r) Y_{l_\alpha m_\alpha}(\hat{r}) Y_{L_\alpha m_\alpha'}(\hat{x}). \tag{C.41}$$

We now use the relations

$$-\frac{1}{2}\nabla_x^2 = -\frac{1}{2}\left[\frac{d^2}{dx^2} - \frac{L_\alpha(L_\alpha+1)}{x^2} + k_\gamma^2 \right] + \frac{1}{2}k_\gamma^2 \tag{C.42a}$$

$$-\frac{1}{2}\nabla_r^2 = -\frac{1}{2}\left[\frac{d^2}{dr^2} - \frac{l_\alpha(l_\alpha+1)}{r^2} \right] \tag{C.42b}$$

and substitute

$$\overline{K}_{\gamma\alpha}(\rho, x) \equiv \overline{K}_{\gamma\alpha}^{(1)}(\rho, x) + \overline{K}_{\gamma\alpha}^{(2)}(\rho, x). \left(-\frac{1}{2}\right) \left[\frac{d^2}{dx^2} - \frac{L_\alpha(L_\alpha+1)}{x^2} + k_\gamma^2\right]. \quad (C.43)$$

Now, similar to before, putting

$$Y_{l_\gamma m_\gamma}^*(\hat{R}) = (-)^{l_\gamma + m_\gamma} \sum_{\substack{a,b \\ m_a, m_b}} \delta_{l_\gamma, a+b} \left[\frac{4\pi \hat{l}_\gamma!}{\hat{a}! \hat{b}!}\right] (2x)^a (2\rho)^b \times$$

$$Y_{a m_a}(\hat{x}) Y_{b m_b}(\hat{\rho}) \langle ab; m_a m_b | l_\gamma - m_\gamma\rangle R^{-l_\gamma} \quad (C.44a)$$

and

$$Y_{l_\alpha m_\alpha}(\hat{r}) = (-)^{l_\alpha} \sum_{\substack{c,d \\ m_c, m_d}} \delta_{l_\alpha, c+d} \left[\frac{4\pi \hat{l}_\alpha!}{\hat{c}! \hat{d}!}\right] x^c (2\rho)^d \times$$

$$Y_{c m_c}(\hat{x}) Y_{d m_d}(\hat{\rho}) \langle cd; m_c m_d | l_\alpha m_\alpha\rangle r^{-l_\alpha} \quad (C.44b)$$

and evaluating the products of integrals

$$I_{\hat{x}} = \int d\hat{x} Y_{a m_a}(\hat{x}) Y_{\lambda m_\lambda}(\hat{x}) Y_{L_\alpha m_\alpha'}(\hat{x}) Y_{c m_c}(\hat{x})$$

$$= \sum_{j, m_j} \frac{(\hat{a}\hat{c}\hat{\lambda}\hat{L}_\alpha)^{\frac{1}{2}}}{4\pi \hat{j}} \langle L_\alpha \lambda; m_\alpha' m_\lambda | j - m_j\rangle \langle ac; m_a m_c | j m_j\rangle$$

$$\times \langle L_\alpha \lambda; 00 | j0\rangle \langle ac; 00 | j0\rangle (-)^{m_j} \quad (C.45)$$

$$I_{\hat{\rho}} = (-)^{m_\gamma' + m_\lambda} \int d\hat{\rho} Y_{L_\gamma - m_\gamma}(\hat{\rho}) Y_{b m_b}(\hat{\rho}) Y_{\lambda - m_\lambda'}(\hat{\rho}) Y_{d m_d}(\hat{\rho})$$

$$= \sum_{k, m_k} \frac{(\hat{b}\hat{d}\hat{\lambda}\hat{L}_\gamma)^{\frac{1}{2}}}{4\pi \hat{k}} \langle L_\gamma \lambda; m_\gamma' m_\lambda | k m_k\rangle \langle bd; m_b m_d | k m_k\rangle$$

$$\times \langle L_\gamma \lambda; 00 | k0\rangle \langle bd; 00 | k0\rangle, \quad (C.46)$$

we also define

$$\overline{k}_{\lambda, \gamma\alpha}^{(i)}(\rho, x) = \frac{\hat{\lambda}}{2} \int_{-1}^{+1} d(\widehat{\rho x}) P_\lambda(\widehat{\rho x}) Q_{\gamma\alpha}^{(i)}, \quad (C.47)$$

where, similar to $O^{(i)}_{\alpha\gamma}$,

$$
Q^{(1)}_{\gamma\alpha} \equiv R^{-l_\gamma} S_{n_\gamma l_\gamma}(R) r^{-1} \times
$$

$$
\left[-\frac{d^2}{dr^2} + \frac{l_\alpha(l_\alpha+1)}{r^2} + \overline{V}(\rho, x) - \varepsilon_\alpha \right] r R_{n_\alpha l_\alpha}(r) r^{-l_\alpha}
$$

$$
= \sum_{\lambda=0}^{\infty} \overline{k}^{(1)}_{\lambda,\gamma\alpha}(\rho, x) P_\lambda(\widehat{\rho x}) \qquad\qquad \text{(C.48a)}
$$

$$
= 4\pi \sum_{\lambda, m_\lambda} \hat{\lambda}^{-1} \overline{k}^{(1)}_{\lambda,\gamma\alpha}(\rho, x) Y^*_{\lambda m_\lambda}(\hat\rho) Y_{\lambda m_\lambda}(\hat x)
$$

and

$$
Q^{(2)}_{\gamma\alpha} \equiv R^{-l_\gamma} S_{n_\gamma l_\gamma}(R) R_{n_\alpha l_\alpha}(r) r^{-l_\alpha}
$$

$$
= \sum_{\lambda=0}^{\infty} \overline{k}^{(2)}_{\lambda,\gamma\alpha}(\rho, x) P_\lambda(\widehat{\rho x}) \qquad\qquad \text{(C.48b)}
$$

$$
= 4\pi \sum_{\lambda, m_\lambda} \hat{\lambda}^{-1} \overline{k}^{(2)}_{\lambda,\gamma\alpha}(\rho, x) Y^*_{\lambda m_\lambda}(\hat\rho) Y_{\lambda m_\lambda}(\hat x);
$$

$\overline{V}(\rho, x)$ is defined by (C.15). Bringing together all of these results we obtain

$$
\overline{K}^{(i)}_{\gamma\alpha}(\rho, x) = 8(-)^{L_\alpha+L_\gamma} (\hat{L}_\alpha \hat{L}_\gamma)^{1/2} 2^{l_\alpha+l_\gamma-c} \times
$$

$$
\sum_{a,b} \delta_{l_\gamma, a+b} \left[\frac{\hat{l}_\gamma!}{(2a)!(2b)!} \right] \sum_{c,d} \delta_{l_\alpha, c+d} \left[\frac{\hat{l}_\alpha!}{(2c)!(2d)!} \right] \times
$$

$$
x^{a+c} \rho^{b+d} \sum_\lambda \overline{k}^{(i)}_{\lambda,\gamma\alpha}(\rho, x) \times
$$

$$
\sum_j \begin{pmatrix} a & c & j \\ 0 & 0 & 0 \end{pmatrix} \begin{pmatrix} L_\alpha & \lambda & j \\ 0 & 0 & 0 \end{pmatrix} \sum_k \begin{pmatrix} b & d & k \\ 0 & 0 & 0 \end{pmatrix} \begin{pmatrix} L_\gamma & \lambda & k \\ 0 & 0 & 0 \end{pmatrix} \overline{\mathcal{M}} \quad \text{(C.49)}
$$

where

$$
\overline{\mathcal{M}} = \sum (-)^{m_\gamma+m_j} \langle L_\gamma l_\gamma; m'_\gamma m_\gamma | JM \rangle \langle L_\alpha l_\alpha; m'_\alpha m_\alpha | JM \rangle
$$

$$
\langle ab; m_a m_b | l_\gamma - m_\gamma \rangle \langle cd; m_c m_d | l_\alpha m_\alpha \rangle \langle L_\alpha \lambda; m'_\alpha m_\lambda | j - m_j \rangle
$$

$$
\langle ac; m_a m_c | j m_j \rangle \langle L_\gamma \lambda; m'_\gamma m_\lambda | k m_k \rangle \langle bd; m_b m_d | k m_k \rangle. \quad \text{(C.50)}
$$

In order to evaluate $\overline{\mathcal{M}}$ we compare (C.50) with (C.19). Making the substitutions

$$
\begin{array}{cc}
L_\alpha \to L_\gamma & L_\gamma \to L_\alpha \\[4pt]
m'_\alpha \to m'_\gamma & m'_\gamma \to m'_\alpha \\[4pt]
l_\alpha \to l_\gamma & l_\gamma \to l_\alpha \\[4pt]
m_\alpha \to m_\gamma \cdot & m_\gamma \to m_\alpha \\[4pt]
j \to k & k \to j \\[4pt]
m_j \to m_k & m_k \to m_j
\end{array}
\tag{C.51}
$$

we see that $\overline{\mathcal{M}} \to \mathcal{M}$. It follows immediately then that

$$
\overline{\mathcal{M}} = (-)^{J+L_\alpha+L_\gamma+\lambda}\hat{j}\hat{k}(\hat{l}_\alpha\hat{l}_\gamma)^{1/2}\sum_y \hat{y}
\tag{C.52}
$$

$$
\times
\begin{Bmatrix} l_\gamma & l_\alpha & y \\ b & d & k \\ a & c & j \end{Bmatrix}
\begin{Bmatrix} y & L_\gamma & L_\alpha \\ J & l_\alpha & l_\gamma \end{Bmatrix}
\begin{Bmatrix} y & j & k \\ \lambda & L_\gamma & L_\alpha \end{Bmatrix}.
\tag{C.53}
$$

Notice that in this expression the summations have been reduced to only one and all magnetic quantum number dependence has disappeared.

We thus have, finally,

$$
\overline{K}_{\gamma\alpha}(\rho,x) = \sum_{ac\lambda}\overline{A}_{ac\lambda}\left[\overline{k}^{(1)}_{\lambda,\gamma\alpha}(\rho,x) + \overline{k}^{(2)}_{\lambda,\gamma\alpha}(\rho,x) \times \right.
$$

$$
\left. \left(-\frac{1}{2}\right)\left\{\frac{\mathrm{d}^2}{\mathrm{d}x^2} - \frac{L_\gamma(L_\alpha+1)}{x^2} + k_\alpha^2\right\}\right]
\tag{C.54}
$$

where

$$
\overline{A}_{ac\lambda} = 8(-)^{J+\lambda}2^{l_\alpha+l_\gamma-c}\hat{l}_\alpha\hat{l}_\gamma(\hat{L}_\alpha\hat{L}_\gamma)^{1/2}x^{a+c}\rho^{l_\alpha+l_\gamma-(a+c)}
$$

$$
\left[\frac{(2\hat{l}_\alpha)!}{(2c)!(2l_\alpha-2c)!}\right]\left[\frac{(2\hat{l}_\gamma)!}{(2a)!(2l_\gamma-2a)!}\right]\times
$$

$$
\sum_j \hat{j}\begin{pmatrix} a & c & j \\ 0 & 0 & 0 \end{pmatrix}\begin{pmatrix} L_\alpha & \lambda & j \\ 0 & 0 & 0 \end{pmatrix}\sum_k \hat{k}\begin{pmatrix} b & d & k \\ 0 & 0 & 0 \end{pmatrix}\begin{pmatrix} L_\gamma & \lambda & k \\ 0 & 0 & 0 \end{pmatrix}\times
$$

$$
\sum_y \hat{y}\begin{Bmatrix} l_\gamma & l_\alpha & y \\ b & d & k \\ a & c & j \end{Bmatrix}\begin{Bmatrix} y & L_\gamma & L_\alpha \\ J & l_\alpha & l_\gamma \end{Bmatrix}\begin{Bmatrix} y & j & k \\ \lambda & L_\gamma & L_\alpha \end{Bmatrix}.
\tag{C.55}
$$

From equation (C.43) we also have

$$\overline{K}^{(i)}_{\gamma\alpha}(\rho, x) = \sum_{ac\lambda} \overline{A}_{ac\lambda} \overline{k}^{(i)}_{\lambda,\gamma\alpha}(\rho, x) \tag{C.56}$$

Similarly to the matrix element M_3 the kernels $\overline{K}^{(i)}_{\lambda,\gamma\alpha}(\rho, x)$ are energy independent and depend only on the target expansion (2.21) and the total angular momentum J; all angular factors, also energy independent, are contained in the factor $\overline{A}_{ac\lambda}$. For each energy all that needs to be evaluated is the derivative given by the last few terms in (C.54).

Direct potentials $\mathbf{V}_{\alpha\beta}$ and $\mathbf{W}_{\gamma\delta}$

The two direct potentials are given by the matrix elements (2.33)

$$V_{\alpha\beta} = \left\langle \phi_\alpha \left| \frac{1}{x} - \frac{1}{R} \right| \phi_\beta \right\rangle \tag{C.57}$$

$$W_{\gamma\delta} = \left\langle \psi_\gamma \left| \frac{Z}{x} - \frac{Z}{r} \right| \psi_\delta \right\rangle. \tag{C.58}$$

Writing (C.57) out in full we have

$$V_{\alpha\beta}(x) = 2 \sum \langle L_\alpha l_\alpha; m'_\alpha m_\alpha | JM \rangle \langle L_\beta l_\beta; m'_\beta m_\beta | JM \rangle \int d\hat{x} \int d\boldsymbol{r}$$

$$R_{n_\alpha l_\alpha}(r) R_{n_\beta l_\beta}(r) Y^*_{l_\alpha m_\alpha}(\hat{r}) Y_{l_\beta m_\beta}(\hat{r}) Y^*_{L_\alpha m'_\alpha}(\hat{x}) Y_{L_\beta m'_\beta}(\hat{x}) \left[\frac{1}{x} - \frac{1}{R} \right]. \tag{C.59}$$

Noting that $R = |\boldsymbol{r} - \boldsymbol{x}|$ and introducing the notation

$$\tilde{Y}^{JM}_{l_1 l_2}(\hat{r}_1; \hat{r}_2) = \sum_{m_1, m_2} \langle l_1 l_2; m_1 m_2 | JM \rangle Y_{l_1 m_1}(\hat{r}_1) Y_{l_2 m_2}(\hat{r}_2) \tag{C.60}$$

this may be rewritten

$$V_{\alpha\beta}(x) = 2 \int d\hat{x} \int d\boldsymbol{r} R_{n_\alpha l_\alpha}(r) R_{n_\beta l_\beta}(r) \tilde{Y}^{JM}_{L_\alpha l_\alpha}{}^* \tilde{Y}^{JM}_{L_\beta l_\beta} \left[\frac{1}{x} - \frac{1}{|\boldsymbol{r} - \boldsymbol{x}|} \right], \tag{C.61}$$

where, as usual, $*$ denotes complex conjugation. The first term is straight-forward to evaluate, giving $\delta_{\alpha\beta}\left(\frac{2}{x}\right)$. For the second term we use the result [87]

$$I = \int d\hat{x} \int d\hat{r} \, \tilde{Y}^{JM}_{Ll}{}^* \frac{1}{|\boldsymbol{r} - \boldsymbol{x}|} \tilde{Y}^{JM}_{L'l'}$$

$$= \sum_\lambda \gamma_\lambda(r, x) C_\lambda(Ll; L'l'; J) \tag{C.62}$$

where

$$C_\lambda(Ll; L'l'; J) = (-)^\lambda \left[(2L+1)(2l+1) \right]^{1/2} \times$$

$$\langle L'\lambda; 00|L0 \rangle \langle l'\lambda; 00|l0 \rangle \, W(L'\lambda Jl; Ll') \quad (C.63)$$

is a Percival-Seaton coefficient, $W(L'\lambda Jl; Ll')$ is a Racah W-coefficient [206], and

$$\gamma_\lambda(r, x) = \begin{cases} \frac{r^\lambda}{x^{\lambda+1}}, & x > r \\[2mm] \frac{x^\lambda}{r^{\lambda+1}}, & r > x. \end{cases} \quad (C.64)$$

This is proved as follows.

Expanding

$$\frac{1}{|\boldsymbol{r} - \boldsymbol{x}|} = \sum_{\lambda=0}^{\infty} \sum_{\mu=-\lambda}^{\lambda} \frac{4\pi}{\hat{\lambda}} \gamma_\lambda(r, x) Y_{\lambda\mu}^*(\hat{r}) Y_{\lambda\mu}(\hat{x}) \quad (C.65)$$

we have two integrals over products of three spherical harmonics. These may be evaluated by use of

$$Y_{l_1 m_1}(\Omega) Y_{l_2 m_2}(\Omega) = \sum_{l,m} \left[\frac{\hat{l}_1 \hat{l}_2}{4\pi \hat{l}} \right]^{1/2} \langle l_1 l_2; 00|l0 \rangle \langle l_1 l_2; m_1 m_2|lm \rangle \, Y_{lm}(\Omega), \quad (C.66)$$

the fact that

$$Y_{lm}^*(\Omega) = (-)^m Y_{l-m}(\Omega) \quad (C.67)$$

and the orthogonality of the spherical harmonics. From this we obtain

$$C_\lambda(Ll; L'l'; J) = \sum (-)^{m_L + m_l + \mu} \frac{(\hat{L}\hat{l}\hat{L}'\hat{l}')^{1/2}}{\hat{\lambda}^2} \langle Ll; m_L m_l|JM \rangle \langle L'l'; m_{L'} m_{l'}|JM \rangle$$

$$\langle LL'; -m_L m_{L'}|\lambda\mu \rangle \langle ll'; -m_l m_{l'}|\lambda - \mu \rangle \langle LL'; 00|\lambda 0 \rangle \langle ll'; 00|\lambda 0 \rangle . \quad (C.68)$$

Using the symmetry relations of the Clebsch-Gordan coefficients we make the replacement

$$\langle LL'; 00|\lambda 0 \rangle \langle ll'; 00|\lambda 0 \rangle$$

$$= \frac{\hat{\lambda}}{(\hat{L}\hat{l})^{1/2}} (-)^{L+l} \langle L'\lambda; 00|L0 \rangle \langle l'\lambda; 00|l0 \rangle . \quad (C.69)$$

This can now be manipulated in graphical form giving

$$C_\lambda(Ll; L'l'; J) = (-)^\lambda (\hat{L}'\hat{l}')^{1/2} \langle L'\lambda; 00|L0\rangle \langle l'\lambda; 00|l0\rangle$$
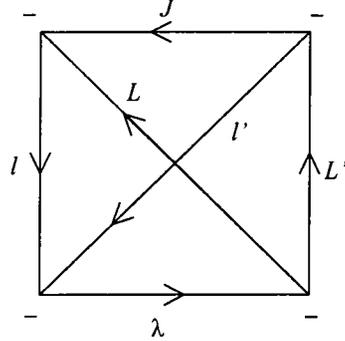
$$= (-)^\lambda (\hat{L}'\hat{l}')^{1/2} \langle L'\lambda; 00|L0\rangle \langle l'\lambda; 00|l0\rangle$$

$$(-)^{J+L+L'+\lambda}$$
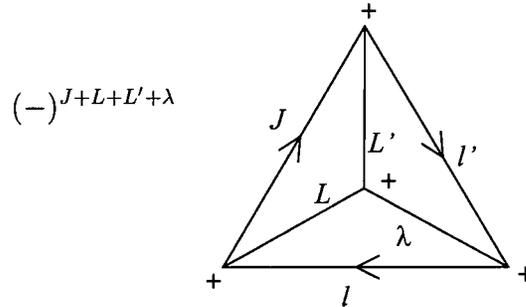
$$= (-)^\lambda (\hat{L}\hat{l})^{1/2} \langle L'\lambda; 00|L0\rangle \langle l'\lambda; 00|l0\rangle$$

$$(-)^{J+L+L'+\lambda} \begin{Bmatrix} L' & \lambda & L \\ l & J & l' \end{Bmatrix}$$

$$= (-)^\lambda (\hat{L}\hat{l})^{1/2} \langle L'\lambda; 00|L0\rangle \langle l'\lambda; 00|l0\rangle \, W(L'\lambda Jl; Ll'). \qquad (C.70)$$

We thus have the final result

$$V_{\alpha\beta}(x) = \frac{2}{x}\delta_{\alpha\beta} - 2\sum_\lambda C_\lambda(L_\alpha l_\alpha; L_\beta l_\beta; J) \times$$

$$\int_0^\infty r^2 dr \, \gamma_\lambda(r, x) R_{n_\alpha l_\alpha}(r) R_{n_\beta l_\beta}(r). \qquad (C.71)$$

Here the integral may be evaluated analytically in the case of real (eigenstate) targets or numerically in the case of pseudostates.

We now proceed to the other direct potential, $W_{\gamma\delta}(\rho)$. Writing it out in full we

have

$$W_{\gamma\delta}(\rho) = 4 \sum_{g} \langle L_\gamma l_\gamma; m'_\gamma m_\gamma | JM \rangle \langle L_\delta l_\delta; m'_\delta m_\delta | JM \rangle \int d\hat{\rho} \int d\boldsymbol{R}$$

$$S_{n_\gamma l_\gamma}(R) S_{n_\delta l_\delta}(R) Y^*_{l_\gamma m_\gamma}(\hat{R}) Y_{l_\delta m_\delta}(\hat{R}) Y^*_{L_\gamma m'_\gamma}(\hat{\rho}) Y_{L_\delta m'_\delta}(\hat{\rho}) \left[\frac{Z}{x} - \frac{Z}{r} \right], \quad \text{(C.72)}$$

where the sum is over the magnetic quantum numbers. The rest of the derivation proceeds much the same as for $V_{\alpha\beta}(x)$, noting that

$$\frac{1}{r} = \frac{1}{|\frac{1}{2}\boldsymbol{R} - \boldsymbol{\rho}|} = \sum_{\lambda=0}^{\infty} \gamma_\lambda(\rho, \tfrac{1}{2}R) P_\lambda(\mu) \qquad \text{(C.73a)}$$

$$\frac{1}{x} = \frac{1}{|\frac{1}{2}\boldsymbol{R} + \boldsymbol{\rho}|} = \sum_{\lambda=0}^{\infty} (-)^\lambda \gamma_\lambda(\rho, \tfrac{1}{2}R) P_\lambda(\mu), \qquad \text{(C.73b)}$$

where the factor $(-)^\lambda$ arises due to the parity of the Legendre polynomial ($\mu \to -\mu$). Defining

$$\Gamma_\lambda(R, \rho) = -\gamma_\lambda(\rho, \tfrac{1}{2}R) \left[1 - (-)^\lambda \right] \qquad \text{(C.74)}$$

we thus have

$$W_{\gamma\delta}(\rho) = 4Z \sum_{\lambda} C_\lambda(L_\gamma l_\gamma; L_\delta l_\delta; J) \int_0^\infty R^2 dR\, \Gamma_\lambda(R, \rho) S_{n_\gamma l_\gamma}(R) S_{n_\delta l_\delta}(R). \quad \text{(C.75)}$$

It is worth noting that the contribution to the potential is zero for values of λ that are even. This is a consequence of the charge-mass symmetry of positronium which does not occur for, say, hydrogen.

Bibliography

[1] A. L. Merts and L. A. Collins, "A least-squares technique for electron scattering by atoms and molecules," J. Phys. B **18**, L29–33 (1985).

[2] B. H. Bransden and C. J. Noble, "Application of least-squares methods to atomic rearrangement collisions," J. Phys. B **32**, 1305–14 (1999).

[3] R. Damburg and E. Karule, "A modification of the close-coupling approximation for e-H scattering allowing for the long-range interactions," Proc. Phys. Soc. **90**, 637–40 (1967).

[4] I. Bray and A. T. Stelbovics, "Explicit demonstration of the convergence of the close-coupling method for a Coulomb three-body problem," Phys. Rev. Lett. **69**, 53–6 (1992).

[5] P. A. M. Dirac, Proc. Roy. Soc. A **118**, 351 (1928).

[6] C. D. Anderson, Phys. Rev. **43**, 491 (1933).

[7] A. Ore, Univ. Bergen Arbok Natur. Rekke 9 and 12 (1949).

[8] H. S. W. Massey and C. B. O. Mohr, "Gaseous reactions involving positronium," Proc. Phys. Soc. London A **67**, 695–704 (1954).

[9] B. H. Bransden, "Positron Collisions," in *Case Studies in Atomic Collision Physics*, E. W. McDaniel and M. R. C. McDowell, eds., (North-Holland Publishing Company, Amsterdam, 1969), Vol. I, Chap. 4, pp. 169–248.

[10] A. S. Ghosh, N. C. Sil, and P. Mandal, "Positron-atom and positron-molecule collisions," Phys. Rep. **87**, 313–406 (1982).

[11] G. G. Ryzhikh and J. Mitroy, "Positronic Lithium, an Electronically Stable Li-e$^+$ Ground State," Phys. Rev. Lett. **79**, 4124-6 (1997).

[12] G. G. Ryzhikh, J. Mitroy, and K. Varga, "The structure of exotic atoms containing positrons and positronium," J. Phys. B **31**, 3965-96 (1998).

[13] J. Mitroy, M. W. J. Bromley, and G. G. Ryzhikh, "Positron binding to a model alkali atom," J. Phys. B **32**, 2203-14 (1999).

[14] G. Gabrielse *et al* , "The Production and Study of Cold Antihydrogen," ATRAP proposal SPSC 97-8, CERN (1997) .

[15] M. H. Holzscheiter *et al* , "Antihydrogen Production and Precision Experiments," ATHENA proposal SPSLC 96-47, CERN (1996) .

[16] T. Azuma *et al* , "Atomic Spectroscopy and Collisions using Slow Antiprotons," ASACUSA proposal SPSC 97-19, CERN (1997) .

[17] M. Charlton, J. Eades, D. Horváth, R. J. Hughes, and C. Zimmermann, "Antihydrogen physics," Phys. Rep. **241**, 65-117 (1994).

[18] M. H. Holzscheiter and M. Charlton, "Ultra-low energy antihydrogen," Rep. Prog. Phys. **62**, 1-60 (1999).

[19] J. Eades and F. J. Hartmann, "Forty years of antiprotons," Rev. Mod. Phys. **71**, 373-419 (1999).

[20] E. A. G. Armour and J. W. Humberston, "Methods and programs in collisions of positrons with atoms and molecules," Phys. Rep. **204**, 165-251 (1991).

[21] C. P. Campbell, M. T. McAlinden, A. A. Kernoghan, and H. R. J. Walters, "Positron collisions with one- and two-electron atoms," Nuc. Instr. B **143**, 41-56 (1998).

[22] J. W. Humberston, "Positronium formation in s-wave positron-hydrogen scattering," J. Phys. B **17**, 2353-61 (1984).

[23] C. J. Brown and J. W. Humberston, "Positronium formation in p-wave positron-hydrogen scattering," J. Phys. B **17**, L423–6 (1984).

[24] C. J. Brown and J. W. Humberston, "Positronium formation in positron-hydrogen scattering," J. Phys. B **18**, L401–6 (1985).

[25] J. W. Humberston, P. Van Reeth, M. S. T. Watts, and W. E. Meyerhof, "Positron-hydrogen scattering in the vicinity of the positronium formation threshold," J. Phys. B **30**, 2477–93 (1997).

[26] Y. R. Kuang and T. T. Gien, "Positron-hydrogen collisions at low energies," Phys. Rev. A **55**, 256–64 (1997).

[27] T. T. Gien, "Accurate algebraic coupled-state calculation of positron-hydrogen scattering at low energies," J. Phys. B **30**, L23–30 (1997).

[28] A. A. Kernoghan, M. T. McAlinden, and H. R. J. Walters, "Resonances above the ionization threshold in positron-hydrogen scattering," J. Phys. B **27**, L543–49 (1994).

[29] A. A. Kernoghan, M. T. McAlinden, and H. R. J. Walters, "An 18-state calculation of positron-hydrogen scattering," J. Phys. B **28**, 1079–94 (1995).

[30] A. A. Kernoghan, D. J. R. Robinson, M. T. McAlinden, and H. R. J. Walters, "Positron scattering by atomic hydrogen," J. Phys. B **29**, 2089–102 (1996).

[31] K. Higgins and P. G. Burke, "Positron scattering by atomic hydrogen including positronium formation," J. Phys. B **24**, L343–9 (1991).

[32] K. Higgins and P. G. Burke, "Positron scattering by atomic hydrogen including positronium formation," J. Phys. B **26**, 4269–88 (1993).

[33] K. Higgins, P. G. Burke, and H. R. J. Walters, "Positron scattering by atomic hydrogen at intermediate energies," J. Phys. B **23**, 1345–57 (1990).

[34] A. Igarashi and N. Toshima, "Hyperspherical coupled-channel study of positronium formation," Phys. Rev. A **50**, 232–9 (1994).

[35] Y. Zhou and C. D. Lin, "Hyperspherical close-coupling calculation of positronium formation cross sections in positron-hydrogen scattering at low energies," J. Phys. B **27**, 5065–81 (1994).

[36] Y. Zhou and C. D. Lin, "Hyperspherical close-coupling calculation of positronium formation and excitation cross sections in positron-hydrogen scattering at energies below the H($n = 4$) threshold," J. Phys. B **28**, 4907–25 (1995).

[37] A. Igarashi and I. Shimamura, "S-wave resonances in positron scattering by He$^+$," Phys. Rev. A **56**, 4733–6 (1997).

[38] I. Bray and A. T. Stelbovics, "Convergent close-coupling calculations of low-energy positron-atomic-hydrogen scattering," Phys. Rev. A **48**, 4787–9 (1993).

[39] I. Bray and A. T. Stelbovics, "Calculation of the total and total ionization cross sections for positron scattering on atomic hydrogen," Phys. Rev. A **49**, R2224–6 (1994).

[40] A. S. Kadyrov and I. Bray, "Convergent close-coupling calculations of the S-wave model of positron-hydrogen scattering," Nuc. Instr. B **171**, 119–25 (2000).

[41] A. S. Kadyrov and I. Bray, "Convergence of two-centre expansions in positron-hydrogen collisions," J. Phys. B **33**, L635–40 (2000).

[42] J. Mitroy, "Another s-wave resonance in positron-hydrogen scattering," J. Phys. B **26**, L625–31 (1993).

[43] J. Mitroy, "Close coupling calculations of positron-hydrogen scattering at low energies," J. Phys. B **26**, 4861–9 (1993).

[44] J. Mitroy, "Close Coupling Theory of Positron-Hydrogen Scattering," Aust. J. Phys. **46**, 751–71 (1993).

[45] J. Mitroy, "An L^2 calculation of positron-hydrogen scattering at intermediate energies," J. Phys. B **29**, L263–9 (1996).

[46] J. Mitroy, L. Berge, and A. T. Stelbovics, "Positron-hydrogen scattering at low energies," Phys. Rev. Lett. **73**, 2966–9 (1994).

[47] J. Mitroy and A. T. Stelbovics, "Resonance structure in the positron-hydrogen system above the ionization threshold," J. Phys. B **27**, L55–60 (1994).

[48] J. Mitroy and A. T. Stelbovics, "The positron-hydrogen system in a six state model," J. Phys. B **27**, 3257–75 (1994).

[49] J. Mitroy and A. T. Stelbovics, "Positronium and antihydrogen formation in the e^+–H and Ps–$\bar{p}$ systems," Phys. Rev. Lett. **72**, 3495–7 (1994).

[50] J. Mitroy and K. Ratnavelu, "The positron-hydrogen system at low energies," J. Phys. B **28**, 287–306 (1995).

[51] D. Basu, G. Banerji, and A. S. Gosh, "Positron-hydrogen scattering using an integral approach," Phys. Rev. A **13**, 1381–7 (1976).

[52] D. Basu, M. Mukherjee, and A. S. Gosh, "Positron-hydrogen scattering including short- and long-range correlations," J. Phys. B **22**, 2195–204 (1989).

[53] R. N. Hewitt, C. J. Noble, and B. H. Bransden, "Positronium formation in positron-hydrogen scattering," J. Phys. B **23**, 4185–95 (1990).

[54] R. N. Hewitt, C. J. Noble, and B. H. Bransden, "Intermediate energy resonances in positron-hydrogen scattering," J. Phys. B **24**, L635–9 (1991).

[55] J. W. Humberston, "Positronium—its formation and interaction with simple systems," Adv. At. Mol. Phys. **22**, 1–36 (1986).

[56] B. H. Bransden and C. J. Noble, "Positronium formation by positron impact on atoms at intermediate energies," Adv. At. Mol. Phys. **32**, 19–37 (1994).

[57] J. P. Merrison, H. Bluhme, J. Chevallier, B. I. Deutch, P. Hvelplund, L. V. Jørgensen, H. Knudsen, M. R. Poulsen, and M. Charlton, "Hydrogen Formation by Proton Impact on Positronium," Phys. Rev. Lett. **78**, 2728–31 (1997).

[58] J. P. Merrison, H. Blume, M. Charlton, H. Knudsen, and M. R. Poulsen, "Experimental demonstration of hydrogen formation following the interaction of protons with positronium," Hyp. Int. **109**, 313–21 (1997).

[59] M. Charlton, "Possible antihydrogen formation in antiproton-positronium reactions: where we've been and where we're going," Hyp. Int. **109**, 269–78 (1997).

[60] C. M. Surko, R. G. Greaves, and M. Charlton, "Stored positrons for antihydrogen production," Hyp. Int. **109**, 181–8 (1997).

[61] R. J. Drachman, "A general overview of positron collision physics," Nuc. Instr. B **143**, 1–10 (1998).

[62] P. T. Greenland, "Antimatter," Contemp. Phys. **38**, 181–203 (1997).

[63] C. M. Surko, R. G. Greaves, K. Iwata, and S. J. Gilbert, "Atomic and molecular physics using positron accumulation techniques— summary and a look to the future," Nuc. Instr. B **171**, 2–16 (2000).

[64] W. Sperber, D. Becker, K. G. Lynn, W. Raith, A. Schwab, G. Sinapius, G. Spicher, and M. Weber, "Measurement of positronium formation in positron collisions with hydrogen atoms," Phys. Rev. Lett. **68**, 3690–3 (1992).

[65] G. O. Jones, M. Charlton, J. Slevin, G. Laricchia, À. Kövér, M. R. Poulsen, and S. Nic Chormaic, "Positron Impact Ionization of Atomic Hydrogen," J. Phys. B **26**, L483–8 (1993).

[66] S. Zhou, H. Li, W. E. Kauppila, C. K. Kwan, and T. S. Stein, "Measurements of total and positronium formation cross sections for positrons and electrons scattered by hydrogen atoms and molecules," Phys. Rev. A **55**, 361–8 (1997).

[67] P. Defrance, F. Brouillard, W. Claeys, and G. V. Wassenhove, "Crossed beam measurement of absolute cross sections: an alternative method and its application to the impact ionisation of He$^+$," J. Phys. B **14**, 103–10 (1981).

[68] M. T. McAlinden, A. A. Kernoghan, and H. R. J. Walters, "Positron scattering by potassium," J. Phys. B **29**, 555–69 (1996).

[69] A. A. Kernoghan, M. T. McAlinden, and H. R. J. Walters, "Positron scattering by rubidium and caesium," J. Phys. B **29**, 3971–87 (1996).

[70] M. T. McAlinden, A. A. Kernoghan, and H. R. J. Walters, "Positron scattering by potassium," J. Phys. B **30**, 1543–61 (1997).

[71] P. Van Reeth and J. W. Humberston, "The use of inexact helium wavefunctions in positron-helium scattering," J. Phys. B **28**, L23–8 (1995).

[72] P. Van Reeth and J. W. Humberston, "Positronium formation in low energy s-wave positron-helium scattering," J. Phys. B **28**, L511–7 (1995).

[73] P. Van Reeth and J. W. Humberston, "A partial-wave analysis of positronium formation in positron-helium scattering," J. Phys. B **30**, L95–100 (1997).

[74] P. Van Reeth and J. W. Humberston, "Elastic scattering and positronium formation in low-energy positron-helium collisions," J. Phys. B **32**, 3651–67 (1999).

[75] P. Van Reeth and J. W. Humberston, "Theoretical studies of threshold features in the cross-sections for low-energy e^+-H and e^+-He scattering," Nuc. Instr. B **171**, 106–12 (2000).

[76] G. Ryzhikh and J. Mitroy, "Positron scattering from atomic sodium," J. Phys. B **30**, 5545–65 (1997).

[77] M. S. T. Watts and J. W. Humberston, "Low energy s-wave positron-lithium scattering," J. Phys. B **25**, L491–6 (1992).

[78] R. N. Hewitt, C. J. Noble, and B. H. Bransden, "He(2^1S,2^1P) excitation and positronium formation in positron-helium collisions at intermediate energies," J. Phys. B **25**, 557–70 (1992).

[79] R. N. Hewitt, C. J. Noble, and B. H. Bransden, "The effect of positronium formation on close-coupling calculations of positron-lithium collisions," J. Phys. B **25**, 2683–95 (1992).

[80] R. N. Hewitt, C. J. Noble, and B. H. Bransden, "Positron collisions with alkali atoms at low and intermediate energies," J. Phys. B **26**, 3661–77 (1993).

[81] F. A. Gianturco and R. Melissa, "A new model optical potential for Ps formation in positron scattering from H and He," Europhys. Lett. **33**, 661–6 (1996).

[82] F. A. Gianturco and R. Melissa, "Positronium formation in positron-alkali-metal-atom collisions: An optical potential approach," Phys. Rev. A **54**, 357–64 (1996).

[83] F. A. Gianturco and R. Melissa, "Positronium formation with ionic targets: an optical potential calculation," J. Phys. B **29**, L719–24 (1996).

[84] J. E. Blackwood, C. P. Campbell, M. T. McAlinden, and H. R. J. Walters, "Positronium scattering by helium," Phys. Rev. A **60**, 4454–60 (1999).

[85] B. H. Bransden, A. M. Ermolaev, R. N. Hewitt, and C. J. Noble, "Momentum-space calculations of scattering between charged atomic systems—application to the formation of the positronium negative ion in positronium collisions with atomic hydrogen," J. Phys. B **28**, 1603–12 (1995).

[86] H. S. W. Massey and C. B. O. Mohr, "The Collision of Slow Electrons with Atoms. I. General Theory and Elastic Collisions," Proc. Roy. Soc. London A **136**, 289–311 (1932).

[87] I. C. Percival and M. J. Seaton, "The partial wave theory of electron-hydrogen atom collisions," Proc. Camb. Phil. Soc. **53**, 654–62 (1957).

[88] L. F. Shampine, *Numerical Solution of Ordinary Differential Equations* (Chapman & Hall, Inc., London, 1994).

[89] H. R. J. Walters, A. A. Kernoghan, M. T. McAlinden, and C. P. Campbell, in *Photon and Electron Collisions with Atoms and Molecules*, P. G. Burke and C. J. Joachain, eds., (Plenum Press, New York, 1997).

[90] B. Simon, Math. Ann. **207**, 133 (1974).

[91] B. Simon, Int. J. Quantum Chem. **14**, 529 (1978).

[92] P. G. Burke and T. G. Webb, "Electron scattering by atomic hydrogen using a pseudostate expansion I. Elastic scattering," J. Phys. B **2**, 1142–54 (1969).

[93] S. Geltman and P. G. Burke, "Electron scattering by atomic hydrogen using a pseudostate expansion II. Excitation of 2s and 2p states near threshold," J. Phys. B **3**, 1062–72 (1970).

[94] P. G. Burke and T. G. Webb, "Electron scattering by atomic hydrogen using a pseudostate expansion III. Excitation of 2s and 2p states at intermediate energies," J. Phys. B **3**, L131–4 (1970).

[95] A. Temkin, "Nonadiabatic theory of electron-hydrogen scattering," Phys. Rev. **126**, 130 (1962).

[96] R. Poet, "The exact solution for a simplified model of electron scattering by hydrogen atoms," J. Phys. B **11**, 3081–94 (1978).

[97] B. H. Bransden, *Atomic Collision Theory*, 2nd ed. (The Benjamin/Cummings Publishing Company, Inc., Reading, Massachusetts, 1983).

[98] N. F. Mott and H. S. W. Massey, *The Theory of Atomic Collisions*, 3rd ed. (Clarendon Press, Oxford, 1965).

[99] C. J. Noble and R. K. Nesbet, "CFASYM, a program for the calculation of the asymptotic solutions of the coupled equations of electron collision theory," Comp. Phys. Comm. **33**, 399–411 (1984).

[100] P. G. Burke and C. J. Noble, Comp. Phys. Comm. **85**, 471 (1995).

[101] J. C. Light and R. B. Walker, "An R-matrix approach to the solution of coupled equations for atom-molecule reactive scattering," J. Chem. Phys. **65,** 4272 (1976).

[102] L. M. Delves and J. L. Mohamed, *Computational Methods for Integral Equations* (Cambridge University Press, 1985).

[103] L. M. Delves and J. Walsh, *Numerical Solution of Integral Equations* (Clarendon Press, Oxford, 1974).

[104] G. H. Golub and C. F. Van Loan, *Matrix computations*, 2nd ed. (John Hopkins University Press, Baltimore, 1989).

[105] A. H. Stroud and D. Secrest, *Gaussian Quadrature Formulas* (Prentice-Hall Inc., Englewood Cliffs, N. J., 1966).

[106] C. J. Joachain, *Quantum Collision Theory*, 3rd ed. (North-Holland, 1983).

[107] P. G. Burke and C. J. Joachain, *Theory of Electron-Atom Collisions Part I: Potential Scattering* (Plenum Press, New York, 1995).

[108] L. A. Morgan, "A generalized R-matrix propagation program for solving coupled second-order differential equations," Comp. Phys. Comm. **31,** 419–22 (1984).

[109] V. M. Burke and C. J. Noble, "FARM — a flexible asymptotic R-matrix package," Comp. Phys. Comm. **85,** 471–500 (1995).

[110] K. L. Baluja, P. G. Burke, and L. A. Morgan, "R-matrix propagation program for solving coupled second-order differential equations," Comp. Phys. Comm. **27,** 299–307 (1982).

[111] B. I. Schneider and R. B. Walker, "The coupled channel R-matrix propagation method," J. Chem. Phys. **70,** 2466–70 (1979).

[112] E. B. Stechel, R. B. Walker, and J. C. Light, "R-matrix solution of coupled equations for inelastic scattering," J. Chem. Phys. **65,** 3518–31 (1978).

[113] C. Bloch, "Une formulation unifiée de la théorie des réactions nucléaires," Nucl. Phys. **4**, 503–28 (1957).

[114] A. M. Lane and D. Robson, "Comprehensive formalism for nuclear reaction problems. I. Derivation of existing reaction theories," Phys. Rev. **151**, 774–87 (1966).

[115] E. P. Wigner and L. Eisenbud, "Higher angular momenta and long range interaction in resonance reactions," Phys. Rev. **72**, 29–41 (1947).

[116] E. P. Wigner, "Resonance reactions and anomalous scattering," Phys. Rev. **70**, 15 (1946).

[117] E. P. Wigner, "Resonance reactions," Phys. Rev. **70**, 606 (1946).

[118] P. G. Burke and K. A. Berrington, *Atomic and Molecular Processes: an R-matrix approach* (Institute of Physics Publishing, Bristol, 1993).

[119] M. A. Preston, *Physics of the nucleus* (Addison-Wesley, 1962).

[120] P. G. Burke and W. D. Robb, "The R-matrix theory of atomic processes," Adv. At. Mol. Phys. **11**, 143–214 (1975).

[121] P. G. Burke, in *Atomic Physics*, H. Narumi and I. Shimamura, eds., (Elsevier, Amsterdam, 1987), Vol. 10, p. 243.

[122] R. K. Nesbet, *Variational Methods in Electron-Atom Scattering Theory* (Plenum Press, New York, 1980).

[123] L. Hulthén, Kgl. Fysiogr. Sallsk. Lund Förh. 14 (1944).

[124] L. Hulthén, Arkiv. Mat. Ast. Fys. **35**, 25 (1948).

[125] W. Kohn, "Variational methods in nuclear collision problems," Phys. Rev. **74**, 1763–72 (1948).

[126] C. Schwartz, "Variational calculations of scattering," Ann. Phys. **16**, 36 (1961).

[127] C. Schwartz, "Electron scattering from hydrogen," Phys. Rev. **124**, 1468 (1961).

[128] F. E. Harris, "Expansion approach to scattering," Phys. Rev. Lett. **19**, 173 (1967).

[129] I. Shimamura, "Harris-method calculations of electron and positron scattering by hydrogen-like ions," J. Phys. Soc. Japan **31**, 217–29 (1971).

[130] J. L. Jackson, "A variational approach to nuclear reactions," Phys. Rev. **83**, 301–4 (1951).

[131] J. Schwinger, "A variational principle for scattering problems," Phys. Rev. **72**, 742 (1947).

[132] S. Kar and P. Mandal, "Multichannel Schwinger's principle for rearrangement collisions: positronium formation in positron-hydrogen collisions," Phys. Rev. A **59**, 1913–25 (1999).

[133] C. D. Lin, "Hyperspherical coordinate approach to atomic and other Coulombic three-body systems," Phys. Rep. **257**, 1–83 (1995).

[134] H. Feshbach, "Unified theory of nuclear reactions," Ann. Phys. **5**, 357–90 (1958).

[135] H. Feshbach, "A unified theory of nuclear reactions II," Ann. Phys. **19**, 287–313 (1962).

[136] B. H. Bransden, C. J. Noble, and R. N. Hewitt, "The interpretation of resonance formation in coupled-channel models of positron scattering by atomic hydrogen using localized optical potentials," J. Phys. B **30**, 2299–315 (1997).

[137] P. Khan, P. S. Mazumder, and A. S. Ghosh, "Positron-hydrogen-like-ion scattering," Z. Phys. A **318**, 19–23 (1984).

[138] G. Arfken, *Mathematical Methods for Physicists*, 3rd ed. (Academic Press, Inc., London, 1985).

[139] B. H. Bransden and C. J. Joachain, *Physics of Atoms and Molecules* (Longman, 1983).

[140] B. H. Bransden and C. J. Joachain, *Introduction to quantum mechanics* (Longman, 1989).

[141] I. S. Gradshteyn and I. M. Ryzhik, *Table of Integrals, Series and Products*, fourth ed. (Academic Press, Inc., Orlando, Florida, 1980).

[142] M. Abramowitz and I. A. Stegun, *Handbook of Mathematical Functions* (Dover, New York, 1964).

[143] B. H. Bransden, C. J. Noble, and R. J. Whitehead, "Positron Scattering by Singly Charged Helium Ions in the Ground State," J. Phys. B (2001), provisionally scheduled for June 2001.

[144] O. A. Fojón, R. Gayet, J. Hanssen, and R. D. Rivarola, Phys. Scr. **51**, 204 (1995).

[145] O. A. Fojón, R. D. Rivarola, R. Gayet, J. Hanssen, and P. A. Hervieux, "Continuum-distorted-wave-final-state approximation in positron-hydrogen atom (ion) collisions with positronium formation," Phys. Rev. A **54**, 4923–30 (1996).

[146] O. A. Fojón, R. D. Rivarola, R. Gayet, J. Hanssen, and P. A. Hervieux, "High-energy positronium formation in positron-hydrogenic ion collisions: scaling laws," J. Phys. B **30**, 2199–208 (1997).

[147] M. A. Abdel-Raouf, "Elastic and Inelastic Scattering of Positrons from Hydrogenlike Ions," Nuovo Cimento **11D**, 791 (1989).

[148] Y. K. Ho, "Resonances in e^+-He^+ scattering," Phys. Rev. A **53**, 3165–8 (1996).

[149] A. K. Bhatia and R. J. Drachman, "Search for resonances in positron-atom systems," Phys. Rev. A **42**, 5117–20 (1990).

[150] J. Callaway, K. Unnikrishnan, and D. H. Oza, "Optical-potential study of electron-hydrogen scattering at intermediate energies," Phys. Rev. A **36**, 2576–84 (1987).

[151] J. Tennyson and C. J. Noble, Comp. Phys. Comm. **33**, 421 (1984).

[152] C. J. Noble, in preparation.

[153] G. T. Condo, "On the absorption of negative pions by liquid helium," Phys. Lett. **9**, 65–6 (1964).

[154] R. S. Hayano, "Precision Spectroscopy of Antiprotonic Atoms," Nuc. Instr. B **171**, 145–52 (2000).

[155] G. Gabrielse, "Comparing the antiproton and proton, and opening the way to cold antihydrogen," Adv. At. Mol. Phys. **45**, 1–39 (2001).

[156] M. Iwasaki *et al.*, "Discovery of antiproton trapping by long-lived metastable states in liquid helium," Phys. Rev. Lett. **67**, 1246–9 (1991).

[157] T. Yamazaki *et al.*, "Formation of long-lived gas-phase antiprotonic helium atoms and quenching by H_2," Nature **361**, 238–40 (1993).

[158] T. Yamazaki *et al.*, "High-precision structural studies of the antiprotonic helium atom $\bar{p}He^+$ by observing laser resonances with $\Delta\nu = \Delta(n-l-1) = 2$," Phys. Rev. A **55**, R3295 (1997).

[159] H. A. Torii *et al.*, "Laser measurements of the density shifts of resonance lines in antiprotonic helium atoms and stringent constraint on the antiproton charge and mass," Phys. Rev. A **59**, 223–9 (1999).

[160] V. I. Korobov and D. D. Bakalov, "Energies and relativistic corrections for the metastable states of antiprotonic helium atoms," Phys. Rev. Lett. **79**, 3379–82 (1997).

[161] V. I. Korobov and I. Shimamura, "Auger transition rates for metastable states of antiprotonic helium $He^+\bar{p}$," Phys. Rev. A **56**, 4587–94 (1997).

[162] H. Knudsen and J. F. Reading, "Ionization of atoms by particle and antiparticle impact," Phys. Rep. **212**, 107–222 (1992).

[163] J. S. Cohen, "Antiproton Capture by Simple Atoms and Molecules," In *The Physics of Electronic and Atomic Collisions*, Y. Itikawa *et al* , ed., p. 540 (AIP, Melville, New York, 2000).

[164] J. S. Cohen, "Formation of protonium in collisions of antiprotons with H and H^-," Phys. Rev. A **36**, 2024–30 (1987).

[165] R. Abrines and I. C. Percival, "Classical theory of charge transfer and Ionization of hydrogen atoms by protons," Proc. Phys. Soc. **88**, 861–72 (1966).

[166] R. Abrines and I. C. Percival, "A generalized correspondence principle and proton-hydrogen collisions," Proc. Phys. Soc. **88**, 873–83 (1966).

[167] R. E. Olson, "n, l distributions in $A^{q+} + H$ electron-capture collisions," Phys. Rev. A **24**, 1726–33 (1981).

[168] B. H. Bransden and M. R. C. McDowell, *Charge Exchange and the Theory of Ion-Atom Collisions* (Clarendon Press, Oxford, 1992).

[169] J. S. Cohen, "Fermion molecular dynamics in the capture of muons by hydrogen atoms," J. Phys. B **31**, L833–40 (1998).

[170] N. H. Kwong, J. D. Garcia, and J. S. Cohen, "Classical-quantal coupling in the capture of muons by hydrogen atoms," J. Phys. B **22**, L633 (1989).

[171] C. L. Kirschbaum and L. Wilets, "Classical many-body model for atomic collisions incorporating the Heisenberg and Pauli principles," Phys. Rev. A **21**, 834–41 (1980).

[172] J. S. Cohen, "Molecular effects on antiproton capture by H_2 and the states of $\bar{p}p$ formed," Phys. Rev. A **56**, 3583–96 (1997).

[173] L. Wilets and J. S. Cohen, "Fermion molecular dynamics in atomic, molecular and optical physics," Contemp. Phys. **39**, 163–75 (1998).

[174] G. Peach, S. L. Willis, and M. R. C. McDowell, "The Classical Theory of Charge Transfer and Ionization Processes in Collisions between Complex Atomic Ions," J. Phys. B **18**, 3921–37 (1985).

[175] S. L. Willis, G. Peach, M. R. C. McDowell, and J. Banerji, "Charge Transfer and Ionization Processes in Collisions Involving Atoms and Ions of Hydrogen and Helium," J. Phys. B **18**, 3939–50 (1985).

[176] J. S. Cohen, "Classical phase-space distributions for atomic hydrogen collisions," J. Phys. B **18**, 1759–69 (1985).

[177] A. S. Wightman, "Moderation of negative mesons in hydrogen I: moderation from high energies to capture by an H_2 molecule," Phys. Rev. **77**, 521–8 (1950).

[178] J. S. Cohen, R. L. Martin, and W. R. Wadt, "Diabatic-state treatment of negative-meson moderation and capture. I. The hydrogen atom," Phys. Rev. A **24**, 33–43 (1981).

[179] J. S. Cohen, R. L. Martin, and W. R. Wadt, "Diabatic-state treatment of negative-meson moderation and capture. II. mixtures of hydrogen and helium," Phys. Rev. A **27**, 1821–30 (1983).

[180] J. D. Garcia, N. H. Kwong, and J. S. Cohen, "Time-dependent quantal treatment of muon-hydrogen collisions," Phys. Rev. A **35**, 4068–73 (1987).

[181] K. Ohtsuki, Y. Ishida, M. Matsuzawa, and M. Shinada, "Low energy collision between antiproton and atomic hydrogen," In *Abstracts of contributed papers for the XXI-ICPEAC conference*, Y. Itikawa, K. Okuno, H. Tanaka, A. Yagashita, and M. Matsuzawa, eds.,**II**, 438 (1999).

[182] J. S. Cohen, "Formation of exotic hydrogen atoms," in *Electromagnetic Cascade and Chemistry of Exotic Atoms*, L. M. Simons, D. Horváth, and G. Torelli, eds., (Plenum Press, New York, 1990), p. 1.

[183] D. H. Perkins, *Introduction to High Energy Physics* (Addison-Wesley Publishing Company, Inc., 1987).

[184] J. S. Cohen, "Slowing down and capture of negative muons by hydrogen: Classical-trajectory Monte Carlo calculation," Phys. Rev. A **27,** 167–79 (1983).

[185] L. D. Landau and E. M. Lifshitz, *Statistical Physics* (Pergamon Press, 1959).

[186] L. P. Pitaevski, "Electron recombination in a monoatomic gas," Zh. Eksper. Teor. Fiz. **42,** 1326–9 (1962), translated into English *Soviet Physics JETP vol. 15(5) pp.919–21.*

[187] R. N. Zare, *Angular Momentum* (Wiley, 1988).

[188] D. M. Brink and G. R. Satchler, *Angular Momentum*, 3rd ed. (Oxford University Press, 1993).

[189] M. E. Rose, *Elementary Theory of Angular Momentum* (Wiley, New York, 1957).

[190] A. R. Edmonds, *Angular Momentum in Quantum Mechanics*, 3rd ed. (Princeton University Press, 1974).

[191] L. D. Landau and E. M. Lifshitz, *Mechanics* (Pergomon Press, Oxford, 1969).

[192] Numerical Algorithms Library (NAg) Mark 17; subroutines D02PDF, D02PVF and D02PWF; 8th order Runge-Kutta.

[193] Numerical Algorithms Library (NAg) Mark 17; subroutines G05CBF, G05CCF, G05CFF and G05DAF.

[194] R. J. Whitehead, J. F. McCann, and I. Shimamura, "Laser-Assisted Formation of Antihydrogen," Phys. Rev. A (2001), provisionally scheduled for 01 July 2001.

[195] A. M. Ermolaev, Hyp. Int. **44,** 375 (1988).

[196] E. Fermi and E. Teller, "The capture of negative mesotrons in matter," Phys. Rev. **72,** 399–408 (1947).

[197] J. S. Cohen and N. T. Padial, "Initial distributions, cascade, and annihilation of $\bar{p}p$ atoms formed in $\bar{p}$+H and $\bar{p}$+H$^-$ collisions in near vacuum," Phys. Rev. A **41**, 3460–8 (1990).

[198] B. H. Bransden, C. J. Joachain, and J. F. McCann, "Positronium formation in positron-atom collisions at intermediate energies," J. Phys. B **25**, 4965 (1992).

[199] S.-M. Li, Z.-J. Chen, Z.-F. Zhou, and Q.-Q. Wang, "Laser-enhanced antihydrogen formation," Phys. Rev. A **59**, 1697–8 (1999).

[200] S.-M. Li, Z.-J. Chen, Z.-F. Zhou, and Q.-Q. Wang, "Reply to [201]," Phys. Rev. A **61**, 067402 (2000).

[201] L. B. Madsen and P. Lambropoulos, "Comment on [199]," Phys. Rev. A **61**, 067401 (2000).

[202] G. Bandrage, A. Maquet, and J. Cooper, "Harmonic generation by a classical hydrogen atom in the presence of an intense radiation field," Phys. Rev. A **41**, 1744 (1990).

[203] R. M. Potvliege, "STRFLO: a program for time-independent calculations of multiphoton processes in one-electron atomic systems I. Quasienergy spectra and angular distributions," Comp. Phys. Comm. **114**, 42 (1998).

[204] *MPI-2: Extensions to the Message-Passing Interface*, Message Passing Interface Forum, 1997, available from `http://www.mpi-forum.org/`.

[205] E. O. Steinborn and K. Ruedenberg, "Rotation and translation of regular and irregular solid spherical harmonics," Adv. Quant. Chem. **7**, 1–81 (1973).

[206] G. Racah, "Theory of complex spectra," Phys. Rev. **62**, 438 (1942), see, for example, [187, 188, 190].

Index